



Universität Hamburg

DER FORSCHUNG | DER LEHRE | DER BILDUNG

Novel stealth carrier strategies for the structural investigation
of ABC transporters by small-angle neutron scattering

Dissertation

zur Erlangung des Doktorgrades der Naturwissenschaften (Dr. rer. nat.)
an der Fakultät für Mathematik, Informatik und Naturwissenschaften
der Universität Hamburg, Fachbereich Chemie

vorgelegt von

Dominique-Maurice Kehlenbeck

Hamburg, 11.01.2023

Die vorliegende Arbeit wurde im Zeitraum von Juli 2019 bis Oktober 2022 in der Arbeitsgruppe von Prof. Dr. H. Tidow am Institut für Biochemie und Molekularbiologie des Fachbereichs Chemie der Universität Hamburg und in der Life Sciences Group von Prof. Dr. V. T. Forsyth am Institut Laue-Langevin (ILL, Grenoble, Frankreich) durchgeführt.

1. Gutachter: Prof. Dr. Henning Tidow
2. Gutachter: Prof. Dr. Christian Betzel

Datum der Disputation: 17.02.2023

Acknowledgements

First, I would like to thank my supervisors Prof. Dr. Henning Tidow from the University of Hamburg and Prof. Dr. Trevor Forsyth and Dr. Sylvain Prévost from the Institute Laue-Langevin (ILL), who allowed me to work on this project in their groups and always provided me guidance, feedback and support whenever it was necessary.

My sincere thank also goes to Prof. Dr. Christian Betzel, preparing the second opinion, and to the examiners of my disputation, Prof. Dr. Andrew Torda and Dr. Thomas Hackl.

This work would not have been possible without the collaboration and support of great people from the Deuteration Laboratory (D-Lab), Lipid deuteration Laboratory at the ILL and the SPC facility of the EMBL in Hamburg.

I would like to thank especially Martine Moulin and Krishna Chaithanya Batchu for showing me how to grow and handle deuterated materials and Juliette Devos for helping me, especially outside the lab. Also, I would like to thank Julius Nitsche, who taught me everything in the lab. Also, I want to thank Kesha for many fruitful discussions, which provided me often another view on my project. I thank Timm O. Koller for always being helpful to me dealing with new software to prepare beautiful figures.

In addition, I would like to thank the staff of the beamlines D11, D22 at the ILL (Grenoble, France), CM01, BM29 at the European Synchrotron Radiation Facility (ESRF, Grenoble, France), P12 on the storage ring PETRA III (DESY, Hamburg, Germany) and SANS-1 at the Paul Scherrer Institute (PSI, Villigen, Switzerland).

I am very grateful to all the members and former members of the Tidow group at the University of Hamburg for their motivation, advice and excellent time in and outside the lab. Therefore, I would like to thank Kesha, Ellen, Anne, Simon, Katha, Katharina, Julius, Yasser and Steffi.

Also, I want to thank the Life Sciences Group at the ILL for the support, inspiring discussions and unforgettable lunch breaks. Thank you, Martine, Juliette, Val, Daouda, Michael, Lukas, Alice, Loic, Giacomo, Florent, Jacques, Mizar and Joao.

Mein besonderer Dank gilt meiner Familie, insbesondere meiner Mama und Christian. Ihr habt mich immer unterstützt und motiviert, sowohl während des Studiums als auch darüber hinaus. Ebenfalls danke ich meiner Schwester Fabi für das rege Interesse an dieser Arbeit. Jessi möchte ich danken, dass sie immer ein offenes Ohr für mich hat und für die Energie, die sie mir jeden Tag schenkt. Ohne euren Rückhalt wäre das hier unmöglich gewesen. Vielen Dank!

Table of Contents

Abstract.....	I
Zusammenfassung.....	III
Publication associated with this thesis.....	V
List of Figures.....	VI
List of Tables.....	X
List of Abbreviations.....	XI
1 Introduction.....	1
1.1 Membrane proteins.....	1
1.1.1 Integral membrane proteins (IMPs).....	1
1.1.1.1 ATP binding cassette (ABC-)transporter.....	2
1.2 Lipid carrier systems.....	4
1.2.1 Membrane scaffold protein based nanodiscs (MSP nanodiscs).....	4
1.2.2 Saposin-lipoprotein nanoparticles (Salipro).....	5
1.3 Structural analysis of membrane proteins.....	6
1.3.1 Basic concept of small-angle scattering.....	7
1.3.1.1 Small-angle neutron scattering (SANS) contrast variation.....	9
1.3.2 Cryogenic Electron microscopy (cryo-EM).....	12
1.3.2.1 Single-particle analysis.....	13
1.4 Aims of the thesis.....	16
2 Material and Methods.....	17
2.1 Chemical reagents.....	17
2.2 Bacteria and cell lines.....	17
2.3 Solutions and culture media.....	17
2.4 Expression und purification of MsbA.....	18
2.5 Expression and purification of Saposin A.....	19
2.6 Expression of matched-out deuterated Saposin A.....	19

2.7	Growing, extraction, and purification of matched-out deuterated phosphatidylcholine (dPC)	20
2.8	Reconstitution of MsbA into membrane scaffold based nanodiscs and Salipro nanoparticles	21
2.9	Small-angle neutron scattering (SANS).....	21
2.10	Small-angle X-ray scattering (SAXS)	22
2.11	Stopped-flow time-resolved small-angle X-ray scattering	23
2.12	Cryogenic-Electron microscopy (cryo-EM)	23
2.12.1	Cryo-EM grid preparation.....	23
2.12.2	Cryo-EM data acquisition	24
2.12.3	Image processing	24
2.12.4	Model building and refinement.....	24
2.13	Differential scanning fluorimetry (nDSF) using Prometheus.....	24
2.14	Baginski ATPase activity assay	25
2.15	Phosphate assay for determining lipid concentrations.....	25
3	Results and Discussion	27
3.1	Chapter 1 – Cryo-EM structure of MsbA in Salipro nanoparticles	27
3.1.1	Cryo-EM structure of ADP-vanadate trapped MsbA in Salipro provides insights into nucleotide coordination	27
3.1.2	Cryo-EM analysis confirms increased flexibility of apo MsbA in Salipro	38
3.2	Chapter 2 – Structural analysis of MsbA by small-angle neutron scattering (SANS) using stealth Salipro nanoparticles.....	44
3.2.1	Expression of matched-out deuterated Saposin A in deuterated minimal media	44
3.2.1.1	Expression and purification of SapA in SHuffle cells.....	44
3.2.1.2	Small scale expression and purification of matched out deuterated Saposin A (dSapA) in deuterated conditions.....	45
3.2.1.3	Expression and purification of dSapA in a high cell density culture (HCDC).....	46

3.2.2	Contrast variation experiments of MsbA in Salipro nanoparticles.....	48
3.2.2.1	Contrast variation experiment of MsbA:hSapA:POPC	50
3.2.2.2	Contrast variation experiment of MsbA:dSapA:POPC	55
3.2.3	SANS experiment of ADP-Vi trapped MsbA in a matched out deuterated Salipro	60
3.2.4	SANS experiment of MsbA:dSapA:dPC leads to larger particles.....	67
3.3	Chapter 3 – Time-resolved small-angle X-ray scattering (SAXS) analysis of MsbA in different lipid carrier systems	72
3.3.1	Stopped-flow time-resolved SAXS analysis of wt MsbA in Salipro.....	72
3.3.2	Time-resolved batch mode SAXS analysis of MsbA-EQ in lipid carrier systems with triggering via mixing	79
3.3.2.1	Time-resolved SAXS analysis of MsbA-EQ in MSP nanodiscs.....	81
3.3.2.2	Time-resolved SAXS analysis of MsbA-EQ in Salipro	86
4	References.....	92
5	Safety and Disposal.....	106
5.1	GHS hazards statements	109
5.2	GHS precautional statements	111
5.3	Disposal.....	112
6	Eidesstattliche Versicherung.....	113

Abstract

MsbA is an essential, prokaryotic ATP binding cassette (ABC-)transporter which transports lipopolysaccharides, lipid A, and glycolipids from the inner to the outer leaflet of the bacterial inner membrane. Also, MsbA can function as a multidrug-resistance transporter and could be target for new antibiotic developments and thus shows high biomedical relevance. However, the exact sequence of events during the transport mechanism is still not fully understood.

In this dissertation, MsbA was incorporated into Saposin lipoprotein nanoparticles (Salipro) and was analysed in a single-particle cryo-electron microscopy (cryo-EM) experiment. ADP-vanadate (ADP-Vi) was used to trap MsbA in the post-hydrolysis state. In this occluded state, we improved the resolution to 3.5 Å, allowing us to model all side chains and visualise detailed interactions of ADP-Vi and Mg²⁺ in the nucleotide-binding site. Furthermore, the analysis of the apo state of MsbA in Salipro indicates great flexibility of MsbA inside the lipid carrier with different opening angles.

Analysing small-angle X-ray scattering (SAXS) data of integral membrane proteins is often challenging due to the scattering contribution of the stabilising system of the membrane protein (detergents, membrane scaffold protein (MSP)-based nanodiscs, Salipro etc.). With the help of fractional deuterium labelled Salipro, the Salipro becomes neutron invisible by maximising the neutron scattering contribution of MsbA to simplify the small-angle neutron scattering (SANS) analysis. In the first step, a large-scale expression protocol of match-out deuterated Saposin A (dSapA) was developed using the high cell density culture (HCDC) in a fermenter to exchange hydrogen to deuterium of 70% of the non-exchangeable hydrogen atoms. Then, in a series of contrast variation small-angle neutron scattering (SANS) experiments, different components of the complex of MsbA in hydrogenated and partially deuterated Salipro were matched out, demonstrating the suitability of matching out components in the Salipro system. Next, the entire Salipro was matched out to measure SANS of MsbA in a stealth Salipro (dSapA with fractional deuterium labelled POPC) in 100% D₂O. This stealth Salipro allows direct observation of the solubilised membrane protein without contribution from the surrounding lipid carrier. The match-out was confirmed via a comparison of the experimental SANS data to the calculated scattering of the previously described cryo-EM structure.

In a time-resolved SAXS experiment initiated by stopped-flow mixing, the catalytic cycle of MsbA incorporated into Salipro was investigated. The sample was mixed with ATP-Mg²⁺ and analysed by SAXS over the first 1000 ms. Our data allowed us to structurally characterise

major states of MsbA involved in the catalytic reaction with ATP. In addition, MsbA containing a catalytically inactive point mutation (MsbA-EQ) incorporated into Salipro and MSP-based nanodiscs were characterised in a time-resolved batch mode SAXS experiment. The ATP binding is not affected in both lipid carrier systems, while the speed of hydrolysis and the ADP/phosphate release are significantly reduced. Interestingly the radius of gyration (R_g) increases significantly above the starting R_g , which could be explained by a possible wider inward open state of MsbA compared to the apo conformation in Salipro/MSP-based nanodiscs.

Zusammenfassung

MsbA ist ein essenzieller, prokaryotischer ATP-Bindungskassetten (ABC)-Transporter, der Lipopolysaccharide, Lipid A und Glykolipide von der inneren zur äußeren Seite der inneren Doppellipidschicht transportiert. Außerdem kann MsbA als Multidrug-Resistenz-Transporter fungieren, was MsbA zu einem Ziel für die Entwicklung neuer Antibiotika machen könnte und die hohe biomedizinische Bedeutung von MsbA zeigt. Dennoch ist der genaue Transportmechanismus von MsbA bisher nicht vollständig aufgeklärt.

In dieser Dissertation wurde MsbA in Saposin-Lipoprotein-Nanopartikel (Salipro) eingebaut und mittels Kryoelektronenmikroskopie (Kryo-EM) analysiert. ADP-Vanadat (ADP-Vi) wurde verwendet, um MsbA in der Konformation nach der Hydrolyse zu fixieren. Für diese geschlossene Konformation konnten wir die Auflösung auf 3.5 Å verbessern, was es uns ermöglichte, alle Seitenketten zu modellieren und detaillierte Wechselwirkungen von ADP-Vi und Mg^{2+} in der Nukleotid-Bindungsstelle zu visualisieren. Die Analyse der Apo-Struktur von MsbA in Salipro zeigt eine große Flexibilität von MsbA innerhalb der Salipro mit unterschiedlichen Öffnungswinkeln des Membranproteins.

Die Auswertung von Daten aus Röntgenkleinwinkelstreuung (SAXS) von integralen Membranproteinen ist aufgrund des Streuungsbeitrags der stabilisierenden Systeme des Membranproteins (wie zum Beispiel Detergenzien, MSP-Nanodiscs, Salipro usw.) oft kompliziert. Mittels Deuterierungen der Salipro kann die Neutronenstreuung auf den Beitrag von MsbA minimiert werden, um die Analyse der Kleinwinkel-Neutronenstreuung (SANS) zu vereinfachen. In einem ersten Schritt wurde ein Expressionsprotokoll für match-out deuteriertes Saposin A (dSapA) entwickelt, bei dem die Kultur in einem Fermenter exprimiert wurde, um einen Austausch von Wasserstoff durch Deuterium von 70 % der nicht austauschbaren Wasserstoffatome zu erreichen. In einer Reihe von Kontrastvariationsexperimenten mit Kleinwinkel-Neutronenstreuung (SANS) wurden verschiedene Komponenten von MsbA in einem hydrierten und in einem teilweise deuterierten Salipro für Neutronen unsichtbar gemacht. Als nächstes wurde die gesamte Salipro modifiziert, um SANS von MsbA in einer Stealth-Salipro (dSapA und teilweise deuteriertes POPC) in 100 % D_2O zu messen. Diese Stealth-Salipro ermöglicht die direkte Beobachtung des Membranproteins ohne den Streuungsbeitrag der umgebenden Salipro. Bestätigt wurde die unsichtbare Salipro durch einen Vergleich der experimentellen SANS-Daten mit der berechneten Streuung der zuvor beschriebenen Kryo-EM-Struktur von MsbA.

In einem zeitaufgelösten SAXS-Experiment wurde der katalytische Zyklus von MsbA in Salipro untersucht. Die Probe wurde mit ATP-Mg²⁺ gemischt und SAXS-Streuprofile über die ersten 1000 ms verfolgt. Anhand dieser Daten konnten wir die wichtigsten Zustände von MsbA, die an der katalytischen Reaktion mit ATP beteiligt waren, strukturell charakterisieren. Darüber hinaus wurde MsbA mit einer katalytisch inaktiven Punktmutation (MsbA-EQ) versehen, in Salipro und MSP-Nanodiscs eingebaut und in einem zeitaufgelösten SAXS Experiment im batch-Modus analysiert. Die ATP-Bindung ist in beiden Systemen nicht beeinträchtigt, während die Geschwindigkeit der Hydrolyse und der ADP/Phosphat-Freisetzung deutlich reduziert ist. Interessanterweise steigt der Streumassenradius (R_g) deutlich über den Ausgangs- R_g an, was möglicherweise durch einen weiter nach innen geöffneten Zustand (wider inward-open state) von MsbA im Vergleich zur Apo-Struktur erklärt werden könnte.

Publication associated with this thesis

Kehlenbeck, D.-M., Traore, D.A., Josts, I., Sander, S., Moulin, M., Haertlein, M., Prevost, S., Forsyth, V.T. and Tidow, H. (2022), Cryo-EM structure of MsbA in saposin-lipid nanoparticles (Salipro) provides insights into nucleotide coordination. FEBS J. <https://doi.org/10.1111/febs.16327>

Josts, I., Kehlenbeck, D.-M., Nitsche, J. and Tidow, H. (2022), Chapter Fourteen - Studying integral membrane protein by SANS using stealth reconstitution systems, Editor: John A. Tainer, Methods in Enzymology. <https://doi.org/10.1016/bs.mie.2022.08.034>.

List of Figures

Figure 1: Architecture of an ABC-transporter embedded in a membrane	2
Figure 2: Structure of MsbA (grey) during the transport cycle	3
Figure 3: Known MsbA structures in nanodiscs shown without nucleotides	4
Figure 4: Schematic representation of the assembly of IMPs into Salipro or MSP nanodiscs.	6
Figure 5: Schematic representation of a small-angle scattering experimental setup	8
Figure 6: The scattering length densities of the major biomolecules used in this work	11
Figure 7: Schematic representation of a SANS experiment of a membrane protein incorporated into a stealth carrier	12
Figure 8: Image formation in a TEM	13
Figure 9: General workflow for single-particle analysis	14
Figure 10: Hydrolysis of adenosine triphosphate to adenosine diphosphate and an inorganic phosphate	25
Figure 11: Characterisation of Salipro-embedded MsbA	28
Figure 12: Characterisation of MsbA incorporated into Salipro	29
Figure 13: Cryo-EM characterisation of MsbA in Salipro	31
Figure 14: Image processing workflow	32
Figure 15: Single-particle cryo-EM analysis of MsbA in Salipro	33
Figure 16: ADP and vanadate coordination to the NBD of MsbA	34
Figure 17: Coordination of ADP, vanadate and Mg^{2+} in the catalytic site of MsbA	35
Figure 18: Detailed view of a lipid bound to the TMD of MsbA	36
Figure 19: Comparison of ADP-Vi trapped MsbA incorporated into Salipro with existing MsbA structures	37
Figure 20: Selected 2D averages of apo MsbA incorporated into Salipro	38
Figure 21: 3D analysis of the flexibility of MsbA in Salipro	39
Figure 22: Refined 3D reconstitution of class 0 – class 4	41
Figure 23: Image processing workflow of apo MsbA in Salipro	42
Figure 24: Comparison of the Salipro disc with MsbA in the apo and the ADP-Vi trapped state in cryo-EM density maps low-pass filtered to 6 Å	43
Figure 25: Purification of SapA from SHuffle cells grown in LB media	45
Figure 26: Purifying dSapA from SHuffle cells grown in a flask in D-Enfors minimal media	46
Figure 27: Expression of dSapA in deuterated HCDC	47

Figure 28: Purification of dSapA from SHuffle cells grown in the fermenter in D-Enfors minimal media	48
Figure 29: SDS-PAGE gel of the MsbA purification.	49
Figure 30: Reconstitution of MsbA into Salipro containing deuterated SapA with hydrogenated POPC and Salipro containing hydrogenated SapA and POPC	50
Figure 31: The scattering length densities of the major biomolecules used in this work and Model of MsbA incorporated into Salipro created with MPBuilder ¹⁵⁹	51
Figure 32: Model of MsbA in a full hydrogenated Salipro with different components matched out due to different H ₂ O/D ₂ O ratios.....	52
Figure 33: Small-angle neutron scattering of MsbA incorporated into hydrogenated Salipro in different backgrounds with varying H ₂ O/D ₂ O ratios.....	53
Figure 34: Analysis of SANS data of MsbA in hydrogenated Salipro in different backgrounds with varying H ₂ O/D ₂ O ratios	54
Figure 35: Comparison of the predicted scattering curve using PEPSI ¹³⁴ from the model created in MPBuilder ¹⁵⁹ to the experimental data.....	55
Figure 36: Model of MsbA in a Salipro of dSapA and POPC with different components matched out due to different H ₂ O/D ₂ O ratios	56
Figure 37: Small-angle neutron scattering of MsbA incorporated into Salipro with match-out deuterated SapA and hydrogenated POPC in different backgrounds with varying H ₂ O/D ₂ O ratios.....	57
Figure 38: Analysis of SANS data of MsbA in matched out deuterated dSapA and hydrogenated POPC in different backgrounds with varying H ₂ O/D ₂ O ratios.....	58
Figure 39: Comparison of the predicted scattering curve using PEPSI ¹³⁴ from the model created in MPBuilder ¹⁵⁹ to the experimental data of MsbA in match-out deuterated Saposin A and hydrogenated POPC in different backgrounds with varying H ₂ O/D ₂ O ratios	60
Figure 40: HPTLC analysis of the elution fractions of the SPE	62
Figure 41: Analysis of the HPLC.....	63
Figure 42: Phosphate assay of purified dPC lipids	63
Figure 43: Reconstitution of MsbA into stealth Salipro with a deuterated polar mixture from <i>E. coli</i> and deuterated PC and empty stealth Salipro	64
Figure 44: Small-angle neutron scattering of MsbA in the occluded state incorporated into stealth Salipro.....	65
Figure 45: Analysis of SANS data of occluded MsbA in stealth Salipro	66

Figure 46: Electron density ab initio shape reconstruction by DENSS ¹³⁵ from the experimental SANS data of MsbA incorporated into stealth Salipro containing a deuterated lipid polar mixture from <i>E. coli</i>	67
Figure 47: Reconstitution of MsbA into stealth Salipro with deuterated PC.....	68
Figure 48: Small-angle neutron scattering of MsbA in the open and occluded state incorporated into stealth Salipro	69
Figure 49: Dimeric model of 7bcw.	69
Figure 50: Small-angle neutron scattering of MsbA in the occluded state incorporated into stealth Salipro.....	70
Figure 51: Analysis of SANS data of occluded MsbA in stealth Salipro	70
Figure 52: Electron density ab initio shape reconstruction by DENSS ¹³⁵ from the experimental SANS data of peak 3 superimposed on the MsbA-dimer (7bcw).....	71
Figure 53: Set up for stopped-flow time-resolved SAXS measurements at EMBL’s P12 Beamline, PETRA III.....	73
Figure 54: Stopped-flow time-resolved SAXS data	73
Figure 55: Analysis of starting conformation of MsbA in Salipro in a time-resolved experiment	74
Figure 56: Evolution of R_g of MsbA in Salipro over the first 1000 ms	77
Figure 57: Singular-value decomposition (SVD) analysis of MsbA in Salipro	78
Figure 58: Individual normalised component contribution of the two independent components present in the SVD analysis of MsbA in Salipro measured in a time-resolved stopped-flow SAXS experiment	79
Figure 59: Reconstitution of MsbA-EQ into MSP-based nanodiscs and Salipro.....	80
Figure 60: ATPase activity of wt MsbA and MsbA-EQ mutant incorporated into MSP-based nanodiscs and Salipro measured by the Baginski assay	81
Figure 61: Scattering differences of MsbA-EQ incorporated in MSP-based nanodiscs after mixing with ATP + Mg^{2+}	82
Figure 62: Analysis of time-resolved SAXS data of MsbA-EQ in nanodiscs	83
Figure 63: A: Evolution of R_g^2 of MsbA-EQ in nanodiscs over time.....	84
Figure 64: Singular-value decomposition analysis of MsbA-EQ in nanodiscs	84
Figure 65: Individual normalised component contribution of the three independent components present in the SVD analysis of MsbA-EQ in nanodiscs.....	85
Figure 66: Scattering differences of MsbA-EQ incorporated in Salipro after mixing with ATP- Mg^{2+}	86

Figure 67: Analysis of time-resolved SAXS data of MsbA-EQ in Salipro	87
Figure 68: A: Evolution of R_g^2 of MsbA-EQ in Salipro over the first 380 min.....	88
Figure 69: Singular-value decomposition analysis of MsbA-EQ in Salipro	89
Figure 70: Individual normalised component contribution of the two independent components present in the SVD analysis of MsbA-EQ in Salipro	90

List of Tables

Table 1: Different MSP constructs with corresponding disc size and molecular weight	5
Table 2: Neutron scattering length for most abundant elements in biological material	10
Table 3: Expression systems used in this study	17
Table 4: Composition of media und solutions	17
Table 5: Cryo-EM data collection parameters	29
Table 6: C-alpha distances between S482 and S378 and Y351 and Q485	40
Table 7: Structural SANS parameters of MsbA incorporated into hydrogenated Salipro in different backgrounds with varying H ₂ O/D ₂ O ratios.....	54
Table 8: Structural SANS parameter of MsbA incorporated into match-out deuterated Saposin A and hydrogenated POPC in different backgrounds with varying H ₂ O/D ₂ O ratios.	59
Table 9: Structural SANS parameters of the predicted MsbA model 7bcw and MsbA in stealth Salipro with deuterated polar lipids from <i>E. coli</i> and deuterated PC.....	66
Table 10: Structural SANS parameters of peak 2 and 3 and the predicted MsbA-dimer model from 7bcw	69
Table 11: χ^2 values of the five different classes from the cryo-EM analysis of apo MsbA in Salipro compared to the experimental data after 0 ms.....	74
Table 12: Structural time-resolved SAXS parameter of MsbA-EQ in nanodiscs with POPC 82	
Table 13: Structural time-resolved SAXS parameter of MsbA-EQ in Salipro with POPC....	87
Table 14: Hazardous and toxic chemicals used in this thesis	106

List of Abbreviations

Δp	Contrast
Å	Angstrom
ABC-transporter	ATP-binding cassette transporter
ADP	Adenosine diphosphate
ATP	Adenosine triphosphate
BSA	Bovine serum albumin
C	Celsius
CL	Cardiolipin
CMC	Critical micelle concentration
Cryo-EM	Cryogenic electron microscopy
CTF	Contrast transfer function
cv	Column volume
DDM	n-Dodecyl- <i>b</i> -D-maltopyranoside
D_{\max}	Maximum particle dimension
dPC	match-out deuterated phosphatidylcholine
dSapA	Deuterated Saposin A
DTT	1,4-Dithiothreitol
<i>E. coli</i>	<i>Escherichia coli</i>
eV	Electron volt
g	Gram
GPCR	G-protein-coupled receptor
h	Hour
HCDC	High cell density culture
HEPES	4-(2-hydroxyethyl)-1-piperazineethanesulfonic acid
HPLC	High pressure/performance liquid chromatography
HPTLC	High-performance thin-layer chromatography
hSapA	Hydrogenated Saposin A
I	Intensity
$I(0)$	Scattering intensity at zero angles
IMAC	Immobilized metal affinity chromatography
IMP	Integral membrane proteins
IPTG	Isopropyl β -D-1-thiogalactopyranoside
K_d	Dissociation constant
kDa	Kilodaltons (= 1,000 Daltons = 1,000 g/mol)
K_m	Michaelis constant
L	Liter
LB	Lysogenic Broth
M	Molar
Mg ²⁺	Magnesium ions

min	Minute
mL	Milliliter
mol	Mole
ms	Millisecond
MSP	Membrane scaffold protein
NBD	Nucleotide-binding domain
nDSF	Nano differential scanning fluorimetry
Ni-NTA	Nickel-Nitrilotriacetic acid
nm	Nanometer
NMR	Nuclear magnetic resonance
OD600	Optical density at 600 nm
PC	Phosphatidylcholine
PDB	Protein data bank
PE	Phosphatidylethanolamine
PG	Phosphatidylglycerol
Pi	Inorganic phosphate
POPC	1-palmitoyl-2-oleoyl-glycero-3-phosphocholine
R_g	Radius of gyration
rpm	Rounds per minute
rt	room temperature
s	Second
Salipro	Sapoin-lipoprotein
SANS	Small-angle neutron scattering
SapA	Sapoin A
SAS	Small-angle scattering
SAXS	Small-angle X-ray scattering
SDS	Sodium dodecyl sulfate
SDS-PAGE	Sodium dodecyl sulphate-Polyacrylamide gel electrophoresis
SEC	Size-exclusion chromatography
SPE	Solid phase extraction
SVD	Singular value decomposition
TB	Terrific Broth
TEM	Transmission electron microscope
TEV	Tobacco Etch Virus protease
TLC	Thin-layer chromatography
TMD	Transmembrane domain
Tris	Tris(hydroxymethyl)aminomethane
v/v	Volume per volume
V_i	Vandate
V_{max}	Maximal reaction speed
V_P	Porod volume

w/v
wt

Weight per volume
Wild type

1 Introduction

1.1 Membrane proteins

Lipid membranes are the primary barrier separating the interior of the cell from the outside environment. Proteins peripheral or embedded into the lipid membranes are responsible for many essential processes like transport, signalling and regulation¹. Membrane proteins encode approximately 20-30% of human genes^{2,3} and around half of the FDA-approved drugs target membrane proteins⁴, showing the high biomedical importance of membrane proteins.

1.1.1 Integral membrane proteins (IMPs)

Membrane proteins can be classified as peripheral and integral depending on whether the protein is permanently or transiently located in the lipid membrane. Peripheral membrane proteins cannot integrate permanently in the membrane due to the lack of a well-organised hydrophobic domain. Instead, they usually interact with the membrane via electrostatic interactions, post-translational modifications or a combination of both⁵. IMPs, on the contrary, will permanently stay in the membrane once there are synthesised and properly folded. This is because a region enriched in hydrophobic amino acids is embedded in the lipid bilayer, interacting with the hydrophobic chains of the lipids, while charged and polar amino acids are located outside the membrane exposed to the solvent environment^{1,5}. IMPs can be grouped into three classes: single-pass, multi-pass and β -barrel transmembrane proteins. The first two groups are alpha-helical membrane proteins responsible for most of the functions in the membranes of eukaryotes. In contrast, β -barrels transmembrane proteins are found in the outer membrane of bacteria, chloroplasts and mitochondria¹. In the Protein Data Bank (PDB), less than 1% of the protein structures belong to IMPs, while around 30% of all open reading frames encode IMPs⁶. This vast difference is due to the difficult handling of IMPs in solution. Often it is necessary to extract IMPs from the lipid bilayer to study them. The hydrophobic regions of the IMPs have to be shielded from the polar solvents, for example, with detergents. Detergents are amphipathic molecules consisting of a polar head group and a hydrophobic acyl chain. In contrast to the cylindrical shape of a lipid, the geometry of a detergent molecule is conic. The hydrophobic effect and the shape drive the detergents into spherical micelles above the critical micelle concentration (CMC). In the micelles, the hydrophobic acyl chains form the core of the spheres surrounded by the polar headgroups exposed to the polar solvent. The CMC varies between the detergents, depending on the chemical nature of the headgroup and the length of the acyl chain. The formation of micelles is the basis for membrane protein solubilisation. The hydrophobic parts of the IMPs are covered by the acyl chain of the detergent

while the polar headgroups are exposed to the solvent^{7,8}. However, detergents often negatively influence protein stability and activity due to the poor mimic of the lipid bilayer⁹. Therefore, a better mimic of the natural lipid environment is often necessary to maintain the full function of the protein¹⁰. Several tools have been established for structural studies of IMPs like membrane scaffold protein (MSP) based nanodiscs or Saposin-lipoprotein nanoparticles (Salipro) to overcome these problems. These two systems provide the IMPs with a native-like lipid environment and will be further described in 1.2.

1.1.1.1 ATP binding cassette (ABC-)transporter

The transport of molecules and ions by transmembrane proteins through biological membranes is an essential process in all known organisms. One of the largest family of transmembrane proteins are ATP binding cassette (ABC-)transporters, which use the released free energy from adenosine triphosphate (ATP) hydrolysis to transport substrates through the membrane¹¹. Many of these primary active transporters are built of two monomers consisting of a transmembrane and nucleotide-binding domain each. Together they build a functional dimer (Figure 1), where the transmembrane and the nucleotide-binding domain are connected through a coupling helix. With the dimerization of the two nucleotide-binding domains, a nucleotide-binding pocket is built and one ATP binds to each nucleotide-binding domain. The transporter changes to an occluded state¹². In ABC exporters, the substrate is transported to the extracellular milieu via rearrangements of the core helices and the protein changes to the inward-facing conformation. Hydrolysis of the ATP and the release of inorganic phosphate leads again to the starting conformation of the protein.

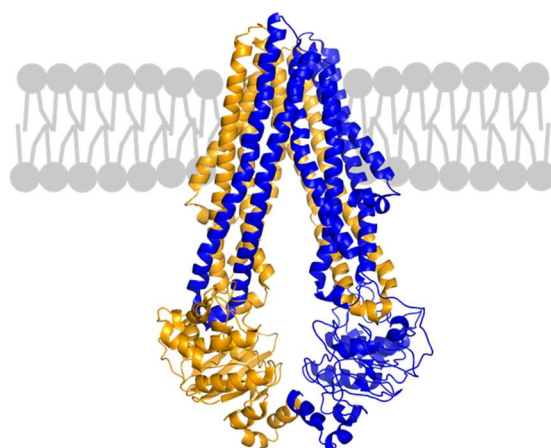


Figure 1: Architecture of an ABC-transporter embedded in a membrane (grey). The two monomers with a transmembrane and a nucleotide-binding domain each are coloured blue and orange.

1.1.1.1.1 MsbA

MsbA is a prokaryotic ABC-transporter located in the inner membrane. It acts as a lipid floppase and transports lipopolysaccharides, lipid A, and glycolipids from the inner to the outer leaflet of the lipid bilayer^{13,14}. In addition, MsbA can function as a multidrug-resistance transporter by exporting several small hydrophobic molecules¹⁵. MsbA is a homodimer composed of two nucleotide-binding (NBDs) and two transmembrane domains (TMDs)^{16,17}. The transport is performed through conformational changes in the TMDs, while ATP binding and hydrolysis occur in the NBDs. The transport potentially follows a power stroke mechanism, where the substrate is binding to the TMDs of the inward open conformation of MsbA. Afterwards, two ATP molecules bind to the NBDs, leading to the dimerization of the NBDs. The following hydrolysis of the ATP molecules induces structural rearrangements of the TMDs, allowing the substrate to enter the periplasmic half of the lipid bilayer. Finally, with the adenosine diphosphate and inorganic phosphate release, MsbA reaches the starting inward open state¹⁷. The exact sequence of events of the transport mechanism is still not fully understood.

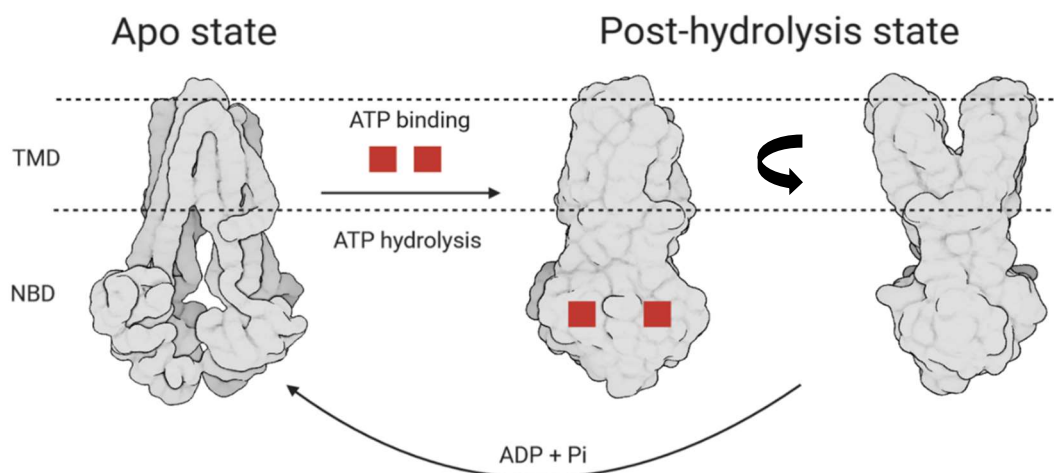


Figure 2: Structure of MsbA (grey) during the transport cycle. MsbA is starting in the inward open (apo) conformation allowing the LPS (not shown) to bind to the TMDs. The binding of two ATPs (red squares) to the NBDs leads to conformational changes of the protein to the occluded, followed by the outward open conformation after the ATP hydrolysis. With the release of ADP and inorganic phosphate, MsbA returns to the inward open state. Created with BioRender.com

Different conformations of MsbA have been determined over the last decade, including crystal structures in detergent and single-particle cryogenic electron microscopy (cryo-EM) in MSP-based nanodiscs^{16,18–20}. These structures range from inward-open via occluded state to outward-open conformation (Figure 3). Nevertheless, a complementary technique like small-angle scattering to confirm the native structures of MsbA in a lipidic environment in non-cryogenic conditions is still lacking.

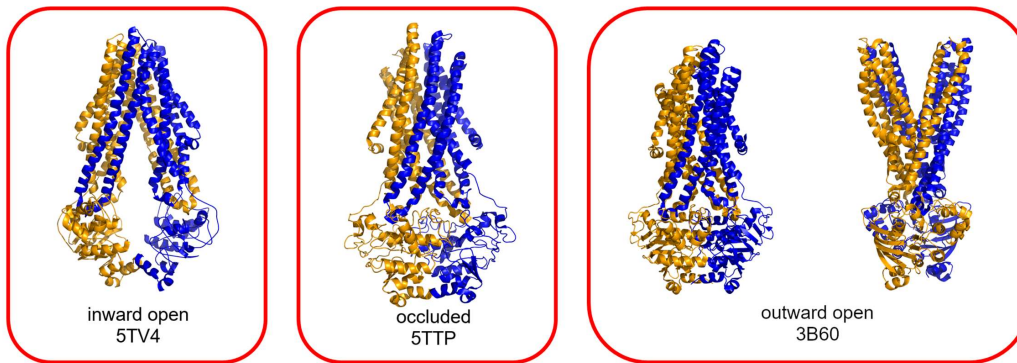


Figure 3: Known MsbA structures in nanodiscs shown without nucleotides. The structure of MsbA shows an inward open state (pdb: 5TV4)¹⁷, while the addition of ADP-vanadate leads to an occluded state of the protein (5TTP)¹⁷. MsbA in detergent in complex with AMPPNP adopts an outward open state (3B60)¹⁶.

1.2 Lipid carrier systems

There are several strategies to mimic the native-like lipid bilayer to analyse IMPs *in vitro*. The two lipid carrier systems used in this project to reconstitute the ABC-transporter MsbA are membrane scaffold protein (MSP) based nanodiscs and Saposin-lipoprotein nanoparticles. In both systems, the membrane protein is incorporated into a bilayer of lipids allowing structural investigations of IMP in a detergent-free environment. Both will be described in more detail in sections 1.2.1 and 1.2.2.

In this project mainly the phospholipid [(2*R*)-3-Hexadecanoyloxy-2-[(*Z*)-octadec-9-enoyl]oxypropyl] 2-(trimethylazaniumyl)ethyl-phosphate (POPC) was used. Even though POPC is not present in the natural membranes of *E. coli*, MsbA shows high activity and thermostability in both systems²¹. Another reason for using POPC was the previously established protocol to grow and purify a match-out deuterated version of POPC with 78% deuteration of the headgroups and 92% deuteration of the acyl chains. For a more natural lipid environment for MsbA, a perdeuterated *E. coli* polar lipid mixture was also used for small-angle neutron scattering (SANS) studies.

1.2.1 Membrane scaffold protein based nanodiscs (MSP nanodiscs)

One well-described method to analyse the structure or activity of IMPs is the incorporation into an MSP nanodisc, a disc-shaped particle of a bilayer of lipids encircled by two molecules of MSPs²². With the addition of MSPs and lipids to IMPs solubilised in detergent, the membrane proteins self-assemble into the MSP nanodiscs after detergent removal, with the TMDs embedded into the lipid bilayer of the discs²³, yielding a soluble complex. Following size-exclusion chromatography, larger aggregates and empty nanodiscs are separated from the

assembled IMP nanodisc complexes. To obtain homogeneous and monodisperse units, the correct molar ratio between membrane protein to MSP to phospholipid is crucial²⁴. This ratio depends on the size of the TMD of the membrane protein, the MSP construct and the size and number of the lipids. Furthermore, different MSP constructs differ in additional helices in the central part of the MSP, leading to an enlargement of the MSP nanodiscs²⁴, so it is possible to selectively assemble monomers or oligomers of the target membrane protein into one MSP nanodiscs. It is also possible to yield shorter versions of MSP by truncating helices to study proteins with a small transmembrane domain.

Table 1: Different MSP constructs with corresponding disc size and molecular weight²⁴.

Protein	Disc size (Stoke-hydrodynamic diameter [nm])	Molecular weight [kDa]
MSP1	9.7	24.6
MSP1D1	9.5	24.7
MSP1E1	10.4	27.5
MSP1E3D1	12.1	32.6

MSPs are α -helical proteins derived from human apolipoprotein A-1²², the main component of high-density lipoprotein particles. Apolipoprotein A-1 is built of a globular domain at the N-terminus and ten amphipathic helices, which are crucial for lipid binding. In this project, the MSP construct MSP1D1 was used, yielding empty nanodiscs of 9.5 nm diameter (see Table 1) containing 90-120 phospholipids depending on the type and size of the lipids^{25,26}.

1.2.2 Saposin-lipoprotein nanoparticles (Salipro)

Recently, a new lipid carrier system called Salipro has been developed as an alternative system to reconstitute membrane proteins. Similar to MSP nanodiscs, a disc-shaped bilayer of lipids is formed and encircled by several Saposin A (SapA) proteins. Saposin proteins are modulators of lipid membranes with lipid binding properties^{27,28}. Due to the smaller size of SapA (8 kDa) compared to MSP1D1 (24.7 kDa), several SapA proteins are necessary to encircle the lipid bilayer and build a disc-shaped particle²⁸⁻³⁰. This enables the formation of different sizes of Salipro without changing the construct of the carrier protein. Therefore, Salipro can adapt to varying dimensions of TMDs of the IMP depending on the stoichiometric ratio of IMP to SapA to lipids, yielding monodisperse and homogenous units³⁰. The mechanism of assembly is very comparable to the MSP nanodiscs²⁹.

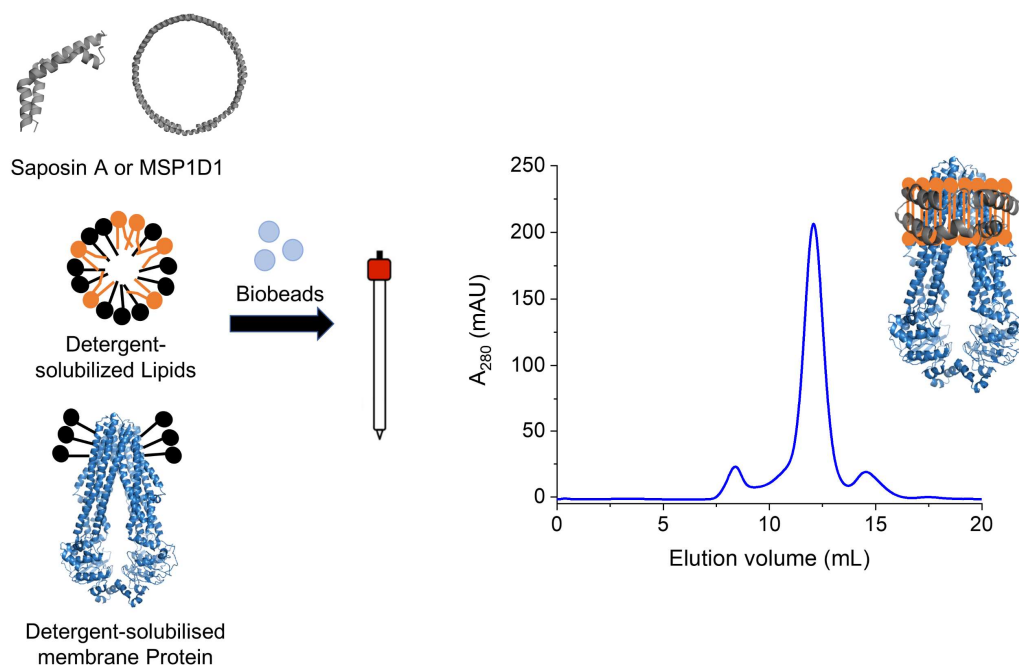


Figure 4: Schematic representation of the assembly of IMPs into Salipro or MSP nanodiscs. The carrier protein SapA or MSP1D1 are mixed with detergent-solubilized lipids and the membrane protein. Next, initiation of the self-assembly process with the detergent removal through Biobeads, yielding monodisperse units. Afterwards, a purification on a size-exclusion column was performed.

1.3 Structural analysis of membrane proteins

Only the three techniques crystallography, nuclear magnetic resonance (NMR) and cryogenic electron microscopy (cryo-EM), can provide atomic resolution structural information of proteins. So far, crystallography is the most successful method to resolve the three-dimensional structure of membrane proteins^{31–36} and has led to numerous breakthroughs in the structural analysis of important membrane protein complexes like G-protein-coupled receptors (GPCRs)^{37,38} and membrane pumps^{39–41}. However, it is very challenging for many membrane proteins to obtain crystals that diffract sufficiently, especially when a lipid environment is required for stability and function^{21,42,43}.

The second technique which can provide high-resolution information on membrane proteins in solution is nuclear magnetic resonance (NMR) spectroscopy. With NMR, it is possible to analyse the membrane protein in a lipid bilayer under native-like conditions; however, the limitation is the maximum size of the samples that can be studied, so often the studies of multi-subunit complexes are very complex in NMR studies^{44–46}.

Cryogenic electron microscopy (cryo-EM) is another powerful technique in structural biology and will be discussed in detail in section 1.3.2.

Low-resolution techniques for structural studies of membrane proteins are the small-angle scattering (SAS) methods, small-angle x-ray scattering (SAXS) and small-angle neutron scattering (SANS). Detergents are often used to stabilise membrane proteins in solution⁹. However, analysing SAS data is often challenging for membrane proteins in detergents. Most membrane proteins are purified with a detergent concentration close to or above the critical micelle concentration (CMC), resulting in two different micelle populations. One population are the micelles built of membrane protein and detergent, while the other are pure detergent micelles and individual detergent molecules. The concentration of co-purified empty micelles is usually difficult to estimate, which makes it very problematic to provide an optimal buffer match. Therefore, the resulting scattering data contains the signal of both micelle populations. To overcome this problem, the membrane proteins can be reconstituted into MSP nanodiscs (see section 1.2.1) and Salipro (see section 1.2.2). Another possibility is to separate the empty micelles by performing size-exclusion chromatography coupled with SAXS/SANS.

1.3.1 Basic concept of small-angle scattering

Monitoring conformational changes of biological macromolecules and complexes have become an increasing aspect of modern structural biology. Over the last decade, the small-angle scattering (SAS) techniques have become increasingly powerful methods that allows studies of water-soluble protein systems⁴⁷⁻⁵⁰. The method analyses macromolecule samples directly in solution and can be applied to numerous different sample environments⁵¹⁻⁵³. Furthermore, the required sample volume and concentration have been brought down to about 10-20 μL of a few mg/mL for small-angle X-ray scattering (SAXS) and 200-300 μL at a similar concentration for small-angle neutron scattering (SANS)^{47,54}, which is compatible to what is typically achievable for a lot of membrane protein systems. Therefore, SAS has become an essential technique for studying membrane proteins reconstituted into detergents⁵⁵⁻⁶³ or lipid systems like MSP nanodiscs⁶⁴⁻⁶⁸ and Salipro.

Particles are randomly distributed and oriented in the solution. The rotational averaging of all molecules limits the resolution of SAS techniques. SAS techniques enable the extraction of global structural parameters like the radius of gyration (R_g), the maximal particle dimension (D_{max}) and the distribution of distances between atoms within a particle directly from the experimental data⁶⁹.

During this PhD project, SAS using X-ray photons was used to study the ABC-transporter MsbA incorporated into MSP nanodiscs and Salipro, as well as neutrons for studies of MsbA in stealth Salipro. Even though the interaction of X-rays and neutrons with matter is different,

the interpretation of the scattering data is similar. In an X-ray scattering experiment, the X-ray photons are scattered by the electron, while the neutrons are primarily scattered by the atomic nuclei.

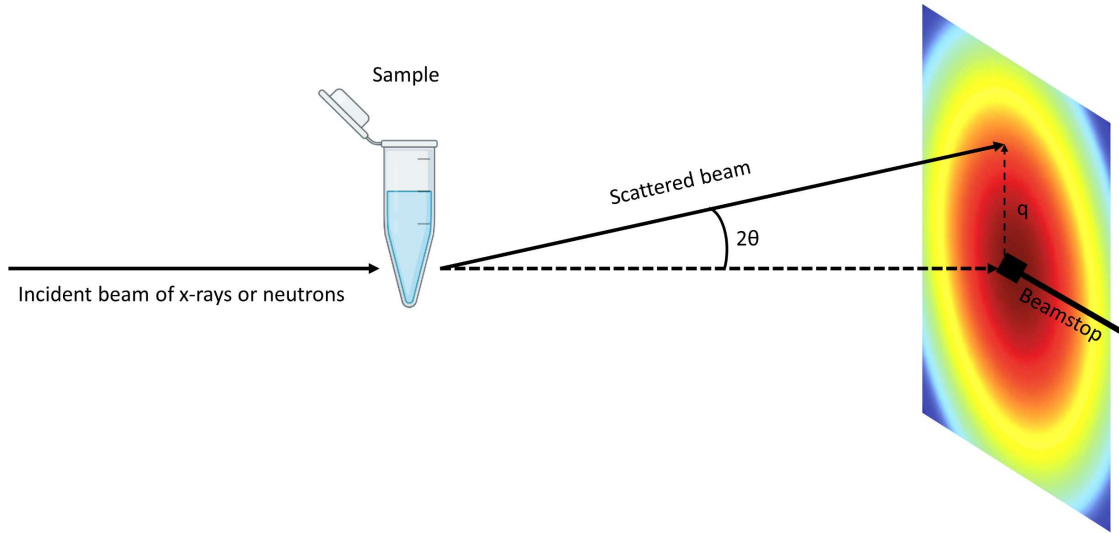


Figure 5: Schematic representation of a small-angle scattering experimental setup. A collimated X-ray or neutron beam illuminates the sample and the scattered radiation is recorded on a 2D detector.

When a sample, like a solution containing protein molecules, is illuminated by a collimated beam, a small portion of the incident beam will be scattered. The scattered particles are detected on a 2D position-sensitive detector. The sample particles are randomly oriented, resulting in a centrosymmetric scattering pattern with intensities to every angle. The intensities can be radially averaged, yielding a plot of the scattering intensity against the scattering angle 2θ . The wavelength-dependent scattering angle 2θ can be converted into the wavelength-independent scattering vector q ,

$$q = \frac{4\pi \sin \theta}{\lambda} \quad (1)$$

where 2θ is the angle between the scattered and the incident beam and λ is the wavelength of the incident radiation^{70,71}. Assuming no distance correlation between particles in solution, their contribution to the plot can be described in

$$I(q) = n \left\langle \left| \int_V (\rho(\vec{r}) - \rho_S) e^{-i\vec{q}\cdot\vec{r}} d^3\vec{r} \right|^2 \right\rangle \quad (2)$$

where $I(q)$ is the scattered intensity, n the number of particles per unit volume, $\rho(\vec{r})$ is the scattering length density (SLD) of the particle at the position r and ρ_S the SLD of the solvent. The integral is taken over the particle volume V , averaged over time, orientations, and combinations of all structures in the solution. The difference in the SLD between particles and

solvent is termed the contrast and is called $\Delta\rho$ ^{70,71}. In a SAXS experiment, the contrast depends on the averaged electron density of the particles compared to the solvent. The X-ray scattering length is linked to the number of electrons in the atom and the measured scattering intensity is thus the difference in electron density. The contrast in a SANS experiment will be discussed in section 1.3.1.1.

The scattering intensity provides information related to the global shape of the particles in the solution. A general approach to analyse SAS data is to Fourier transform the scattering intensity function to obtain the distance distribution plot ($P(r)$) of the scattered particles. Because of the direct space representation, the distance distribution plot is more intuitive and allows the analysis of the particle shape straightforwardly⁷². The $P(r)$ function describes the probable frequency of distances in a particle and defines the maximal particle dimension D_{\max} . Additionally $P(r)$ can provide information about the shape and the volume of the protein or complex⁷². This method depends on several assumptions, e.g., the $P(r)$ is zero at $r = 0$ and at the D_{\max} and the proposed $P(r)$ function should be smooth.

Two other parameters related to the size and shape of the measured sample can be determined from the SAS data. The radius of gyration (R_g)⁷¹ and the forward scattered intensity at zero angles ($I(0)$)⁷⁰ provide robust structural information and can be calculated by different mathematical methods. The R_g is the root-mean-squared distance from the centre of mass of the particle so that particles with the same volume but with different shapes also differ in R_g . The $I(0)$ describes the scattering intensity at zero angle $\theta = 0^\circ$ and cannot be experimentally measured due to the radiation of the direct beam and the positioning of the beamstop at $q = 0$. However, it can be determined by extrapolation and is proportional to the number of scattering particles per unit volume (N), the contrast ($\Delta\rho$) and the particle volume (V)⁷².

$$I(0) = N(\Delta\rho V)^2 \quad (3)$$

The values of R_g and $I(0)$ can be obtain by fitting the data with the Guinier approximation.

$$I(q) = I(0)e^{\frac{-q^2 R_g^2}{3}} \quad (4)$$

The R_g is yielded by the slope of the linear plot in the low- q range, plotting $\ln I(q)$ versus q^2 . $I(0)$ is determined by the calculation from the y-intercept⁷³.

1.3.1.1 Small-angle neutron scattering (SANS) contrast variation

X-rays interact with electrons, while neutrons interact with the nuclei of the atom. Therefore, the scattering length from X-rays is dependent on the number of electrons of an atom. In

contrast, the neutron scattering length varies in a non-systematic manner and is isotope dependent⁷⁴.

Table 2: Neutron scattering length for most abundant elements in biological material.

Element	Scattering length ($\Sigma b/10^{-5}$ Å)
Hydrogen	-3.74
Deuterium	6.67
Carbon	6.65
Nitrogen	9.36
Oxygen	5.80
Phosphorus	5.13
Sulfur	2.85

In addition, the magnitude of scattering length of the most common atoms in biological material is comparable among their isotopes due to the phase inversion of the scattered neutrons^{75–77}. However, there is one exception. Between hydrogen and deuterium, the neutron scattering length differs drastically because of the missing phase inversion of hydrogens, resulting in a negative neutron scattering length. This phenomenon provides the basis for SANS contrast variation. The substitution of deuterium for hydrogen often has only a limited impact on the structure and function of the biological material⁷⁰. The contrast ($\Delta\rho$) can be tuned by varying the hydrogen to deuterium ratio in the solvent so the neutron scattering length density is equal between the macromolecule and the solvent ($\Delta\rho = 0$)⁷⁷. With zero net coherent scattering, the macromolecule does not contribute to the scattering signal and is matched out. This D₂O:H₂O ratio is the “contrast match point” of this macromolecule⁷⁰. Due to the different composition of each biological material, such as e.g. proteins, DNA and phospholipids, each has a different contrast match point, which allows to match-out specific components in a multi-component complex. For example, in 42% D₂O, all hydrogenated proteins or at 8% D₂O, all hydrogenated phospholipids are matched out (Figure 6). On the other hand, selective deuteration of biological material can be done to manipulate the neutron scattering density to the same level as the solvent to reach a match-out. This specific level of deuteration is called “match-out deuteration”.

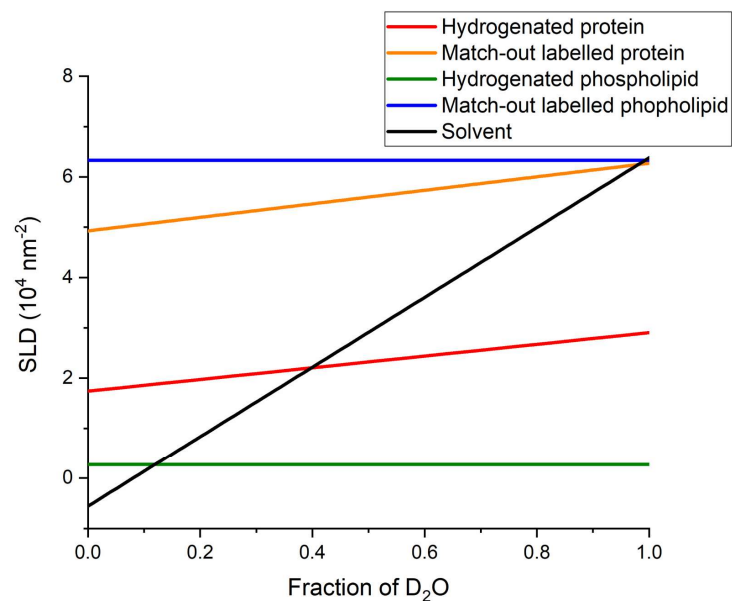


Figure 6: The scattering length densities (SLDs) of the major biomolecules used in this work are plotted as a function of the volume percentage of D₂O, assuming all labile hydrogens are exchanged. The match points of each biomolecule correspond to the intersection with the solvent function. For example, in 100% D₂O match-out labelled proteins and phospholipids have no contrast with the solvent and are not contributing to the scattering signal. Modified from Dunne *et al.*⁷⁸

In this project, the membrane protein complex consists of a bilayer of phospholipids encircled by carrier proteins and the membrane protein. With selective biological or chemical deuteration of the phospholipids and the carrier proteins, it is possible to match-out the entire carrier to simplify the data analysis of the membrane protein in a complex lipid-protein complex^{70,74}.

1.3.1.1.1 Stealth lipid carrier for SANS experiments

The advantage of SANS compared to SAXS is the possibility to make specific components in a multi-component system “neutron invisible” by selective deuteration of the components and solvent adjustments. The required D₂O concentration in the solvent depends on the hydrogen concentration of the components to match. Salipros are a recently developed tool to incorporate and study membrane proteins in a native-like lipid environment. However, the analysis of SAXS data is very challenging due to the extensive contribution of the lipid carrier (several Saposin A proteins and bilayer of phospholipids) to the scattering signal⁷⁹. Since proteins and phospholipids have different contrast match points, making the whole lipid carrier “neutron invisible” in one D₂O concentration is impossible. By selective deuteration of the two components, the neutron scattering length density can be matched, so both components become invisible at the same D₂O concentration in the solvent. With the introduction of selectively deuterated MSP nanodiscs, it is possible to turn the disc invisible to neutrons in 100% D₂O⁸⁰. With the large incoherent scattering cross-section of hydrogen, H₂O will increase the background noise resulting in decreased signal to background scattering signal. Therefore,

biological SANS measurements are often performed in 100% D₂O. In order to reach 100% neutron invisibility, the phospholipids and the MSP were selectively deuterated. The genetic modified *E. coli* strain AL95 was used to deuterate phospholipids to the match point to 100% D₂O, yielding a deuteration level of 78% in the headgroup and 92% in the acyl chains of the phospholipid⁸¹. The deuteration of the MSP was performed in a recombinant expression in *E. coli* using 85% deuterated minimal medium containing hydrogenated glycerol as a carbon source to yield 70% deuteration of the non-exchangeable hydrogen atoms⁸⁰. Using these “stealth MSP nanodiscs” makes it possible to study the structure of membrane proteins without the scattering contribution of the lipid carrier.

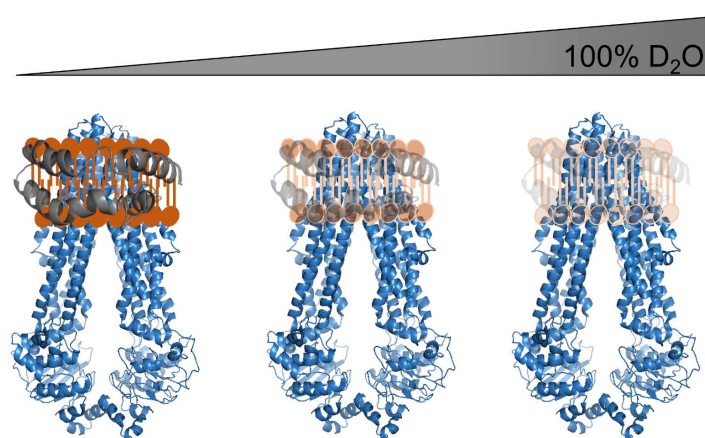


Figure 7: Schematic representation of a SANS experiment of a membrane protein incorporated into a stealth carrier. The lipid carrier becomes neutron invisible by increasing the deuteration level in the solvent until the lipid (brown) and the carrier protein (grey) are not contributing to the neutron scattering (right structure) and only the membrane protein (blue) contributes to the scattering signal.

1.3.2 Cryogenic Electron microscopy (cryo-EM)

Structural information of membrane proteins is key to understand interactions with small-molecule drugs in atomic detail. In addition, it is also important to understand essential cellular mechanisms like transport and signalling on a molecular level. However, small-angle scattering techniques enable only low-resolution information, lacking molecular insights on an atomic scale. On the other hand, X-ray crystallography contributes to most of the atomic coordinates of biological macromolecules in the protein data bank (PDB)⁸². However, the resolution in this method depends on the quality of the protein crystal. Therefore, obtaining a well-ordered crystal of sufficient size is essential for atomic structure determination. Unfortunately, it is difficult or sometimes impossible for many proteins to grow such high-quality crystals, especially for integral membrane proteins or large and dynamic complexes. To overcome these problems, in the 1970s, a new EM-based method called single-particle cryo-EM was developed^{83,84}, where samples are directly visualised under the electron beam. Also, the

visualisation is not limited by the complexity and size of the sample. Additionally, different conformations can be characterised by the development of computational techniques⁸⁵⁻⁸⁷.

The transmission electron microscope (TEM) image is achieved by interactions between the electron beam and the specimen⁸⁸. This interaction results in the scattering of the electrons either elastically or inelastically⁸⁹. If a moving electron hits an atom, it will be scattered elastically (changing direction without losing energy) because of the significant weight difference. Elastically scattered electrons at high angles cannot be focused back due to the objective aperture and are not contributing to the image⁸⁹. On the other hand, the electrons elastically scattered at small angles are focused back and have a different phase at the focal plane compared to reference beam electrons⁸⁸ (Figure 8). Therefore, if a small objective aperture is used, only electrons with a small-angle scattering contribute to the image and enhance the contrast. However, electrons with a high-angle scattering contain high-resolution information. Therefore, it is crucial to balance good contrast and high resolution. On the other hand, if a moving electron collides with electrons of the sample, it is scattered inelastically, affecting the wavelength and direction. The difference in wavelength cannot be corrected due to chromatic aberration of the lenses resulting in noise in the final image⁹⁰.

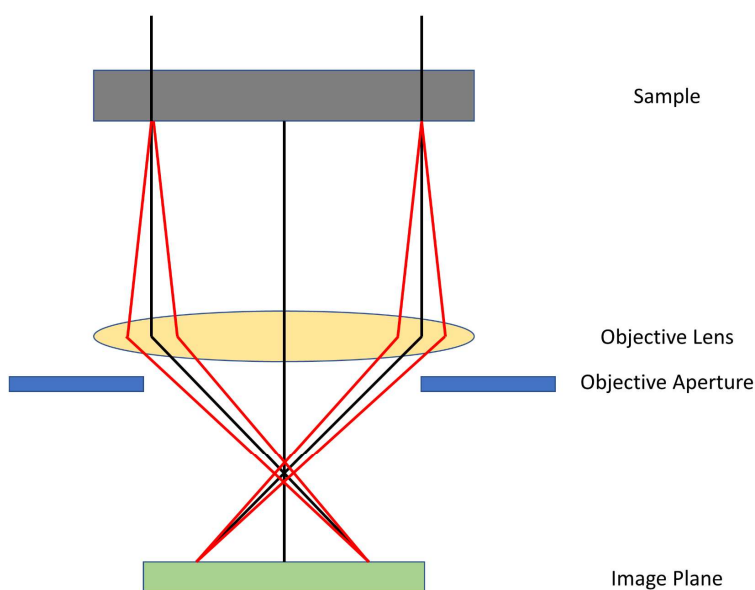


Figure 8: Image formation in a TEM. The Image formation is based on the interference of elastically scattered electrons (shown in red) with the not scattered electron beam (shown in black) at the image plane.

1.3.2.1 Single-particle analysis

Recently the introduction of a new generation of electron detectors⁹¹ and the development of algorithms to correct for beam-induced movement and specimen drift⁹²⁻⁹⁴, new image-processing software⁹⁵⁻⁹⁹ and automated data collection^{100,101} increased the limit of single-

particle cryo-EM to atomic resolution. This “resolution revolution”¹⁰² allows structure determination of ideal proteins up to a resolution of around 1.25 Å¹⁰³. These new developments significantly impact structural biology, allowing solving structures of many protein complexes that could not crystallise, like ion channels^{104,105} and transporters¹⁰⁶.

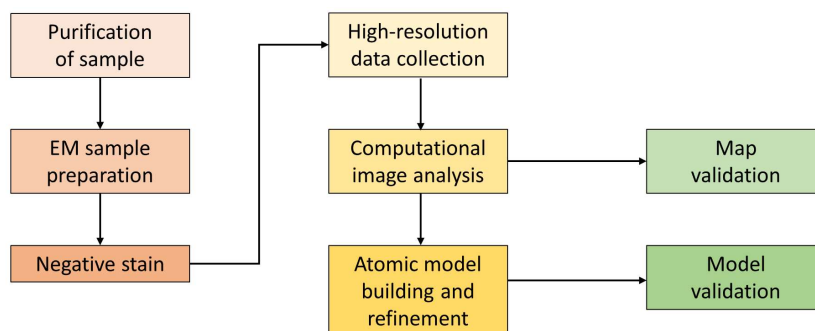


Figure 9: General workflow for single-particle analysis. Starting with the purification of the target and the EM sample preparation with negative stain or vitrification for measurements in cryo-conditions. The next step is the analysis of the negative staining to determine the quality of the sample, followed by the high-resolution data collection in cryo-conditions. The data are computationally processed, yielding an electron density map. Based on this map, an atomic model can be built and refined. The map and model need to undergo several validation steps. The workflow is often not linear, and some steps must be repeated and optimized before proceeding. (Adapted from Lyumkis, 2019¹⁰⁷).

First, the biological sample has to be extracted and purified for a single-particle analysis. The next step is to apply the sample onto grids for screening and data collection. Negative staining with uranyl acetate/formate, ammonium molybdate or methylamine tungstate is used to determine the sample’s quality before the data collection in cryo-conditions^{108,109}. These heavy metal stains dehydrate the sample and generate a contrast at room temperature measurements, yielding low-resolution images. A negative stain develops a strong outline of the particles, whereas internal information is lost. In addition, the dehydration of the sample leads to a flattening of the particles¹¹⁰, and they will add a layer of carbons to the samples, which increases the noise background. All these factors limit the resolution and information of this technique.

After successful results from the negative stain, the next step is the cryo-EM experiment. The sample is applied on a grid and frozen in liquid ethane to maintain a “near-native” state of the sample’s molecular structure because the buffer does not have sufficient time to crystallize^{84,111–113}. Nowadays, these vitrification protocols are robotised and performed in a controlled environment¹¹⁴, allowing the user to reproduce the vitrification conditions.

The data collection for single-particle cryo-EM has become more standardised over the last few years. During data acquisition, the specimen is tilted to minimise the problem of preferred orientations of the sample resulting from the absorbance to the air-water interface during the

vitrification. Using tilts results in a more even coverage of the Fourier space voxels and improves the reconstructed volume¹¹⁵. Most high-resolution cryo-EM structures in the PDB have been collected on a 300-kV microscope. The high accelerating voltage reduces the amount of inelastic scattered electrons and specimen charging^{116,117} and avoids a low-resolution contrast.

Once the data is collected, it is necessary to analyse the images in order to reconstitute one or multiple models from the sample. Today, a large variety of processing software tools are available for image analysis developed in the last decades¹¹⁸. In principle, the main steps in the data processing in a single-particle analysis are motion correction of the movies, yielding micrographs, picking particles, determining the contrast transfer function (CTF) parameters, performing 2D and 3D alignments and classifications, refining angular orientations and building the model.

Once movies are recorded, the position of the particles is corrected due to the beam-induced motion¹¹⁹, yielding micrographs. Next, the CTF estimation of the projected images is performed⁸⁸ due to the amount of defocus and spherical aberration constant of the lenses, which affects the final images. The CTF for a certain micrograph can be determined by calculating the Fourier transformations of images selected from this micrograph that contain a carbon film. By fitting the theoretical expression of CTF to the CTF of the carbon film, the defocus and the CTF parameters can be obtained. The picking of particles can be done manually or automatically. Automatic particle picking is usually based on locating particles by cross-correlating rationally averaged images of references. The user manually selects several particles, which are averaged and used as templates. In the 2D classification, all particles are grouped depending on the represented view and are aligned with each other, resulting in class averages. Based on the obtained class averages, a 3D model can be created by determining the Euler angles, which describes the orientation of the particles in three dimensions. Different projections of the 3D initial model are used to correct the Euler angle, improving the model with each iteration. If the Euler angles are not changing over iterations, the Euler angles are fixed, yielding the final reconstruction¹²⁰.

The validation of the cryo-EM map and atomic model is the final step in a single-particle analysis. Validation of the map ensures the model and representative data are correct and represented in the best possible way to avoid severe mistakes and misinterpretations^{121–123}. The standard metric for cryo-EM maps is the FSC curve¹²⁴, a 3D extension of the 2D Fourier ring correlation curve¹²⁵ and describes the correlation between the two half maps. Each half map

was reconstituted from a randomly selected half subset of the data. Finally, the nominal resolution is determined at the intercept point at a specific threshold, typically 0.143¹²⁶.

In this project, single-particle cryogenic electron microscopy was used to analyse MsbA in different conformations incorporated in Salipro to obtain high-resolution structural information.

1.4 Aims of the thesis

The aim of the thesis is the adaptation of the concept of stealth MSP-based nanodiscs to stealth Saposin-lipoprotein nanoparticles. This enables the structural analysis of integral membrane proteins like MsbA in a native-like lipid environment without the scattering contribution of the lipid carrier in small-angle neutron scattering. The first step to achieve a neutron invisible carrier system is the development of a large-scale expression protocol of match-out deuterated Saposin A. Then, to incorporate MsbA into a matched-out deuterated lipid carrier combining MsbA, deuterated Saposin A and fractional deuterium labelled 1-palmitoyl-2-oleoyl-glycero-3-phosphocholine (POPC) lipids to measure the neutron scattering in 100% D₂O where only the membrane protein contributes to the scattering signal.

In addition, the aim was to understand better the reaction cycle of the MsbA using cryo-EM and time-resolved SAXS experiments. In order to gain detailed insights into the nucleotide binding and other conformational states of MsbA in combination with ATP-Mg²⁺.

2 Material and Methods

2.1 Chemical reagents

Unless otherwise stated, all reagents and chemicals were purchased from Sarstedt, Carl Roth, Sigma-Aldrich and Thermo Fisher Scientific. Hazardous and toxic chemicals were handled and disposed according to the safety instructions (see section 5) and are listed in Table 14.

2.2 Bacteria and cell lines

All bacterial strains used for the expression of recombinant proteins and the production of lipids in this thesis are shown in Table 3 alongside their origins and media. Detailed compositions of culture media are listed in Table 4.

Table 3: Expression systems used in this study.

Cells	Origin	Culture Medium
AL95 (pssA::kanR lacY::Tn9 camR)	<i>E. coli</i>	D-Enfors
BL21 Gold (DE3)	<i>E. coli</i>	LB, TB
C43 (DE3)	<i>E. coli</i>	LB, 2× TY
Rosetta-gami 2 (DE3)	<i>E. coli</i>	LB, TB, 2H High Performance OD2/unlabelled High Performance OD2 mix
SHuffle® T7	<i>E. coli</i>	LB, H-Enfors, D-Enfors

2.3 Solutions and culture media

All solutions and cell culture media utilised during the study are listed in Table 4. They were prepared with deionised water. The pH values were measured using a peqMeter 1.14 (PEQLAB).

Table 4: Composition of media und solutions.

Description	Composition
2× TY	15 g/L Peptone, 10 g/L Yeast extract, 5 g NaCl
2H High Performance OD2/unlabelled High Performance OD2 mix	Ready-to-use (Silantes) mix of 75% 2H and 25% unlabelled
Coomassie staining solution	2 tablets PhastGel® Blue R 95% (v/v) Ethanol, 10% (v/v) Acetic acid

D-Enfors	6.86 g/l (NH ₄) ₂ SO ₄ , 1.56 g/l KH ₂ PO ₄ , 6.48 g/l Na ₂ HPO ₄ ·2H ₂ O, 0.49 g/l diammonium hydrogen-citrate, 0.25 g/l MgSO ₄ ·7H ₂ O, 1.0 ml/l of a salt mix (0.5 g/l CaCl ₂ ·2H ₂ O, 16.7 g/l FeCl ₃ ·6H ₂ O, 0.18 g/l, ZnSO ₄ ·7H ₂ O, 0.16 g/l CuSO ₄ ·5H ₂ O, 0.15 g/l MnSO ₄ ·4H ₂ O, 0.18 g/l CoCl ₂ ·6H ₂ O, 20.1 g/l EDTA, dissolved in D ₂ O, 12% (v/v) glycerol
H-Enfors	6.86 g/l (NH ₄) ₂ SO ₄ , 1.56 g/l KH ₂ PO ₄ , 6.48 g/l Na ₂ HPO ₄ ·2H ₂ O, 0.49 g/l diammonium hydrogen-citrate, 0.25 g/l MgSO ₄ ·7H ₂ O, 1.0 ml/l of a salt mix (0.5 g/l CaCl ₂ ·2H ₂ O, 16.7 g/l FeCl ₃ ·6H ₂ O, 0.18 g/l, ZnSO ₄ ·7H ₂ O, 0.16 g/l CuSO ₄ ·5H ₂ O, 0.15 g/l MnSO ₄ ·4H ₂ O, 0.18 g/l CoCl ₂ ·6H ₂ O, 20.1 g/l EDTA, dissolved in H ₂ O, 12% (v/v) glycerol
LB (Lysogeny Broth) Lennox medium	20 g/L LB-Lennox medium (Roth X964.4), add 15 g/L Agar-Agar for LB-Agar plates
SDS gel destaining solution	25% (v/v) Isopropanol, 10.4% (v/v) Acetic acid
SDS sample buffer 1x	1% (w/v) SDS, 8% (v/v) Glycerol, 50 mM Tris pH 7, 1% (v/v) 2-Mercaptoethanol, 0.01% (w/v) Bromophenol blue
SDS-PAGE running buffer 1x	25 mM Tris base (3 g/L), 192 mM Glycine (14.4 g/L), 0.1% (w/v) SDS
TB (Terrific Broth) medium	12 g/L Peptone, 24 g/L Yeast extract, 4 mL/L Glycerol
TB Buffer	0.17 M KH ₂ PO ₄ , 0.72 M K ₂ HPO ₄

2.4 Expression und purification of MsbA

msbA gene from *E. coli* BL21 DE3, cloned with an N-terminal His₆-Tag in a pNEK vector was expressed in the *E. coli* strain C43¹²⁷. In 2x TY media at 37 °C, the cells were grown until they reached an OD₆₀₀ of ~1.5, and the temperature was decreased to 20 °C. After reaching 20 °C, the protein expression was induced with 0.1 mM isopropyl-β-D-1-thiogalactopyranoside (IPTG) overnight.

After centrifugation (5000 x g, 20 min, 4 °C) and discarding the supernatant, the biomass was resuspended in lysis buffer (30 mM Tris pH: 8.0, 300 mM NaCl, 10% glycerol, 5 mM MgCl₂) and disrupted in a high-pressure homogenizer (EmulsiFlex-C3; Avestin, Ottawa, ON, Canada). The lysis was spun down at 20000 x g for 25 min at 4 °C, and a second centrifugation step (100000 x g for 100 min at 4 °C) was done to obtain the membrane fractions. First, the solubilization of the membrane was performed in a buffer containing 1% (w/v) DDM, 30 mM

Tris (pH 8), 300 mM NaCl, 10% glycerol, 10 mM imidazole by stirring for 90 min at 4 °C. In the next step, pre-equilibrated Ni-nitrilotriacetic acid (Ni-NTA) resin was added to the solubilized proteins and incubated for 60 min at 4 °C. Next, the resin was washed with 1% (w/v) DDM in 30 mM Tris pH: 8, 300 mM NaCl and 10 mM imidazole, followed by additional washing steps with a decreased DDM and an increasing imidazole concentration (0.03% DDM, 30 mM Tris pH: 8, 300 mM NaCl, 10/30 mM imidazole). Next, MsbA was eluted in the same buffer with an imidazole concentration of 400 mM. Fractions containing MsbA were pooled and concentrated to 2 – 5 mg/mL before reconstitution into lipidic carriers.

2.5 Expression and purification of Saposin A

Saposin A was expressed in a pNIC28-Bsa4 vector with an N-terminal His₆-tag and tobacco etch virus (TEV) cleavage site in the *E. coli* strain Rosetta-gami 2²⁹. After the OD₆₀₀ of ~1.5 was reached in terrific broth (TB) media at 37 °C, the temperature was lowered to 20 °C, and 0.1 mM IPTG was added to start the induction overnight.

After harvesting the cells (5000 x g, 20 min, 4 °C), the pellet was resuspended in lysis buffer (20 mM sodium phosphate pH 7.4, 300 mM NaCl, 5% glycerol, 15 mM imidazole) and sonicated 3× 3 min with 30% power. Next, the cell suspension was heated to 70 °C for 20 min to precipitate the thermolabile components. After a centrifugation step (16000 x g, 20 min, 4 °C), an immobilised metal affinity chromatography (IMAC) was performed. First, pre-equilibrated Ni-NTA resin was added to the supernatant of the previous centrifugation step and stirred for 90 min at 4 °C, followed by a series of washing steps with an increasing imidazole concentration (20 mM sodium phosphate pH 7.4, 300 mM NaCl, 5% glycerol, 15/30 mM imidazole). Then, the elution was performed with 20 mM sodium phosphate (pH 7.4), 300 mM NaCl, 5% glycerol, 400 mM imidazole and TEV-protease were added to the eluted protein and dialysed overnight at 4 °C against dialysis buffer (20 mM sodium phosphate pH 7.4, 300 mM NaCl, 5% glycerol, 1 mM DTT). In a second IMAC, the TEV-protease and the cleaved His₆-tag were removed. The proteins were concentrated and applied to an S75 16/600 (GE Healthcare, Chicago, IL, USA) column, and a size-exclusion chromatography (SEC) was performed (buffer: 20 mM HEPES, pH 7.4, 200 mM NaCl) to yield the purified SapA. The fractions containing the monomeric SapA were pooled and concentrated to ~4 mg/mL and stored at -80 °C.

2.6 Expression of matched-out deuterated Saposin A

Matched-out deuterated Saposin A was expressed in SHuffle *E. coli* cells with a pNIC28-Bsa4 vector. The adaptation to deuterated minimal media was performed several stages¹²⁸ to 85%

deuterated D-Enfors minimal media (6.86 g/l $(\text{NH}_4)_2\text{SO}_4$, 1.56 g/l KH_2PO_4 , 6.48 g/l $\text{Na}_2\text{HPO}_4 \cdot 2\text{H}_2\text{O}$, 0.49 g/l diammonium hydrogen-citrate, 0.25 g/l $\text{MgSO}_4 \cdot 7\text{H}_2\text{O}$, 1.0 ml/l of a salt mix (0.5 g/l $\text{CaCl}_2 \cdot 2\text{H}_2\text{O}$, 16.7 g/l $\text{FeCl}_3 \cdot 6\text{H}_2\text{O}$, 0.18 g/l, $\text{ZnSO}_4 \cdot 7\text{H}_2\text{O}$, 0.16 g/l $\text{CuSO}_4 \cdot 5\text{H}_2\text{O}$, 0.15 g/l $\text{MnSO}_4 \cdot 4\text{H}_2\text{O}$, 0.18 g/l $\text{CoCl}_2 \cdot 6\text{H}_2\text{O}$, 20.1 g/l EDTA, 10 $\mu\text{g}/\text{mL}$ kanamycin dissolved in D_2O) using 12% glycerol as carbon source. After incubation for 24 h at 37 °C, the temperature was decreased to 20 °C, and the protein expression was induced with 0.1 mM IPTG. The cells were incubated for another 24 h and afterwards harvested. The protein was purified with the established protocol described in 2.5.

2.7 Growing, extraction, and purification of matched-out deuterated phosphatidylcholine (dPC)

Selectively deuterated mixed acyl phosphatidylcholine (dPC) was produced in the *E. coli* strain AL95 which carries the plasmid pAC-PCSlp-Sp-Gm (ParaB-pcs SpR GmR) to allow the production of a PC synthase controlled of an arabinose inducible promotor. The adaptation to deuterated minimal media was performed in a multi-step process, a modified method by Artero *et al.*¹²⁸ to 100 % deuterated D-Enfors minimal media (6.86 g/l $(\text{NH}_4)_2\text{SO}_4$, 1.56 g/l KH_2PO_4 , 6.48 g/l $\text{Na}_2\text{HPO}_4 \cdot 2\text{H}_2\text{O}$, 0.49 g/l diammonium hydrogen-citrate, 0.25 g/l $\text{MgSO}_4 \cdot 7\text{H}_2\text{O}$, 1.0 ml/l of a salt mix (0.5 g/l $\text{CaCl}_2 \cdot 2\text{H}_2\text{O}$, 16.7 g/l $\text{FeCl}_3 \cdot 6\text{H}_2\text{O}$, 0.18 g/l, $\text{ZnSO}_4 \cdot 7\text{H}_2\text{O}$, 0.16 g/l $\text{CuSO}_4 \cdot 5\text{H}_2\text{O}$, 0.15 g/l $\text{MnSO}_4 \cdot 4\text{H}_2\text{O}$, 0.18 g/l $\text{CoCl}_2 \cdot 6\text{H}_2\text{O}$, 20.1 g/l EDTA, 10 $\mu\text{g}/\text{mL}$ gentamicin) with deuterated d_8 -glycerol as a carbon source. The dPC production was induced with 0.2 % unlabelled arabinose and 2 mM fractionally deuterated choline chloride (trimethyl- d_9 , 98 %; Eurisotop). After incubation at 37 °C for 48 h, the cells were centrifugated (10000 x g, 20 min, 4 °C) and washed with H_2O ⁸¹.

The extraction of the total phospholipids was performed using a modified method of Bligh and Dyer. 5 g of cell paste was resuspended in 10 mL H_2O and sonicated (3x 5 min, 6 s on followed by 3 s off, 3 min off between each 5 min, with 20% power) on ice. The cell lysate was boiled in 100 mL absolute ethanol (EtOH) containing 1% butylated hydroxytoluene (BHT) at 95 °C for 5 min with vigorous stirring to denature lipases. The lysate was cooled down on ice for 15 min. 110 mL methanol (MeOH) and 50 mL chloroform (CHCl_3) were added and stirred overnight at 4 °C. The phase separation was induced by adding 200 mL of CHCl_3 and 50 mL of H_2O . The organic phase was collected, and the aqueous phase was reextracted with 50 mL CHCl_3 and 10 mL H_2O . The pooled organic phase was evaporated and resuspended in 25 mL hexane.

The solid phase extraction (SPE) was performed to separate the phospholipids according to the different head groups. The sample was distributed to four gravity flow columns filled with ~3 mL equilibrated Silica gel 60 (0.040-0.063 mm) and to each column 25 mL of running solvent containing different ratios of CHCl₃:MeOH (20:1, 15:1, 12:1, 9:1, 6:1, 4:1, 2:1, 1:1, 100% MeOH, v/v) was applied. Each elution was collected and 1 mL EtOH with 1% BHT was added to avoid oxidation.

The results of the SPE were characterised by high-performance thin-layer chromatography (HPTLC) and compared to known standards. The samples and standards were sprayed on a TLC Silica gel 60 glass plate using a CAMAG automatic TLC sampler 4 (CAMAG, Muttenz, Switzerland) and developed with the running solvent CHCl₃:MeOH:Acetic acid 65:28:8, v/v/v. Lipids were stained by primuline solution¹²⁹ (0.05% primuline in acetone:H₂O 8:2, v/v) and analysed under UV light.

The mixed fractions of dPC and other phospholipids were further purified using high-pressure liquid chromatography (HPLC). First, the sample was passed through a diol-modified silica stationary phase column coupled to a High-performance Liquid Chromatography-Evaporative light scattering detector (HPLC-ELSD) (Agilent 1260, United Kingdom). The mobile phase employed was a gradient between solvent A (CHCl₃/CH₃OH/NH₄OH, 80:20.5:0.5, v/v) and solvent B (CHCl₃/CH₃OH/H₂O/NH₄OH, 60:35:5.5:0.5, v/v).

2.8 Reconstitution of MsbA into membrane scaffold based nanodiscs and Salipro nanoparticles

To reconstitute MsbA into Salipro nanoparticles (Salipro), lipids were resuspended in 100 mM cholate to obtain a 50 mM POPC stock solution. Next, in a molar ratio of 1:4:20 (MsbA:SapA:lipids) in a buffer containing 20 mM HEPES, pH 7.4, 200 mM NaCl was mixed and incubated at 4 °C for 30 min. The Salipro formation was initiated by adding 0.8 g/mL equilibrated Biobeads to the mixture and constant agitation overnight at 4 °C. After the Biobead removal, the reconstituted MsbA was concentrated and purified to an S200 column (GE Healthcare) with a buffer containing 20 mM HEPES pH 7.4, 200 mM NaCl. The reconstitution of MsbA into nanodiscs was performed in a molar ratio of 1:1:25 (MsbA:MSP1D1:POPC). The other steps for reconstitution and purification were identical to Salipro.

2.9 Small-angle neutron scattering (SANS)

The contrast variation experiments of MsbA in Salipro were performed using the small-angle scattering instrument D11¹³⁰ at the Institute Laue-Langevin (ILL, Grenoble, France). Data

recorded using D11 at ILL were measured in two different configurations of 2.5 m / 2 m and 16.5 m / 16.5 m (collimation length / sample-detector distances) to cover a wide q -range ($0.004 < q > 0.351 \text{ \AA}^{-1}$) with a fixed neutron wavelength of 4.6 Å. The measurements were performed in 100%, 42%, 8% D₂O buffer (30 mM Tris pH 7.5, 150 mM NaCl) and 100% H₂O buffer (30 mM Tris pH 7.5, 150 mM NaCl) at 1-6 mg/ml protein concentration at 10 °C.

The other measurements were performed at the SANS-I instrument at the Paul Scherrer Institut (PSI, Villigen, Switzerland). Measurements at SANS-I were performed at a constant wavelength of 0.60 nm at a sample-detector distance of 1.5 m, 6 m and 18 m with a beam collimated at 4.5 m, 6 m and 18 m, respectively. The measurements were performed in 100% D₂O buffer (30 mM Tris pH 7.5, 150 mM NaCl) at 1-3 mg/ml MsbA-Salipro protein concentration at 17 °C. The radii of gyration were extracted by the Guinier approximation. The program GNOM¹³¹ was used to calculate the distance distribution function ($P(r)$) and the maximal protein dimension (D_{max}) from the scattering curve.

Water reference, buffers, empty cell, the direct beam, and the total absorber boron-cadmium were measured to perform data reduction using the GRASP software to obtain one-dimensional scattering intensities $I(q)$. The scattering curve of the samples was buffer subtracted using PRIMUS¹³² and the extraction of radii of gyration was done by the Guinier approximation. The R_g and scattering intensities were back-calculated from the cryo-EM model of MsbA (PDB: 7bcw¹³³) using the programme PEPSI¹³⁴ and scored in a χ^2 fit against the experimental data. Finally, the electron density *ab initio* shape reconstruction was performed with the software DENSS¹³⁵ from the experimental SANS data.

2.10 Small-angle X-ray scattering (SAXS)

MsbA in Salipro nanoparticles in the apo and the ADP-Vi state was characterized by small-angle X-ray scattering (SAXS) using the Bio-SAXS beamline P12⁵² on the storage ring PETRA III (EMBL/DESY, Hamburg, Germany). The scattered intensity was recorded as a function of the scattering vector q with $q = 4\pi\sin\theta/\lambda$, using a wavelength of 0.124 nm. The calibration of the scattering intensity into absolute units of cm^{-1} was performed using the bovine serum albumin (BSA) forward scattering intensity. All measurements were performed at 10 °C in 20 mM HEPES, pH 7.4, and 200 mM NaCl, with protein concentrations of 1-5 mg/ml. The normalization and the background subtraction were performed by the automatic procedures on the beamline¹³². The radii of gyration were extracted by the Guinier approximation. The program GNOM¹³¹ was used to calculate the distance distribution function ($P(r)$) and the maximal protein dimension (D_{max}) from the scattering curve.

For measuring the kinetics of the EQMsba mutant in MSP nanodiscs in a time-resolved SAXS experiment, the Bio-SAXS beamline P12⁵² on the storage ring PETRA III (DESY, Hamburg, Germany) was used. First, the sample was measured without Mg²⁺-ATP to obtain the scattering of the apo form of EQMsba. Afterwards, the sample was mixed in a 1:1 (v/v) ratio with 15 mM Mg²⁺-ATP, and after 5, 10, 15, 20, 30, 60, 105, 150 and 382 min, the scattering was measured to cover a wide range in the kinetics. All measurements were performed at room temperature in 20 mM HEPES, pH 7.4, and 200 mM NaCl, with protein concentrations of 1-5 mg/ml.

The time-resolved SAXS experiment of the EQMsba mutant incorporated into Salipro was performed at the bio-SAXS instrument BM29 at European Synchrotron Radiation Facility (ESRF, Grenoble, France). All the experimental parameters were identical to the time-resolved SAXS experiment of EQMsba in nanodiscs.

2.11 Stopped-flow time-resolved small-angle X-ray scattering

The stopped-flow time-resolved SAXS experiment of Msba in MSP nanodiscs was performed at the Bio-SAXS beamline P12⁵² on the storage ring PETRA III (EMBL/DESY, Hamburg, Germany). Msba in Salipro (conc.: 100 μ M) was mixed 1:1 (v/v) with Mg²⁺-ATP (conc.: 100 μ M) using a stopped-flow device, injecting 80 μ L each (Bio-logic, Seyssinet-Pariset, France). All measurements were done at room temperature, and the data was collected on the Pilatus 6M detector. The X-ray exposure time was set to 25 ms, and 24 frames were acquired for each injection. This was repeated 10-times and summed up for the corresponding time intervals to increase the signal-to-noise ratio. These frames were analysed for radiation damage using CorMap¹³⁶. For analysing longer kinetics, delays between sample mixing and acquisition of the first frame were set up. The radii of gyration were extracted by the Guinier approximation. The program GNOM¹³¹ was used to calculate the distance distribution function (P(r)) and the maximal protein dimension (D_{max}) from the scattering curve.

2.12 Cryogenic-Electron microscopy (cryo-EM)

2.12.1 Cryo-EM grid preparation

After incorporation of Msba in Salipro particles and the following purification (see section 2.8), 4 μ L of the sample (0.6 mg/mL) was applied to a glow-discharged Quantifoil holey carbon grid R2/2 (CU, 200 mesh). The blotting and plunge-freezing in liquid ethane were performed using an FEI Vitrobot Mark IV (Thermo Fisher Scientific Ltd, Waltham, MA, USA) with zero blot force, 6 s blot time, 95% humidity at 4 °C. For analysing ADP-vanadate trapped Msba, 1 mM vanadate, 1 mM ATP and 1 mM MgCl₂ were added to the sample (0.6 mg/mL) and

incubated for 3 days at 4 °C. The following conditions, the application to the grid and the blotting, are identical to the apoprotein.

2.12.2 Cryo-EM data acquisition

Cryo-EM data was collected on the Titan Krios microscope at the ESRF¹³⁷ operated at 300 kV using EPU (Thermo Fisher Scientific) with a Quantum LS energy filter and Gatan K2 summit direct electron detector. Movies were recorded in counting mode at a nominal magnification of 165000×, with a pixel size of 0.827 Å/pixel. The defocus range was set from -0.8 to -3.0 μm and the exposure time was 5 s for each movie at a dose rate of 5.42 e⁻/pixel·s, resulting in a total dosage of 39.55 e⁻/Å² over 40 frames.

2.12.3 Image processing

The pre-processing was carried out using Scipion¹³⁸ by the scripts implemented in CM01 at the ESRF to perform beam-induced motion correction¹¹⁹ and contrast transfer function (CTF) estimation¹³⁹. Particle picking and 2D classification were carried out in crYOLO¹⁴⁰ and RELION¹⁴¹, also implemented in Scipion¹⁴². The cleaned-up set of particles was exported into cryoSPARC⁹⁸ for further processing. In a 3D classification step, the particles were further cleaned up, followed by a heterogeneous refinement step to remove bad particles. The best classes were used for a non-uniform refinement (C1), followed by a second 3D classification. Finally, a CTF refinement was carried out with the best resolving class, followed by a non-uniform refinement (C2), resulting in a final map. Post-processing and local resolution estimation were carried out in cryoSPARC (see Figure 14).

2.12.4 Model building and refinement

The MsbA coordinates of the accession number 5TTP from the Protein Data Bank (PDB) were used as a starting model. This model was placed in the cryo-EM map using UCSF ChimeraX¹⁴³ and auto-sharpened using PHENIX prior model building. (*B* factor: -94 Å²). The model was rebuilt using Coot¹⁴⁴, ISOLDE¹⁴⁵ and the PHENIX¹⁴⁶ suite. PHENIX was also used for real-space refinement and model validation^{147,148}. The final model was deposited to the PDB under accession number 7bcw.

2.13 Differential scanning fluorimetry (nDSF) using Prometheus

Differential fluorescence fluorimetry using a nanoDSF instrument (Prometheus, NanoTemper Technologies, Munich, Germany) was performed to investigate the stability of MsbA in the lipid carrier systems with different nucleotides monitoring the change of intrinsic fluorescence of tryptophan residues at 330 and 350 nm after excitation at 280 nm. 0.5 mg/mL of protein was

mixed in a forward reaction with 0.5 mM of ligand in 10 mM HEPES, pH 7.4, 150 mM NaCl, 5 mM MgCl₂ buffer and incubated for 2-3 h. The samples were loaded in capillaries (Prometheus NT.48 Capillaries nanoDSF Grade) and the temperature was increased with a heating rate of 1 °C/mL, covering a temperature range from 20 to 90 °C to measure the unfolding of the proteins. The first derivative of the unfolding curves (F350/F330) was used to determine the transition midpoint. All experiments were performed as triplicates.

2.14 Baginski ATPase activity assay

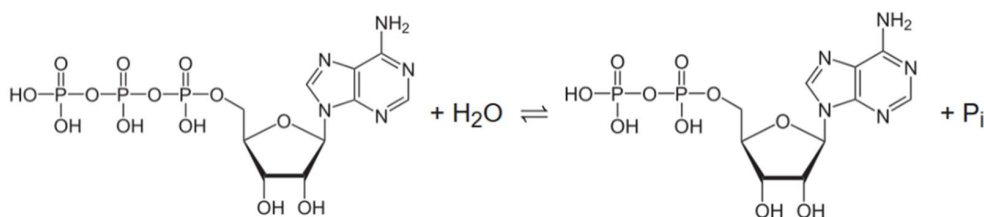


Figure 10: Hydrolysis of adenosine triphosphate (ATP) to adenosine diphosphate (ADP) and an inorganic phosphate (P_i).

For measuring the activity of MsbA in Salipro, the Baginski assay was used^{149,150}, similar to previously described in Nitsche *et al.*¹⁵¹. 5 µg MsbA in Salipro in buffer containing 30 mM Tris (pH 7.5), 150 mM NaCl and 5 mM MgCl₂ were incubated with different ATP concentrations (0/100/200/300/500/1000/2000/4000 µM) in 50 µL for 12 min at room temperature (RT). During this time, the ATPase is hydrolysing ATP to ADP and inorganic phosphate. Next, the reaction was stopped by adding 50 µL ascorbic acid solution (140 mM ascorbic acid, 0.5 M HCl, 0.1% SDS, 5 mM ammonium heptamolybdate) and after additional 10 min incubation at RT 75 µL solution B (75 mM sodium citrate, 2% (w/v) sodium metaarsenite and 2% (v/v) acetic acid) was used to stop the colorimetric reaction. After 20 min, the absorbance at 860 nm was measured using a Tecan Infinite200 microplate reader. All experiments were performed as triplicates.

2.15 Phosphate assay for determining lipid concentrations

The phosphate assay was used to determine a precise concentration of lipids by analysing the amount of phosphate after hydrolysing phospholipids. Phosphate standards with 0.0325, 0.065, 0.163 and 0.325 µmol were prepared from a 1 mM K₂HPO₄ in 0.005 N HCl stock solution in glass vials. The lipid samples were prepared with an estimated amount of phosphate in the range of the standards. Each standard and sample were prepared and measured as doublets. The solvents of all vials were evaporated. 0.45 mL H₂SO₄ (8.9 N) was added to each vial and heated to 200 °C for 60 min. The vials were cooled down for 5 min before adding 50 µL of 30% H₂O₂. The standards and samples were heated at 200 °C for another 30 min. The vials were cooled

down to room temperature. 3.9 mL deionised water and 0.5 mL ammonium molybdate tetrahydrate solution (2.5%, w/v) were added and mixed. 0.5 mL ascorbic acid (10%, w/v) was added, mixed, and heated to 100 °C for 7 min to develop and stabilise the colourimetric reaction. The absorbance at 820 nm was measured for all standards and samples. A linear fit from the absorbance of the phosphate standards was created and the amount of phosphate in the samples was calculated, leading to the lipid concentration.

3 Results and Discussion

3.1 Chapter 1 – Cryo-EM structure of MsbA in Salipro nanoparticles

3.1.1 Cryo-EM structure of ADP-vanadate trapped MsbA in Salipro provides insights into nucleotide coordination

The following chapter is based on:

Kehlenbeck, D.-M., Traore, D.A., Josts, I., Sander, S., Moulin, M., Haertlein, M., Prevost, S., Forsyth, V.T. and Tidow, H. (2022), Cryo-EM structure of MsbA in saposin-lipid nanoparticles (Salipro) provides insights into nucleotide coordination. FEBS J. <https://doi.org/10.1111/febs.16327>

The structure of MsbA has been studied in different states and reconstitution systems. However, due to the limited resolution, a detailed understanding of nucleotide binding to MsbA has remained elusive. MsbA was reconstituted into Salipro nanoparticles to analyse the structure of the ADP-vanadate trapped state of MsbA by using single-particle cryo-electron microscopy to 3.5 Å resolution. This resolution enables a detailed view on the exact nucleotide coordination inside the binding pocket and the modelling of most side chains.

MsbA from *E. coli* C43 cells was purified with dodecyl maltoside (DDM) and reconstituted into Salipro using 1-palmitoyl-2-oleoyl-glycero-3-phosphocholine (16:0–18:1 PC) (POPC). The molar ratio of 1:4:20 (MsbA:SapA:POPC) yields a monodisperse sample. The assembly was controlled and analysed by size-exclusion chromatography (SEC) and SDS-PAGE (Figure 11A). In the SEC profile of the assembly, only one peak at 12 mL with a small shoulder of slightly larger particles at 10 mL is visible. Elution fractions from the prominent peak were pooled and analysed by SDS PAGE. The Coomassie-stained gel shows two bands corresponding to MsbA and SapA, confirming the successful reconstitution of MsbA into Salipro.

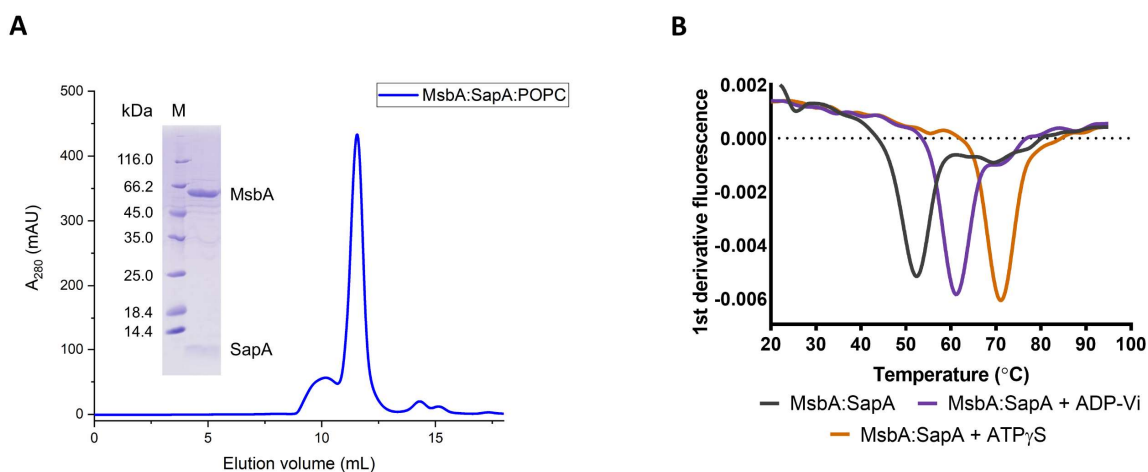


Figure 11: Characterisation of Salipro-embedded MsbA. **A:** SEC profile and corresponding SDS-PAGE gel showing the reconstitution of MsbA into Salipro. **B:** Thermal melt profiles from nDSF from apo MsbA (grey), MsbA with ADP-Vi (violet) and MsbA with ATP γ S (orange), illustrating a significant stabilisation of MsbA by nucleotides.

The reconstituted sample was characterised by analysing the thermostability of the complex. Orthovanadate (Vi) was used to mimic the transition state after ATP-hydrolysis by trapping the Mg²⁺-ADP-Vi complex in the catalytic site of MsbA. In this trapped state, the stability of MsbA in Salipro is significantly increased compared to apo MsbA. The change in the ratio of F350/F330 nm indicated a change in the solvent accessibility of tryptophan residues. From this change, the melting point of the protein can be calculated. The melting point describes the temperature where folded and unfolded proteins are present in the same concentration. The melting temperature for apo MsbA is 53 °C (black), increases to 62 °C with the Mg²⁺-ADP-Vi complex (purple) and 71 °C for MsbA with ATP γ S (orange, Figure 11B). MsbA reconstituted into Salipro retained its specific ATPase activity measured using the Baginski assay (Figure 12A), showing the typical hyperbolic profile for ATPases. MsbA hydrolyses ATP to ADP and inorganic phosphate during the transport process. In the Baginski assay, the ammoniumheptamolybdate builds a complex with the released inorganic phosphate and the ascorbic acid. This complex stains the solution, and the absorbance is measured at 860 nm. The structural differences of MsbA in Salipro in the apo and in ADP-Vi trapped occluded state were analysed using SAXS. Significant differences were detected in the mid-q region from 0.5 – 3 nm⁻¹. The distance distribution plots show a very similar curve progression. The R_g of the apo state with 46.5 ± 0.02 Å and 46.6 ± 0.02 Å for the ADP-Vi trapped state are very similar and the D_{max} is with 18.0 nm identical, indicating the differences refer to internal structural rearrangements.

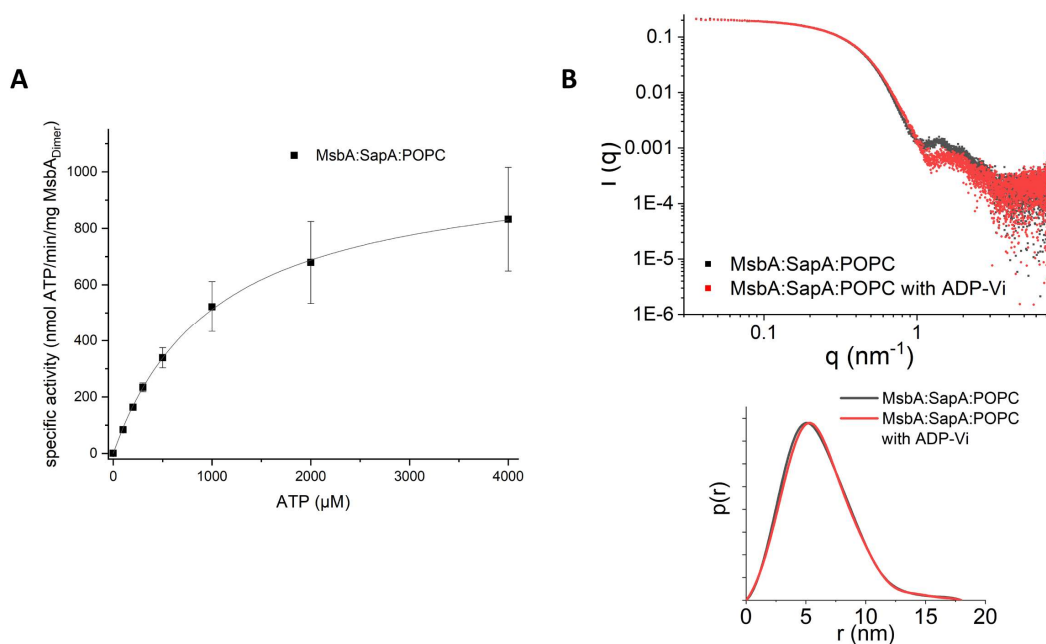


Figure 12: Characterisation of MsbA incorporated into Salipro. **A:** Activity measured by the Baginski assay. The maximal reaction speed (V_{\max}) of MsbA in Salipro with POPC is 1110 ± 292 nmol ATP \cdot min $^{-1}\cdot$ mg $^{-1}$ enzyme and the Michaelis (K_m) constant is 1050 ± 289 μ M. The experiment was performed at RT in triplicates. **B:** SAXS profiles of MsbA in Salipro with (red) and without (black) ADP-Vi. Scattering shows differences in the mid q -range, illustrating structural differences between the two states of MsbA. In addition, the distance distribution plots look identical, indicating internal structural rearrangements between the two measured states.

We were measuring the ADP-Vi trapped state of MsbA in Salipro because due to the increased thermal stability and the lower flexibility of the protein we were hoping for a high-resolution cryo-EM structure, highlighting key residues involved in nucleotide binding. POPC was used in the Salipro-reconstitution due to the high stability²¹ and potential comparison to stealth carrier SANS data⁷⁹.

Table 5: Cryo-EM data collection parameters.

	EMDB: 12145 PDB: 7bcw
Data	
Magnification	165 000
Voltage (kV)	300
Electron exposure (e-/Å ²)	39.55
Defocus range (μ m)	-0.8 to -3.0
Pixel size (Å)	0.827
Symmetry imposed	C2
Final particle images (no.)	83278
GS-FSC resolution at 0.143 (Å)	3.5
Initial model used	PDB: 7bcw

Map sharpening <i>B</i> factor (Å ²)	-94
Model	
FSC model (0/0.173/0.5)	3.0/3.3/3.6
Nonhydrogen atoms	9023
Protein residues	1148
Ligands	VO ₄ (2), POV (2), ADP (2)
Bond (RMSD)	
Length (Å)	0.005
Angles (°)	0.663
MolProbity score	1.77
Clash score	9.26
Rotamer outliers (%)	0
Ramachandran plot	
Favoured (%)	95.72
Allowed (%)	4.28
Outliers (%)	0
EMRinger score	2.27

The cryo-EM data was collected by Dr Daouda A.K. Traore on the Titan Krios microscope at the ESRF¹³⁷. All data collection parameters are summarised in Table 5. After the data collection, the recorded movies were pre-processed via motion correction¹¹⁹, CTF estimation¹³⁹ and particle picking¹⁴⁰. Next, two rounds of 2D classification of the picked particles were performed (Figure 13A). After 3D classifications and further refinements, a final map with a resolution of 3.5 Å at gold standard FSC 0.143 was obtained (Figure 13B). With this high resolution, reconstructing the transmembrane helices and the NBDs, including side chains was possible (Figure 13C).

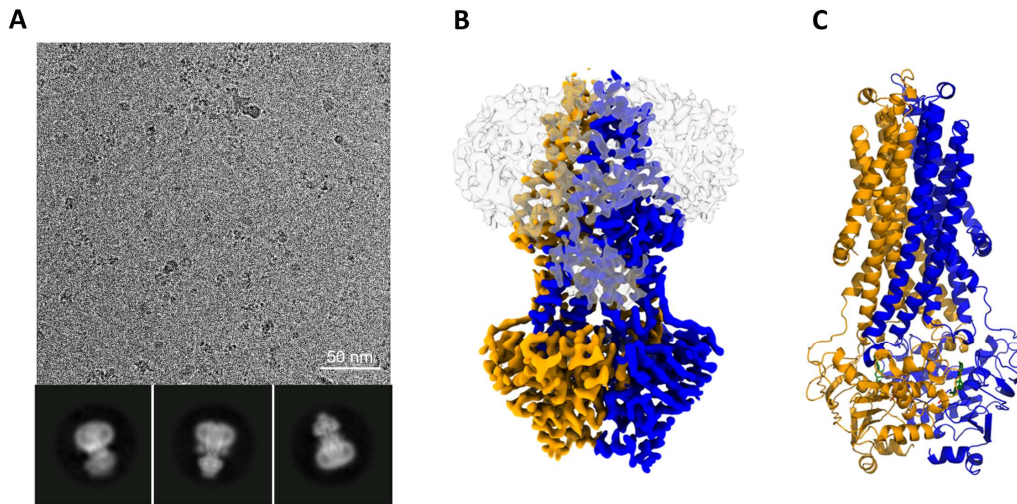


Figure 13: Cryo-EM characterisation of MsbA in Salipro. **A:** Representative cryo-EM image and selected 2D averages of Salipro-embedded MsbA. Box dimension of 2D averages: 183 Å. **B:** The surface representation of MsbA in a 3D reconstruction is filtered to 3.5 Å resolution. MsbA subunits are coloured blue and orange. The Salipro is shown in a grey outline. **C:** Ribbon diagram of MsbA embedded in Salipro.

The data processing pipeline is shown in Figure 14. First, 10302 movies were collected and processed using motion correction and CTF estimation (A). Next, 679185 particles were picked from the micrographs and classified in two rounds in 2D ($T = 13$) to remove junk particles (B). The remaining 230352 particles were further filtered in a first 3D classification step ($T = 5$) (C). Particles from the two best classes were refined separately or combined to yield a reconstruction of 7.82 Å for class 1, 3.98 Å for class 2 and 4.22 Å for the combination of classes 1 and 2 (D). Afterwards, a second 3D classification of particles belonging to class 2 was performed to remove more junk particles, resulting in a final set of 83278 particles (E). After several refinement steps, a final 3D reconstruction map of 3.46 Å (GSFC 0.143) was obtained (F). Dr Daouda A.K. Traore contributed significantly to the final cryo-EM structure.

Data processing pipeline

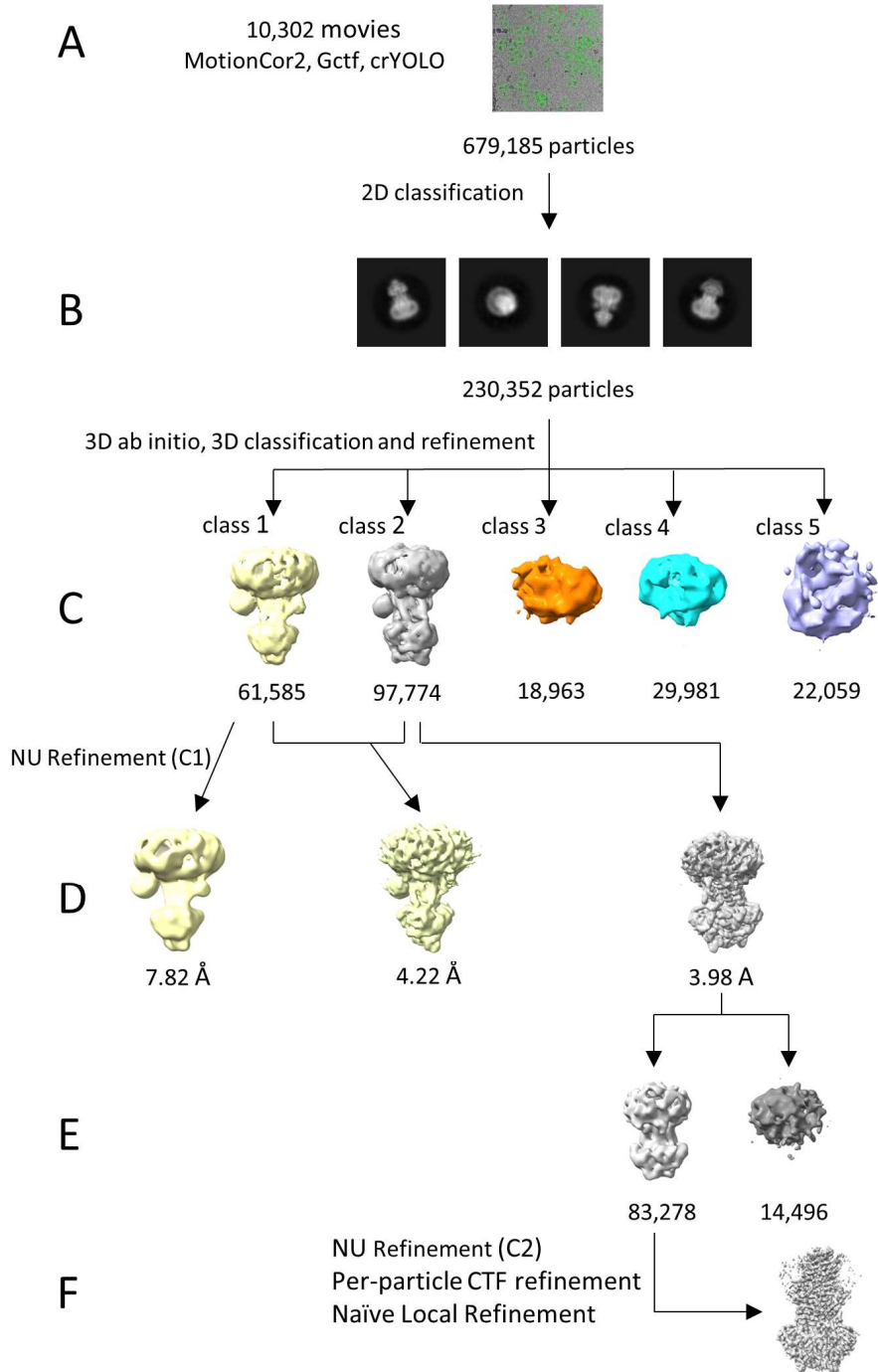


Figure 14: Image processing workflow. **A:** Starting with 10302 movies, the pre-processing, including motion correction and CTF estimation, was done in Scipion, followed by particle picking in crYOLO resulting in 679185 picked particles. **B:** The picked particles were subject to two rounds of 2D classification ($T = 13$) to remove junk particles. **C:** Selected particles were further cleaned up by a round of 3D classification ($T = 5$). **D:** Particles within the best 3D classes (classes 1 and 2) were further refined separately or merged. Here, using the reconstruction from particles that belong to class 1 reached 7.4 Å; reconstruction with particles class 2 reached 4.0 Å and the merged particles from both classes reached 4.2 Å. **E:** Afterwards, a second 3D classification was performed using class 2 particles, which yielded a final set of 83278 particles. **F:** After several refinement steps, the final 3D reconstruction map reached a resolution of 3.46 Å (GSFC 0.143).

The local resolution map is shown in Figure 15. The map is coloured according to the local resolution with high-resolution areas (2.5 Å) shown in blue to areas with lower resolution (4.5 Å) in red. The central region of MsbA has a higher local resolution than most parts located outside of MsbA. The corresponding FSC plots of the refined model against the unmasked (black), masked (red) full map and the map of half A (unmasked: blue, masked: green) and half B (unmasked: purple, masked: yellow).

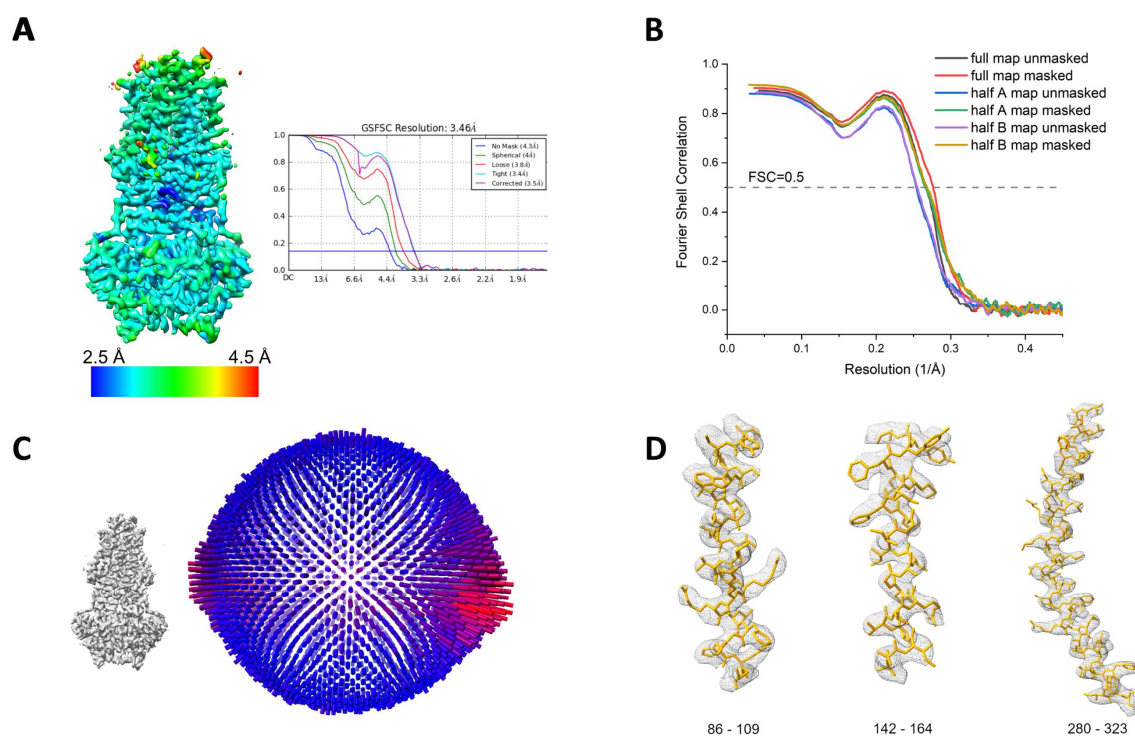


Figure 15: Single-particle cryo-EM analysis of MsbA in Salipro. **A:** Final 3D reconstruction filtered to 3.5 Å resolution, coloured to the local resolution and corresponding FSC curves. **B:** FSC curves of the refined model versus the unmasked (black) and masked (red) full map and the map half A (unmasked: blue, masked: green) and B (unmasked: purple, masked: yellow). **C:** Angular distribution of the particles included in the final reconstitution. **D:** Selected cryo-EM densities (grey mesh) with the atomic model in orange.

Due to the limited resolution in previous cryo-EM structures of MsbA, many side chains could not be modelled¹⁷. Our higher-resolution map made it possible to resolve most side chains across the entire protein. In Figure 15D selected densities are shown (grey), representing the high-resolution map superimposed on the atomic model in orange. Figure 16 illustrates that both NBDs coloured in blue and orange are involved in coordinating ADP, Vi, and Mg²⁺. Figure 16B shows for example the hydrogen bonds between vanadate with A510 of chain B and H537 of chain A, confirming that both NBDs are dimerising during nucleotide binding.

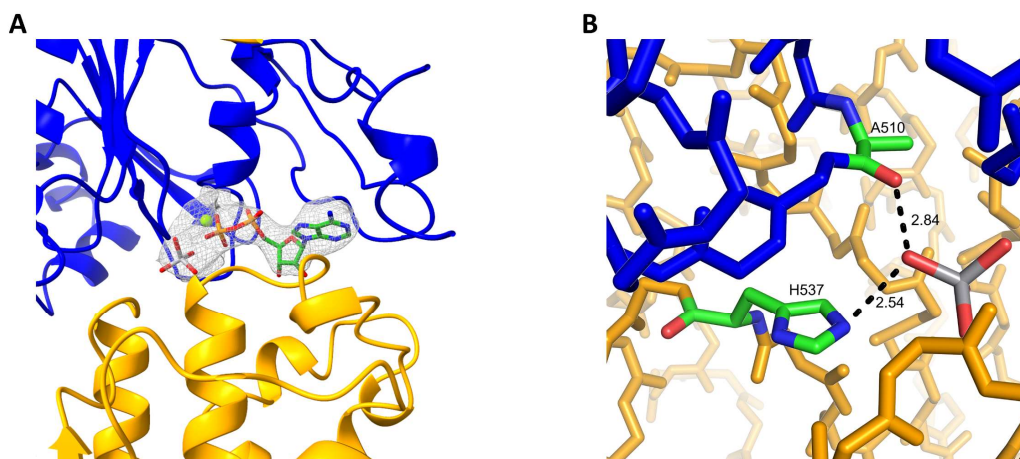


Figure 16: ADP and vanadate coordination to the NBD of MsbA. **A:** Density of the complex of ADP-Vi and Mg^{2+} in grey mesh between the two NBD of MsbA. **B:** Detailed coordination of vanadate to A510 of chain B (blue) and H537 of chain A (orange).

In Figure 17 the precise coordination of Mg^{2+} , ADP and Vi between the two NBDs is illustrated. The binding pocket for ADP is formed of D117 (chain A), Q485 (chain B), S380 (chain A), K382 (chain A), S383 (chain A) and T384 (chain A). In addition, a π - π stacking interaction of Y351 (chain A) stabilises the adenosine. Vanadate is also coordinated between the two NBDs with A510 (chain B) and H537 (chain A), G483 (chain B), K382 (chain A), S378 (chain A) and S482 (chain B). The Mg^{2+} is coordinated between the vanadate, ADP, S383 (chain A) and Q424 (chain A).

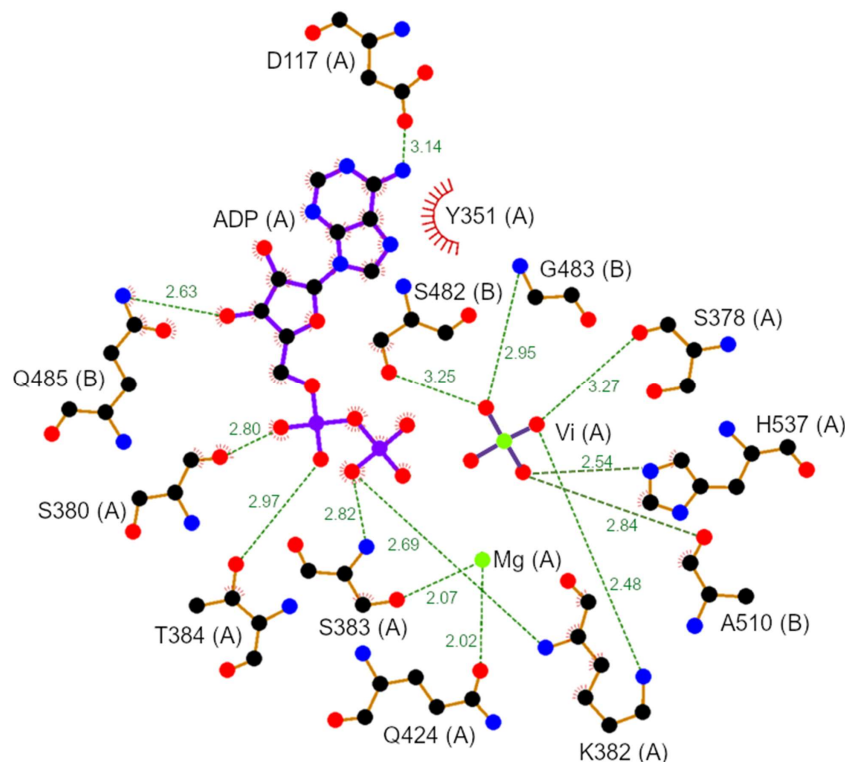


Figure 17: Coordination of ADP, vanadate and Mg^{2+} in the catalytic site of MsbA. ADP (chain A) coordinates via π - π stacking with Y351 (chain A) as well as hydrogen bonds to D117 (chain A), Q485 (chain B), S380 (chain A), T384 (chain A), S383 (chain A), which is also coordinating the Mg^{2+} and K382 (chain A), which is also coordinating the vanadate. The vanadate (A) is coordinated to H537 (chain A), A510 (chain B), S482 (chain B), S378 (chain A) and G483 (chain B).

The improved resolution also allows the modelling of a lipid molecule bound in the binding pocket between the transmembrane helices TM3, TM4, TM6 and the N-terminus (Figure 18). TM4 and TM6 are crucial in switching from the apo to the ADP-Vi-trapped state¹⁵². One possible explanation for the odd position of the lipid is that this modelled lipid is not derived from the Salipro assembly. Therefore, it could be co-purified with MsbA and has a stabilising role for MsbA. Recently an increase of the thermal stability of MsbA in combination with various classes of phospholipids could be confirmed²¹.

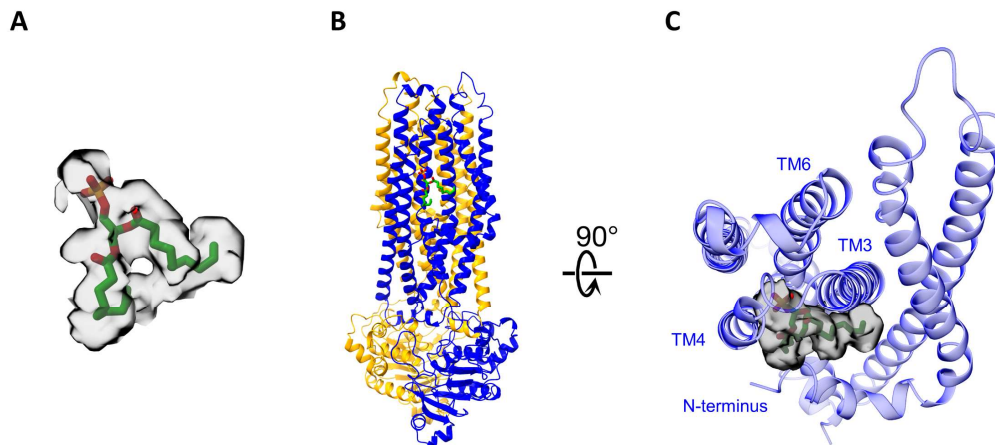


Figure 18: Detailed view of a lipid bound to the TMD of MsbA. **A:** Density superimposed to the lipid model. **B:** Location of the lipid. **C:** Location of the lipid bound between the transmembrane helices TM3, TM4, TM6 and the N-terminus. Lipid is shown in sticks, the corresponding density in a grey surface and the subunits of MsbA in blue and orange.

Several MsbA structures in different conformational states have been determined over the last decade by X-ray crystallography or single-particle cryo-electron microscopy. These states range from the inward-open (pdb: 5tv4¹⁷, 6o30²⁰, 6bl6²⁰, 3b5x¹⁶, 3b5w¹⁶, 6bpl¹⁹, 6bpp¹⁹, 6uz2¹⁵³, 6uzl¹⁵³) via occluded (pdb: 5ttp¹⁷) to outward-open state (pdb: 3b5y¹⁶, 3b60¹⁶, 3b5z¹⁶). The structure from this work can be classified as an occluded state similar to the structure 5ttp (RMSD: 2.4 Å) (see Figure 19A). The resolution of the crystal structure of ADP-Vi trapped MsbA from *Salmonella typhimurium* (pdb: 3bz5) is limited to 4.2 Å, which only allowed the modelling of the protein backbone. This structure was crystallised in undecyl-β-D-maltoside detergent in contrast to MsbA structures from our work and 5ttp. Interestingly, the structures show significant differences in the orientation of the transmembrane helices, in particular on the periplasmic site. The structure 3b5z is therefore classified as outward open, while both MsbA structures embedded in lipids are in an occluded state. The higher flexibility of detergents might allow MsbA to transition to the outward open state, while lipid carrier discs are not flexible enough to reach this conformation while ADP-Vi is bound.

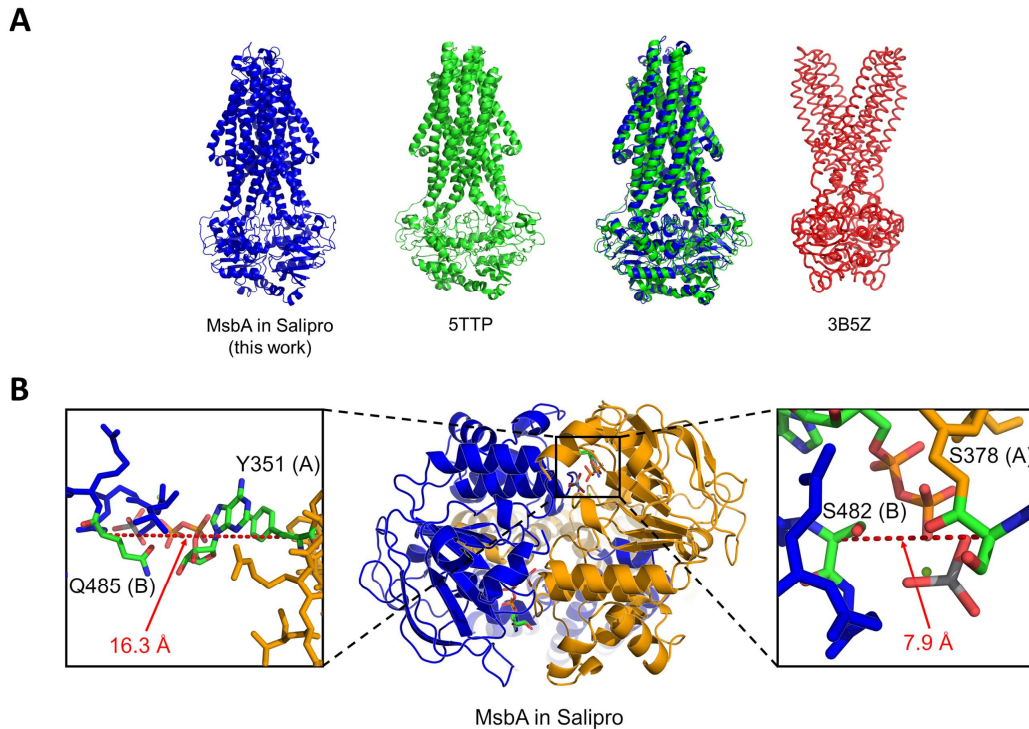


Figure 19: Comparison of ADP-Vi trapped MsbA incorporated into Salipro with existing MsbA structures. **A:** Comparison of MsbA with ADP-Vi in Salipro (this study, blue) and nanodiscs (pdb: 5ttp, green)¹⁷ as well as with the crystal structure in detergent (pdb: 3b5z, red)¹⁶. **B:** View from the cytoplasm to the ADP-Vi-bound MsbA in Salipro with C-alpha distances between S482 (Walker A motif) and S378 (signature motif) of opposing NBD. Furthermore, the C-alpha distance between Y351 and Q485 from the different chains is shown.

For efficient nucleotide binding and hydrolysing of ATP in ABC transporters, the Walker A and signature motifs of the opposing NBD must come together¹⁵⁴. Therefore, the distance between S482 (Walker motif) and S378 (signature motif) of our occluded MsbA should be shorter than the inward open state and similar to the outward open structures. The C-alpha distance of these two motifs (Walker motif chain B, signature motif chain A) is 7.9 Å for our structure in Salipro (Figure 19B), 6.2 Å for the ADP-Vi-bound (occluded state) cryo-EM structure in nanodiscs (pdb:5ttp)¹⁷, 6.0 Å for the ADP-Vi-bound and 7.5 Å for the AMPPNP-bound (outward-open) crystal structures, respectively, in detergent (pdb: 3b5z/3b60)¹⁶. Equally, the C-alpha distance of Y351 (chain A) and Q485 (chain B) is 16.3 Å in Salipro (Figure 19B), 15.8 Å for 5ttp¹⁷ and 18.0/16.8 Å for 3b5z/3b60¹⁶. Compared to the AMPPNP-bound outward open crystal structure of MsbA (pdb: 3b60), the structure from this work reveals only minor differences in the analysed C-alpha distances of key amino acids and also in the whole NBDs (RMSD: 1.0 Å). One minor difference is the side chain of Glu424, which coordinates the Mg²⁺ in our structure, while it adopts a different rotamer in pdb:3b60. In general, the NBDs in our structure are closer together than pdb: 3b60 due to the different orientation of loop T350-P357. The similarities between amino acid distances in the NBDs of

the occluded and the outward open state indicate that the NBDs do not undergo significant rearrangements during the transition from the occluded to the outward open state.

We were able to gain an improvement in the resolution of MsbA trapped with ADP-Vi in Salipro compared to MSP nanodiscs. However, this reason for this difference in resolution when using different carrier systems is still not understood and shows that many different reconstitution systems have to be tried to obtain the best resolution for any membrane protein of interest.

3.1.2 Cryo-EM analysis confirms increased flexibility of apo MsbA in Salipro

We not only analysed the ADP-Vi trapped state but also the apo state of MsbA by cryo-EM. This study aims to visualise the apo state and describe the inward open conformation of MsbA in a lipid environment. The cryo-EM data collection was performed by Dr. Daouda A.K. Traore on the Titan Krios at the ESRF¹³⁷. After the data collection, the recorded movies were motion corrected¹¹⁹ and the CTF estimation¹³⁹ was done. Then, with crYOLO¹⁴⁰, the particles were picked and a 2D classification was performed to remove junk particles. After the 2D classification, the obtained 2D class averages show MsbA from different perspectives. Interestingly, in various 2D classes, the NBDs of MsbA seem to have different distances from each other. For example, in the red-framed class in the first row, the MsbA looks much more open than the red-framed class in the fourth row (Figure 20). Due to this fact, not every MsbA protein inside Salipro has the same opening angle.

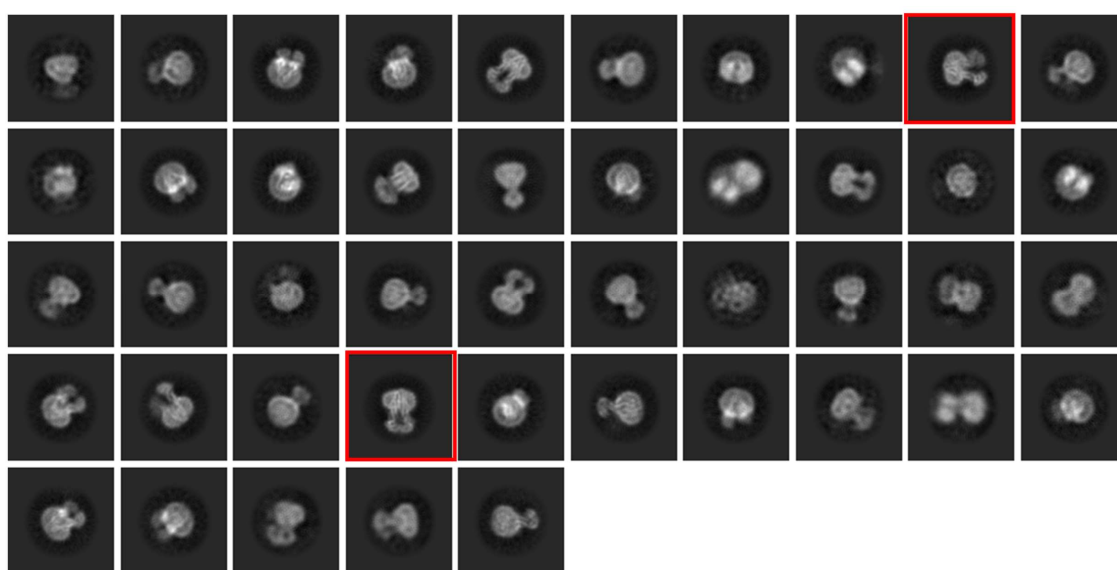


Figure 20: Selected 2D averages of apo MsbA incorporated into Salipro. Averages from the 2D classification show MsbA in different perspectives and opening angles, highlighted in red.

A 3D variability analysis was performed to investigate further the differences in the opening angle in the apo MsbA in Salipro. This CryoSPARC tool allows for the exploration of discrete and continuous heterogeneity in single-particle cryo-EM data sets¹⁵⁵. In this analysis, particle images were not reconstructed into a single 3D structure. Instead, they are used to reconstruct a continuous family of 3D structures. This family contains flexible conformations that may exist in the sample. The 3D variability analysis was performed on a subset of 50000 particles after the 2D classification. The result was a family of 3D structures showing different conformations of MsbA in Salipro ranging from the relative wide-open conformation (class 0 in grey) to conformation where the NBDs are almost in contact with each other (class 4 in red) (Figure 21, top row). To convert the 3D cryo-EM maps into an actual MsbA structure, the inward open structure of MsbA (PDB ID: 6bpp¹⁹) was morphed into the maps of the different classes.

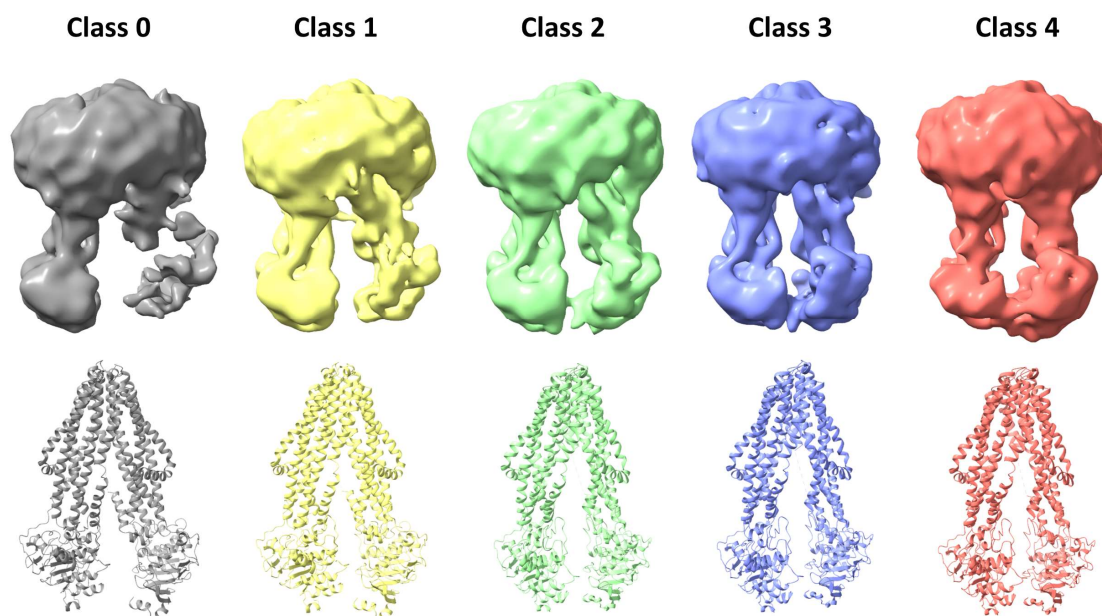


Figure 21: 3D analysis of the flexibility of MsbA in Salipro. The 3D variability analysis confirms different opening angles of MsbA incorporated in Salipro represented in five different classes (class 0 – class 4, upper row), ranging from the relatively wide open in class 0 (grey) to fairly close conformation in class 4 (red). The inward open MsbA structure of PDB: 6bpp¹⁹ was morphed into the cryo-EM maps yielding MsbA models in different opening angles (lower row).

The result of morphing the MsbA structure into the five classes is shown in Figure 21 (bottom row), illustrating five MsbA structures with different distances between the two NBDs. These structures made it possible to determine the distances between amino acids of the different chains which are essential for nucleotide binding, similar to the analysis of the ADP-Vi trapped MsbA (Figure 19). Between the Walker motif (S482) and the signature motif (S378) of the opposing chain, the distance decreases from 26.4 Å of the most open structure of class 0 to

17.4 Å of the most closed structure of class 4. This trend is only not followed by the distance of class 3. With 17.2 Å, it has approximately the same distance as class 4. A similar trend of decreasing distances is also detected between the amino acids Y351 (chain A) and Q485 (chain B). The outlier is the distance of 22.4 of class 1. This study confirms the overall trend of decreasing distances between the two NBDs from class 0 to class 4. The exact lengths must be taken with caution due to the low resolution of the 3D cryo-EM maps used in the morphing (~7.5 Å resolution). This analysis also shows the inward open conformation of MsbA in the apo state. The distances of the ADP-Vi trapped state are 7.9 Å between S378 (chain A) and S482 (chain B) and 16.3 Å between Y351 (chain A) and Q485 (chain B), significantly shorter compared to the apo class 4 with the shortest measured distance.

Table 6: C-alpha distances between S482 (Walker A motif) and S378 (signature motif). Furthermore, the C-alpha distances between Y351 and Q485 from different chains are shown from the five apo MsbA structures and the ADP-Vi trapped MsbA in Salipro (PDB ID: 7bcw)¹³³.

S378 (A) – S482 (B)	Distance of C-alpha (Å)		Y351 (A) – Q485 (B)	Distance of C-alpha (Å)
Class 0	26.4	open  closed	Class 0	26.6
Class 1	21.9		Class 1	22.4
Class 2	18.1		Class 2	24.2
Class 3	17.2		Class 3	23.1
Class 4	17.4		Class 4	22.8
ADP-Vi (PDB: 7bcw)	7.9		ADP-Vi (PDB: 7bcw)	16.3

The five different classes were further refined to improve their resolution. In the first step, a heterogeneous refinement was performed to distribute all particles from the 2D classification to the five 3D reconstitutions from the 3D variability analysis. Next, a non-uniform refinement was performed, followed by a per-particle CTF refinement and a naïve local refinement step to obtain the final 3D reconstruction map. Class 0 (grey) had a final resolution of 6.51 Å, class 1 (yellow) 5.49 Å, class 2 (green) 5.25 Å, class 3 (blue) 5.92 Å and class 4 (red) 6.14 Å. The resolution of the two most extremes (class 0 and class 4) have the worst resolution due to the reduced particle number (108259 particles in class 0, 97914 particles in class 4) in comparison to class 1 (141475 particles), class 2 (173020 particles) and class 3 (161.139 particles). The apo MsbA resolution is much worse than the ADP-Vi trapped MsbA structure (3.5 Å). A possible explanation is that apo MsbA is not only in the 5 different shown conformations present in a lipid environment but in many more sub-states between the shown classes. This heterogeneity of particles in the different classes hinders a high-resolution reconstruction.

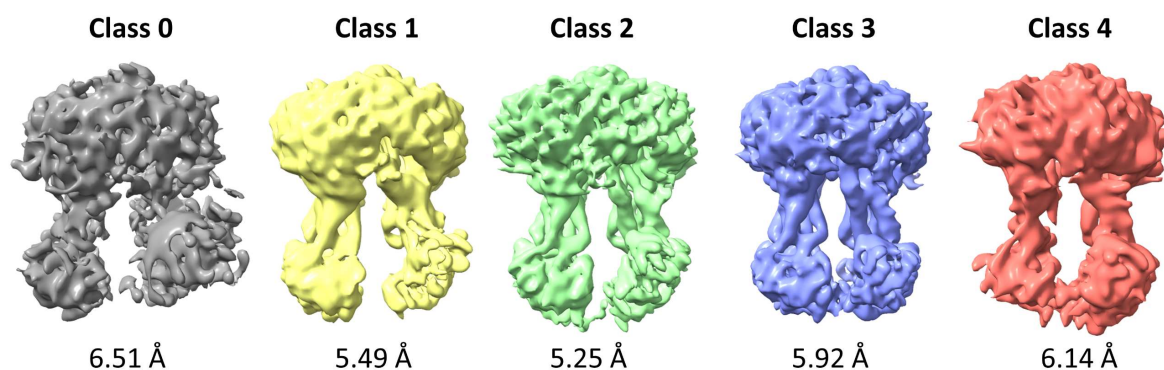


Figure 22: Refined 3D reconstitution of class 0 – class 4. After the 3D variability analysis, multiple refinement steps lead to a resolution of 6.51 Å for class 0 (grey), 5.49 Å for class 1 (yellow), 5.25 Å for class 2 (green), 5.92 Å for class 3 (blue) and 6.14 Å for class 4 (red) (GSFC 0.143).

Figure 23 shows the detailed data processing workflow for apo MsbA in Salipro. First, 11.717 movies were recorded and pre-processed, including motion correction¹¹⁹ and CTF estimation¹³⁹. Next, 706729 particles were picked using crYOLO¹⁴⁰, followed by a 2D classification step ($T = 50$) to remove obvious junk particles. A subset of 50000 particles of the remaining 681807 particles was used for a 3D variability analysis, resulting in a 3D reconstruction family of 5 classes (class 0 – class 4). All particles after the 2D classification were distributed in a heterogeneous refinement to the five classes. After several additional refinement steps, the final 3D reconstructions of the five classes were obtained with a resolution between 6.51 Å (class 0, grey) and 5.25 Å (class 2, green) (GSFC 0.143). In addition, the five 3D reconstructions from the 3D variability analysis were used to morph the inward open MsbA structure (PDB ID: 6bpp¹⁹) into different classes.

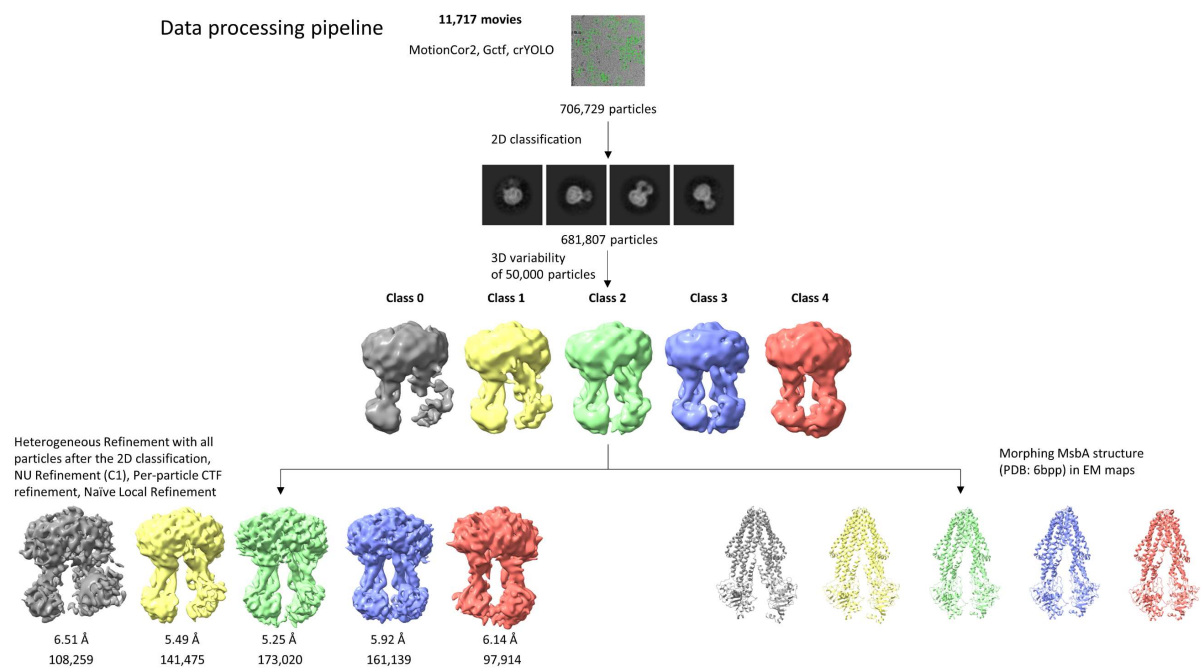
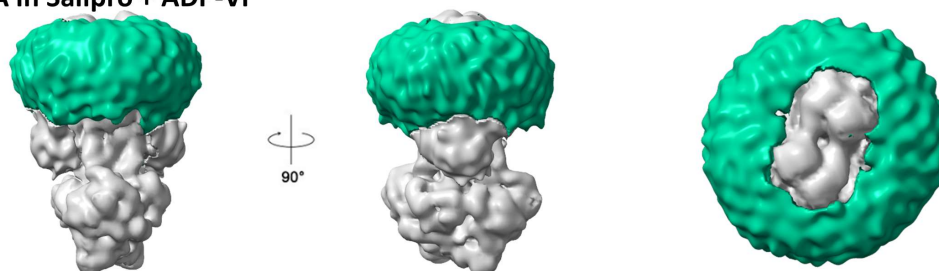


Figure 23: Image processing workflow of apo MsbA in Salipro. Starting with 11717 movies, the pre-processing, including motion correction and CTF estimation was done, followed by particle picking with crYOLO resulting in 706729 picked particles. Next, obvious junk particles were removed in a 2D classification step ($T = 50$). The 2D classes show MsbA in different opening angles in the Salipro. Next, a 3D variability analysis with a subset of 50000 particles was performed to confirm the flexibility of apo MsbA in Salipro. Finally, a heterogeneous refinement with all particles after the 2D classification of the five classes (class 0 – class 4) was performed, followed by several refinement steps in C1. In addition, the MsbA structure (PDB ID: 6bpp) was morphed into different classes.

A remarkable feature observed in the cryo-EM maps concerns the arrangement of the Salipro disc around MsbA. The Salipro with MsbA in the ADP-Vi trapped state shows a round, symmetrical shape (Figure 24, green). In contrast, the shape of the Salipro discs with apo MsbA is more oval (Figure 24, yellow). The two features on the side of MsbA trapped with ADP-Vi are the His₆-tag of MsbA. All refinement steps of the ADP-Vi trapped MsbA were performed in a C2 symmetry which is why two His₆-tags are reconstructed in the cryo-EM density maps. In the apo sample, no His₆-tag is visible because of the refinements in the C1 symmetry. The refinement software did not align all particles correctly, so the His₆-tags were not on the same site of the particles leading to the vanish of the tag's density during the refinements. Another possible explanation could be that the His₆-tag is less ordered in the apo state leading to missing density in the refinement. The protein's conformation potentially influences the shape of the Salipro, even though the TMDs of MsbA in both conformations are very similar. The influence of the protein on the shape of lipid carrier discs and detergent was also described for other membrane protein classes like lipid scramblases¹⁵⁶. In this case, the protein induces a distortion of MSP-based nanodisc lipids and detergents in the TMD. Neither are uniformly distributed on

the outside of the protein. Instead, they adapt to the shape of the protein, resulting in a slightly V-shaped plane of the lipid bilayer or the detergent.

MsbA in Salipro + ADP-Vi



MsbA in Salipro (apo)

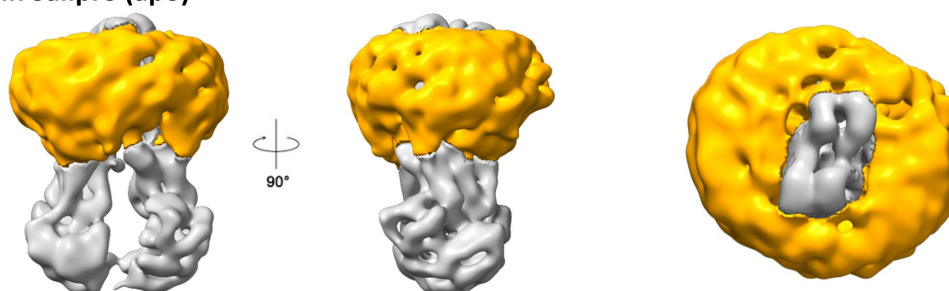


Figure 24: Comparison of the Salipro disc with MsbA in the apo and the ADP-Vi trapped state in cryo-EM density maps low-pass filtered to 6 Å. The Salipro discs with MsbA with ADP-Vi (green) have a round and symmetrical shape, while the discs with apo MsbA are elliptical (yellow). MsbA is shown in grey.

This cryo-EM study illustrates the great flexibility of apo MsbA with numerous different opening angles in Salipro discs. Due to this heterogeneity, refining a high-resolution density map is very challenging. To improve the resolution, more data should be collected to be able to distribute more particles into more classes with different opening angles. With a decent number of particles in the classes, the resolution of each class should be improved. In addition, a potential influence of the MsbA conformation on the shape of the Salipro could be shown.

A potential outlook to further analyse MsbA in Salipro with cryo-EM is a time-resolved study observing the nucleotide binding and the transition from the occluded to the outward open state. In this experiment, MsbA incorporated into Salipro is mixed with an ATP solution and sprayed in different time intervals onto grids to freeze MsbA in different conformational states in the reaction cycle. With this mixing and spraying device, it is possible to study protein motions in the microsecond to millisecond timeframe¹⁵⁷. This experiment could potentially visualise different conformations of MsbA in a lipid environment at a near-atomic resolution.

3.2 Chapter 2 – Structural analysis of MsbA by small-angle neutron scattering (SANS) using stealth Salipro nanoparticles

3.2.1 Expression of matched-out deuterated Saposin A in deuterated minimal media

The expression of deuterated material is essential for match-out studies of a multi-component complex with neutrons. In this thesis, Saposin A (SapA) and phosphocholine (PC) lipids are deuterated to achieve a neutron-invisible lipid carrier, which does not contribute to the neutron scattering signal. The production of match-out deuterated PC lipids with 78% deuteration in the headgroup and 92% in the acyl chains are well described⁸¹. The expression protocol of dSapA with a deuteration level of 70% of the non-exchangeable hydrogen atoms was unknown. The hydrogenated SapA was expressed in the *E. coli* strain Rosetta-gami 2. However, the adaptation of Rosetta-gami 2 cells to deuterated minimal media was unsuccessful due to the leucine auxotrophy (the study performed by members of the Tidow lab and confirmed by members of the ILL Life Science group). The alternative was mixing 75% “2H High Performance OD2 Media solution for *E. coli*” with 25% “unlabelled High Performance OD2 Media solution for *E. coli*” to obtain a yield of 3 mg/L of purified matched-out deuterated SapA. The required labelled rich-media to express sufficient amounts of dSapA for a SANS experiment cost over 3000 €. So, the aim was to find an *E. coli* strain that can express dSapA in deuterated minimal media to reduce the cost of the dSapA expression. The Rosetta-gami 2 strain combines the advantages of Rosetta 2 and Origami 2, which supplies seven rare tRNAs and enhances disulfide bonding. The SHuffle T7 Express cells do not provide rare tRNAs but promote disulfide bond formation and are adaptable to deuterated conditions. These cells were used by the D-Lab platform of the ILL to produce other labelled proteins. So, we tried to apply the SHuffle cells to our target protein in hydrogenated conditions to compare the expression rate in both strains.

3.2.1.1 Expression and purification of SapA in SHuffle cells

In the first step, the SapA plasmid was transformed into SHuffle T7 express cells and grown in LB media with kanamycin (1:1000) at 37 °C until an OD600 of ~1 was reached. After cooling down to 20 °C, the expression was induced by adding 0.1 mM IPTG. After the subsequent purification, the SEC profile was compared between SHuffle cells and Rosetta-gami 2 to specify the overall yield of SapA and the distribution between monomeric and multimeric proteins. The SDS-PAGE of the purification of SHuffle cells is shown in Figure 25A. In the first IMAC, SapA with the His-tag and some minor impurities was eluted with a high-

concentrated imidazole buffer, followed by TEV digestion combined with dialysis overnight. In the IMAC after TEV, purified SapA is in the flow-through and the washing fractions. For the Salipro assembly, only monomeric SapA can be used to form disc-shaped lipid carriers. In both SEC profiles, a prominent peak at 89 mL corresponding to the monomeric SapA is present. In SHuffle cells, more multimeric SapA is present, visualized in the peak at 78 mL (Figure 25B). However, the yield of monomeric SapA from SHuffle cells is comparable to Rosetta-gami 2, showing the successful expression of SapA in another *E. coli* strain.

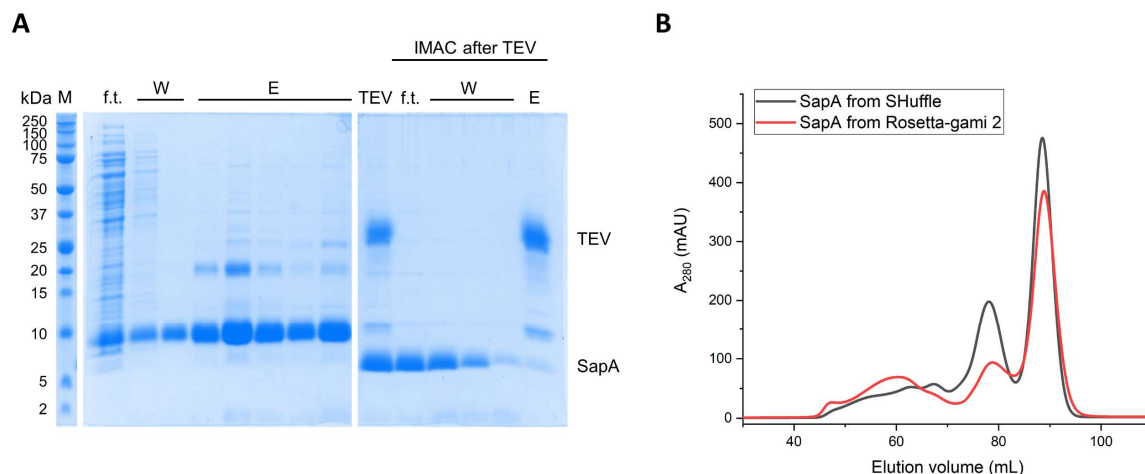


Figure 25: Purification of SapA from SHuffle cells grown in LB media. **A:** SDS-PAGE of SapA purification showing the successful purification of SapA without the His-tag. M = molecular weight marker, f.t. = flow through of lysate through Ni-beads, W = wash fractions, E = elution fractions, TEV = after TEV digest. **B:** SEC profile of SapA from SHuffle cells (in LB media) compared to Rosetta-gami 2 (in TB media) after the second IMAC. The yield of monomeric SapA (peak at 89 mL) from SHuffle cells is comparable to Rosetta-gami 2.

3.2.1.2 Small scale expression and purification of matched out deuterated Saposin A (dSapA) in deuterated conditions

The next step was to adapt the transformed SHuffle cells from LB media to hydrogenated Enfors minimal medium (H-Enfors) followed by deuterated Enfors (D-Enfors) with hydrogenated glycerol as a carbon source. This deuterated medium allows the expression of proteins which are matched out in 100% D₂O due to the same scattering length density (SLD) like the solvent⁷⁸. This adaptation was performed by adding 1 mL of high-density grown cells to 9 mL of fresh hydrogenated minimal Enfors media and incubating at 37 °C overnight. This was repeated over three days. Then, the cells were adapted to 85% deuterated Enfors media over seven days with the same adaptation protocol. This was followed by a small-scale expression in a flask to analyse the expression rate. At an OD₆₀₀ of 0.8, the incubation temperature was decreased to 20 °C, followed by induction with 0.1 mM IPTG overnight. After the successful two-step IMAC, the SEC profile of dSapA grown in D-Enfors (Figure 26) looked

similar to the profile of SapA grown in LB (Figure 25), confirming no decrease in the expression rate in deuterated minimal media.

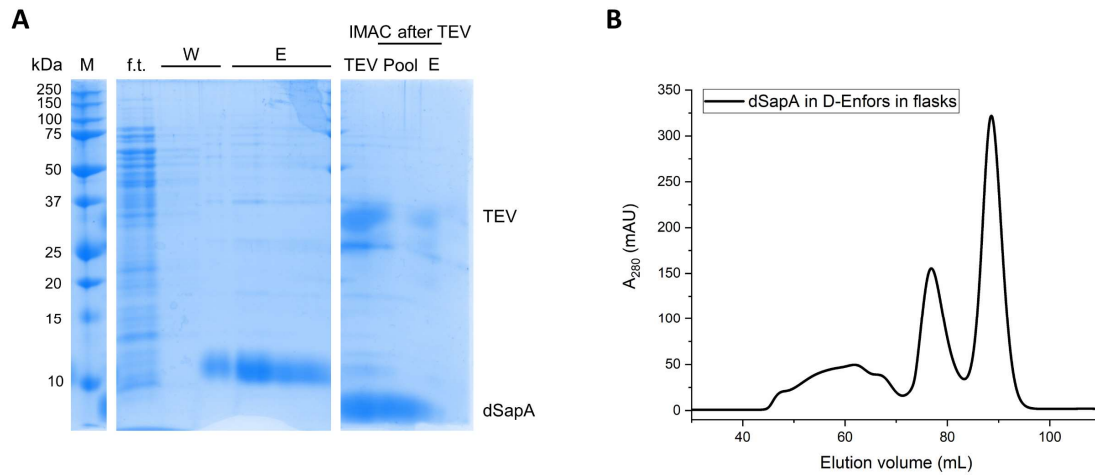


Figure 26: Purifying dSapA from SHuffle cells grown in a flask in D-Enfors minimal media. **A:** SDS-PAGE of dSapA purification showing the successful purification of SapA without the His-tag. M = molecular weight marker, f.t. = flow through of lysate through Ni-beads, W = wash fractions, E = elution fractions, TEV = after TEV digest, Pool = pool of flow through after TEV digest and wash fractions. **B:** SEC profile of dSapA from SHuffle cells in D-Enfors after the second IMAC showing the monomeric dSapA (peak at 89 mL).

3.2.1.3 Expression and purification of dSapA in a high cell density culture (HCDC)

Expressing proteins in a fermenter using high cell density cultures (HCDC)¹⁵⁸ instead of in flasks has the advantage of precisely controlling the bacteria growth conditions such as temperature, pH, oxygen level, etc. Furthermore, with the constant addition of feeding solution (hydrogenated glycerol, 120 g/L), it is possible to grow to much higher OD which often leads to more expressed protein in relatively low amounts of D₂O. A 150 mL inoculum of SHuffle cells in D-Enfors with kanamycin (1:1000) was prepared and incubated at 37 °C overnight for the fermenter the next day. The preculture was added to 1.2 L D-Enfors media with kanamycin (1:1000) dissolved in D₂O in the fermenter and incubated at 30 °C for 2 days until an OD₆₀₀ of 18.6 was reached. Then, the temperature was decreased to 20 °C and the induction was initiated by adding 0.5 mM IPTG. After another 20 h, the fermenter was stopped with a final OD of 22, yielding 45.2 g of cell paste. Before and after induction, a small portion of cells was taken to perform an expression test. The expression test shows overexpression of dSapA after IPTG induction (Figure 27B). The SDS-PAGE confirms the overexpression of dSapA. After IPTG induction (AI) is a band corresponding to dSapA visible, while this band is missing before the induction (BI).

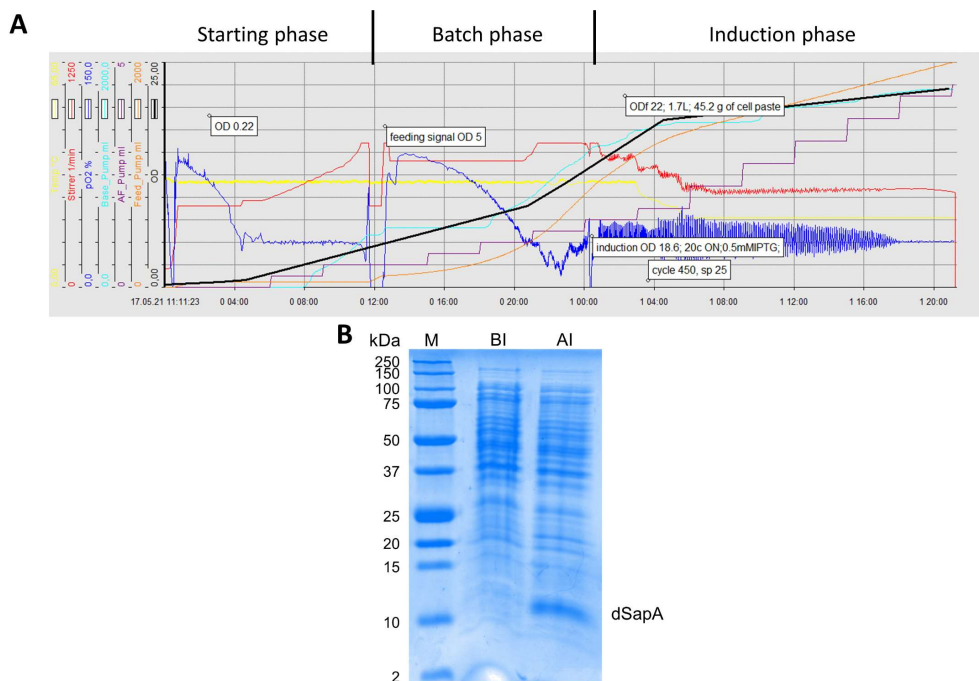


Figure 27: Expression of dSapA in deuterated HCDC. **A:** Profiles of fermentation during the expression of dSapA in a fermenter. The temperature is shown in yellow, the stirring speed in red, the oxygen level in blue, the amount of added base in turquoise, the amount of added anti-foam in purple, the amount of added feeding solution in orange and the OD in black. In the starting phase of the fermentation, 5 g/L of hydrogenated glycerol is present in the medium. After the consumption of the carbon source, new glycerol from the feeding solution is added to the culture. In this batch phase of the fermentation, the bacterial growth is exponential. In the induction phase, IPTG was added to the culture, the temperature was decreased to 20 °C and the biomass was harvested after 20 hours of incubation. **B:** SDS-PAGE of dSapA test expression in a HCDC. Cells were induced with 0.1 mM IPTG overnight, yielding an overexpression of dSapA. M = molecular weight marker, BI = before IPTG induction, AI = after IPTG induction.

The following purification was performed to obtain large amounts of purified, monomeric match-out deuterated SapA (Figure 28). After the two-step IMAC, the profile of the SEC shows a prominent peak at 89 mL, confirming the successful purification of dSapA from SHuffle cells grown in “the cheaper” D-Enfors minimal media. This dSapA was used to prepare stealth Salipro in SANS experiments.

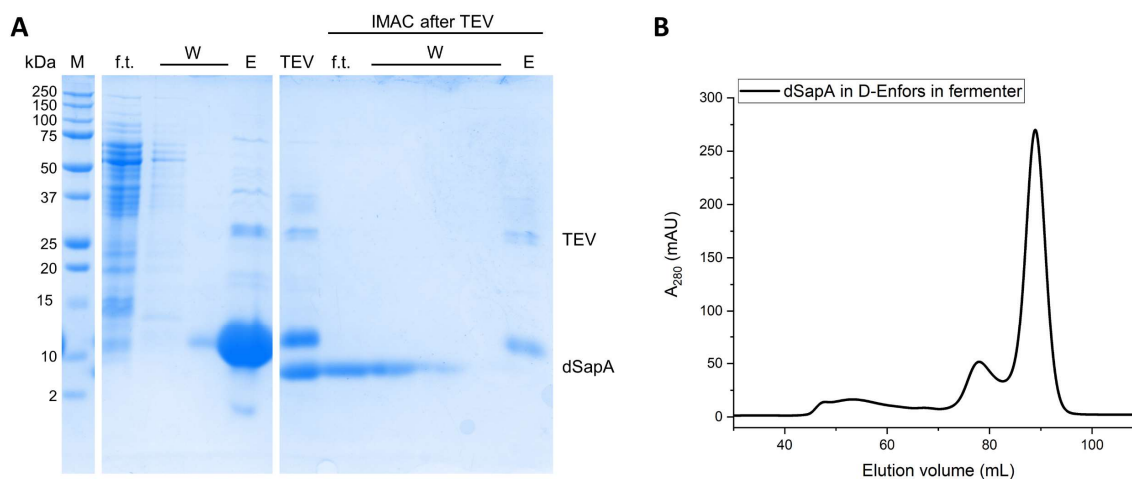


Figure 28: Purification of dSapA from SHuffle cells grown in the fermenter in D-Enfors minimal media. **A:** SDS-PAGE of dSapA purification showing the successful purification of SapA without the His-tag. M = molecular weight marker, f.t. = flow through of lysate through Ni-beads, W = wash fractions, E = elution fractions, TEV = after TEV digest. **B:** SEC profile of dSapA from SHuffle cells in D-Enfors after the second IMAC showing the monomeric dSapA (peak at 89 mL).

3.2.2 Contrast variation experiments of MsbA in Salipro nanoparticles

Partial deuteration of particular components in a multi-component complex enables matching out specific components measuring small-angle neutron scattering in different backgrounds due to the matching scattering length density of component and background. To prove this concept, MsbA was reconstituted in Salipro containing hydrogenated Saposin A (hSapA) and hydrogenated POPC as well as 70% deuterated Saposin A (dSapA) with hydrogenated POPC. These two samples were measured in 100% H₂O, 8% D₂O, 42% D₂O and 100% D₂O to match-out different components in the protein/protein/lipid complex.

MsbA was overexpressed in the *E. coli* strain C43 to sufficient amounts and purified in Dodecyl- β -D-maltoside (DDM). For this, the cells were lysed, followed by a first centrifugation step where the cell debris was removed and in a second centrifugation, the membrane fractions were isolated. The membrane proteins were solubilised in DDM and purified by immobilised metal affinity chromatography (IMAC). In Figure 29, the SDS-PAGE gel of the IMAC is shown. In the first washing step with 1% (w/v) DDM, impurities from the flow-through (f.t.) were separated from the Ni-resin. In addition, most of the endogenous lipids around MsbA were removed. This washing step is essential to minimise scattering signal contributing from non-labelled lipids. In the second and third washing step, the Ni-resin is washed with an increasing concentration of imidazole to remove more impurities. The bound MsbA is starting to elute from the column in the third washing step due to the higher imidazole concentration (see MsbA band in W3). Finally, MsbA was eluted with a high imidazole

concentrated buffer. The first elution fraction shows a few impurities co-eluting with MsbA. After the assembly, these impurities will be separated from MsbA in the size exclusion chromatography (SEC). The remaining elution fractions contain only purified MsbA. All MsbA elution fractions were pooled and used for the reconstitution in Salipro.

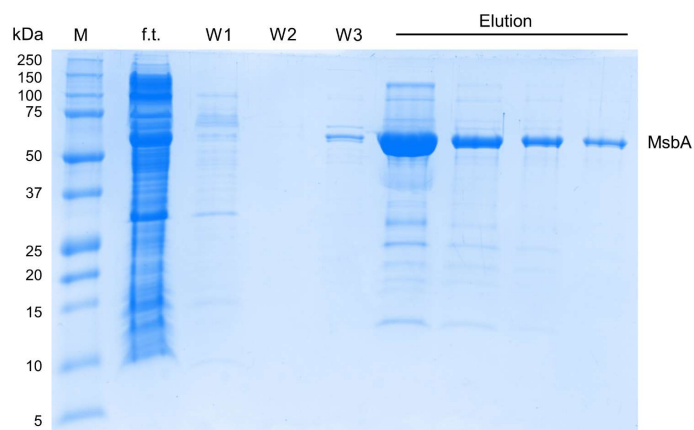


Figure 29: SDS-PAGE gel of the MsbA purification. After three washing steps (first: high DDM concentration, second and third increasing imidazole concentration), purified MsbA and minor impurities are eluted from the Ni-beads.

For the contrast variation experiment, MsbA incorporated in Salipro with hydrogenated SapA and POPC and in Salipro with match-out deuterated SapA and hydrogenated POPC was prepared. To reconstitute MsbA into Salipro, a molar ratio of 1:4:20 (MsbA:hSapA/dSapA:POPC) was used. In the following SEC, the successfully assembled MsbA were isolated. In Figure 30A the SEC profiles of MsbA:hSapA:POPC and MsbA:dSapA:POPC are shown. Both profiles show a similar progression with a small amount of large aggregates in the void volume of the column at ~8 mL and larger particles at ~11 mL. MsbA incorporated into Salipro is eluting at 13 mL and possibly empty Salipro at 16 mL. The successful reconstitution of MsbA into the two different Salipros could be confirmed by SDS-PAGE (Figure 30B). In both samples, a band for MsbA and hSapA/dSapA is visible.

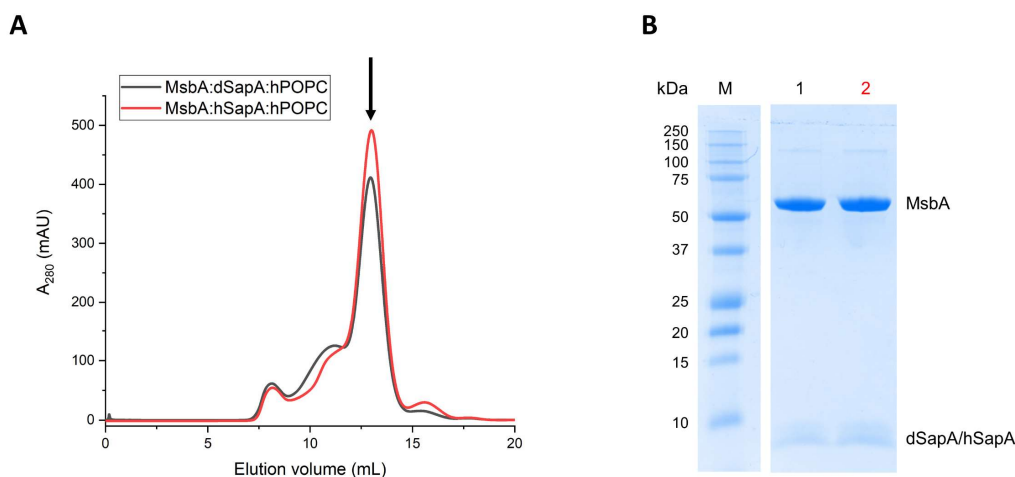


Figure 30: Reconstitution of MsbA into Salipro containing deuterated SapA with hydrogenated POPC (black) and Salipro containing hydrogenated SapA and POPC (red). **A:** SEC profiles show the successful assembly of MsbA in Salipro at 13 mL elution volume. **B:** SDS-PAGE gel of SEC fractions at 13 mL showing the presents of MsbA and dSapA/hSapA. M = molecular weight marker, 1 = MsbA in Salipro with a deuterated SapA and hydrogenated POPC, 2 = MsbA in Salipro with hydrogenated SapA and POPC.

3.2.2.1 Contrast variation experiment of MsbA:hSapA:POPC

In the following experiment, MsbA was incorporated in a Salipro containing hydrogenated Saposin A (hSapA) and hydrogenated POPC. The aim was to match-out different components using different H_2O/D_2O ratios in the solvent. The scattering length density (SLD) increases linearly with higher fractions of D_2O in the solvent. This linear function of the solvent crosses the SLD functions of hydrogenated lipids at 8%, hydrogenated proteins at 42% and match-out labelled proteins and lipids at 100% D_2O (Figure 31A). Under these solvent conditions, the SLD of the component and solvent are matching, the contrast is zero and the component is not contributing to the neutron scattering data. We built a model of MsbA:hSapA:POPC and MsbA:dSapA:POPC (Figure 31B), calculated the scattering curve in different H_2O/D_2O ratios and compared these to experimental data. The models were built in MPBuilder¹⁵⁹ and the deuteration was implemented using a python script.

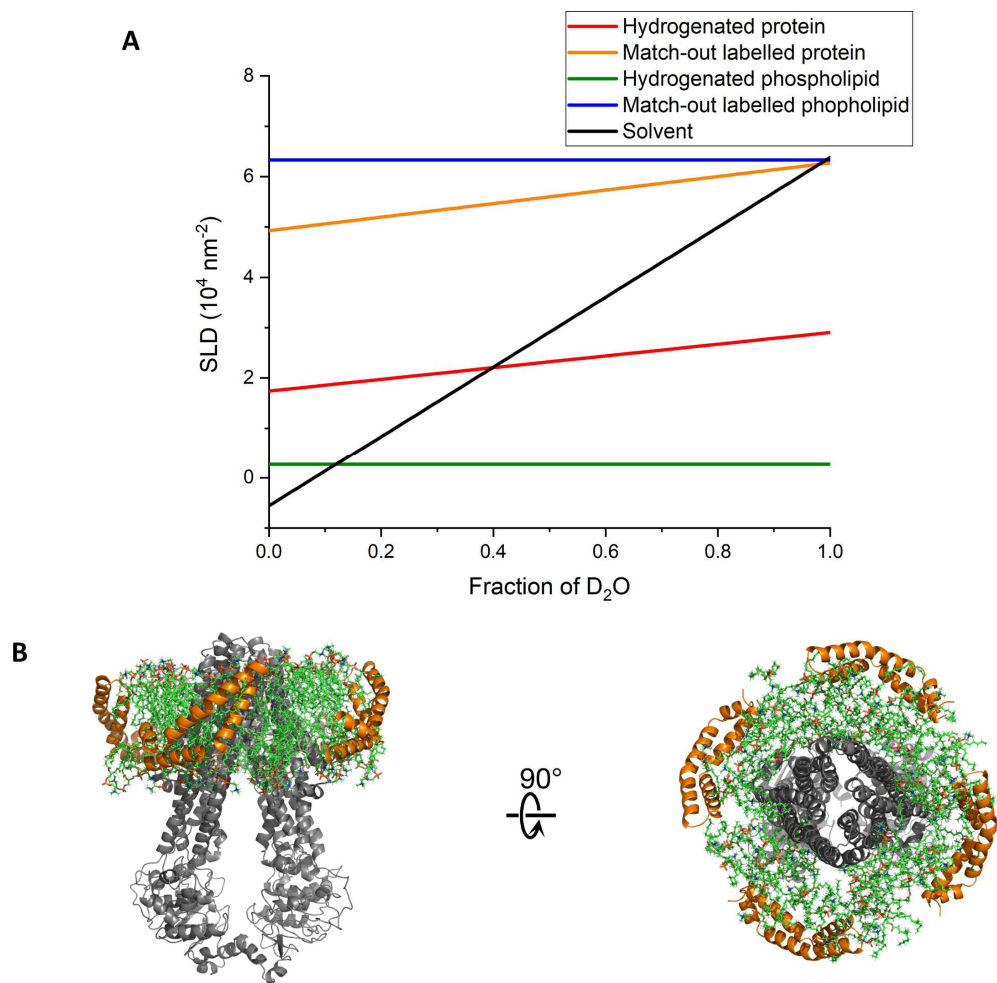


Figure 31: **A:** The scattering length densities (SLDs) of the major biomolecules used in this work are plotted as a function of the volume percentage of D₂O, assuming all labile hydrogens are exchanged. The match points of each biomolecule correspond to the intersection with the solvent function. **B:** Model of MsbA (grey) incorporated into Salipro created with MPBuilder¹⁵⁹ from the side and top view. The Salipro is built of four SapA proteins (orange) and a bilayer of POPC lipids (sticks in green). This model was used to predict theoretical scattering curves in different backgrounds with varying D₂O levels.

In this section of the contrast variation SANS experiment MsbA:hSapA:POPC was analysed in different H₂O/D₂O ratios. Various components contribute to the neutron scattering signal with different amounts based on the solvent. These contributions can be zero when the SLD of the component and solvent is identical (contrast = 0), small with a slight difference in SLD or large with a significant difference in SLD. Additionally, combining scattering components (global SLD) can lead to a match out of the complex in a certain H₂O/D₂O ratio. In Figure 32, the theoretical component contribution to the neutron scattering is illustrated. The transparency level indicates the contribution to the neutron scattering. In H₂O, the hydrogenated proteins MsbA and hSapA should scatter dominantly, while the hydrogenated lipids are almost invisible (Figure 32A). At 8% D₂O, the matching point of POPC is reached, so the lipid bilayer is invisible, while MsbA and hSapA scatter equally (B). The matching point of MsbA and hSapA is reached at 42% D₂O in the solvent (C) and only the lipid bilayer of POPC contributes to the

scattering. In 100% D₂O, the SLD difference between the solvent and MsbA/hSapA is smaller compared to solvent vs. POPC, so the scattering contribution of the protein is less than from the lipids (D).

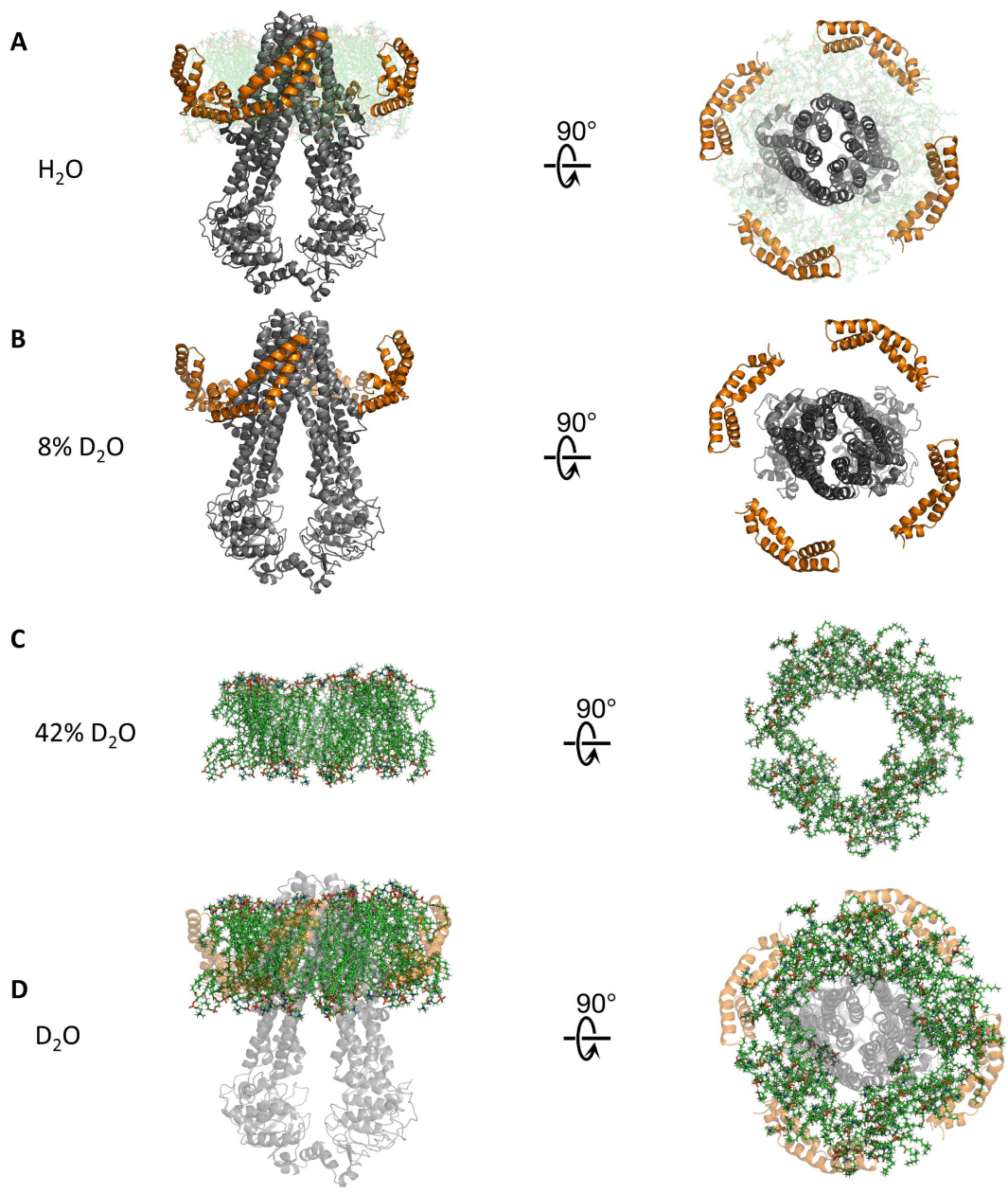


Figure 32: Model of MsbA (grey) in a full hydrogenated Salipro (SapA in orange, POPC in green sticks) with different components matched out due to different H₂O/D₂O ratios of the solvent. The transparency level indicates the neutron scattering contribution in combination with the solvent. **A:** In H₂O, the lipids are barely scattering due to the small contrast in the solvent. **B:** In 8% D₂O, hydrogenated Phospholipids are matched out, leaving the MsbA and the SapA proteins visible in neutrons. **C:** In 42% D₂O, hydrogenated proteins have the same SLD as the solvent and only the bilayer of POPC with a hole scatters neutrons. **D:** In 100% D₂O, the neutron scattering is dominated by lipids.

The neutron scattering of MsbA in a hydrogenated Salipro (hSapA + POPC) was measured in H₂O, D₂O 8% D₂O and 42% D₂O. The scattering profiles are shown in Figure 33A. Every measured sample has a plateau in the low q-range, indicating a high sample quality without

aggregations. The sample measured in H₂O has a flat high q-range and with an increasing D₂O ratio, this region becomes steeper. In Figure 33B is the Guinier region shown, which was used to determine the radius of gyration (R_g).

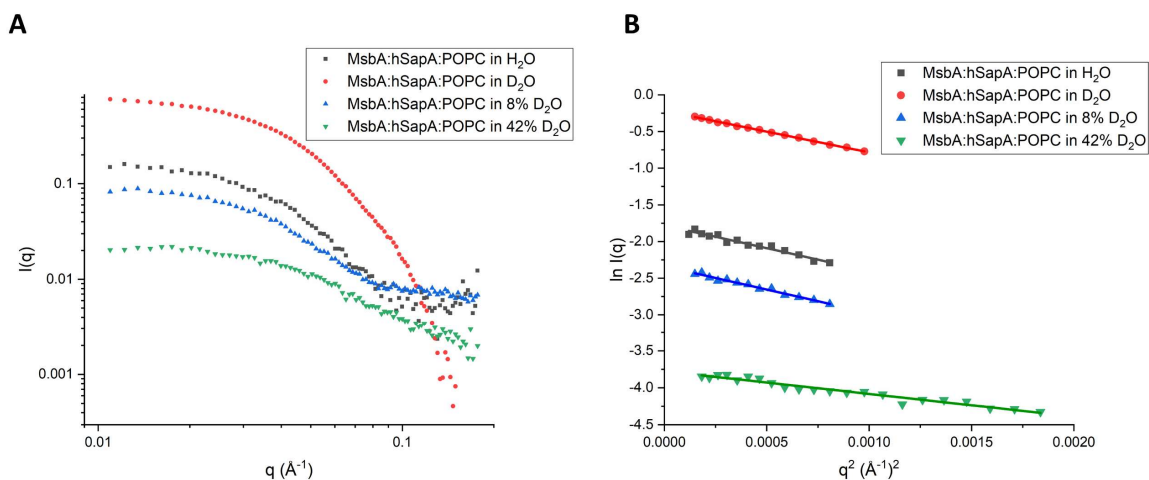


Figure 33: Small-angle neutron scattering of MsbA incorporated into hydrogenated Salipro in different backgrounds with varying H₂O/D₂O ratios, H₂O (black), D₂O (red), 8% D₂O (blue) and 42% D₂O (green). **A:** Scattering profiles of MsbA in Salipro in different backgrounds. **B:** Guinier region of the SANS data.

The distance distribution plots show significant differences (Figure 34A). While the measurements in 8% and 42% D₂O show a double peak, the measurements in H₂O and D₂O show only one peak. The double peak at 8% D₂O is due to the match-out of POPC lipids, resulting in a hollow space between the hSapA and MsbA. In 42% D₂O MsbA and hSapA is neutron invisible, leaving only a bilayer of lipids with a hole in the middle. In 100% H₂O and 100% D₂O, respectively larger holes or hollow areas are not present in the particle, yielding only one peak in the distance distribution plot. Only with the POPC scattering, the D_{\max} of the measurement in 42% D₂O is with 84 Å significantly smaller compared to the measurements at H₂O (128 Å) and 8% D₂O (125 Å). The Kratky plots illustrate the compactness of the particles. In H₂O, 8% D₂O and 42% D₂O, the particles are less compact due to the matched out components in the middle of the particle.

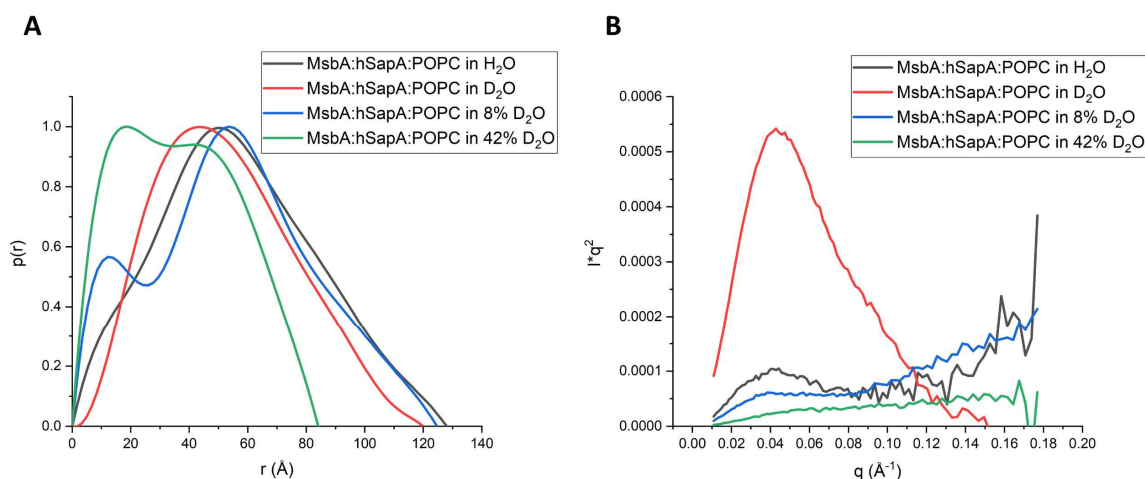


Figure 34: Analysis of SANS data of MsbA in hydrogenated Salipro in different backgrounds with varying H₂O/D₂O ratios, H₂O (black), D₂O (red), 8% D₂O (blue) and 42% D₂O (green). **A:** Distance distribution plots of MsbA in different backgrounds showing differences in D_{\max} . Hollow spaces in the particles are illustrated in the double-peaks in 8% and 42% D₂O. **B:** Kratky plot of the data of A. The peak size indicated different levels of compactness of the particles in different solvents.

Table 7 contains structural SANS parameters for the measurements of the four tested conditions. All parameters fit to the expected match-out condition. For example, the R_g , D_{\max} , V_P and the $I(0)$ at 42% D₂O are the smallest due to the match-out of MsbA and hSapA. Also, the highest Porod volume was measured in H₂O. Both proteins scatter dominantly in this condition, and the lipids scatter less. In contrast, in D₂O, only the lipids scatter dominantly and both proteins scatter only with a reduced contribution leading to a small V_P .

Table 7: Structural SANS parameters of MsbA incorporated into hydrogenated Salipro in different backgrounds with varying H₂O/D₂O ratios.

MsbA:hSapA:POPC	R_g (Å)	D_{\max} (Å)	V_P (nm ³)	$I(0)$ (cm ⁻¹)
in H ₂ O	43.6 ± 1.32	128	357	0.17 ± 0.0031
in D ₂ O	41.2 ± 0.19	120	284	0.80 ± 0.0024
in 8% D ₂ O	43.7 ± 0.90	125	270	0.097 ± 0.0012
in 42% D ₂ O	30.3 ± 0.76	84	33	0.023 ± 0.00036

The model of MsbA:hSapA:POPC was built with MPBuilder¹⁵⁹ (Figure 31B) and the theoretical neutron scattering in a background of H₂O, 8% D₂O, 42% D₂O and 100% D₂O was calculated with PEPSI¹³⁴. These calculated scattering plots were fitted to the experimental data to confirm the successful match-out of different components in the complex. In Figure 35 the calculated scattering plot compared to the experimental data in H₂O (A), 8% D₂O (B), 42% D₂O (C) and 100% D₂O (D) are shown. The calculations of H₂O, 8% D₂O and 42% D₂O are fitting the experimental data with χ^2 of 0.49 in H₂O, χ^2 of 0.43 in 8% D₂O and χ^2 of 0.62 in

42% D₂O. Only the measurement in 100% D₂O resulted in the worst fit to the experimental data ($\chi^2 = 52.47$). A possible explanation could be the difficult calculation of hydrogenated lipids in 100% D₂O. The non-exchangeable hydrogens in the headgroups are directly exposed to the D₂O solvent, resulting in a missing hydration shell around the headgroups, which is challenging for PEPSI¹³⁴ to calculate.

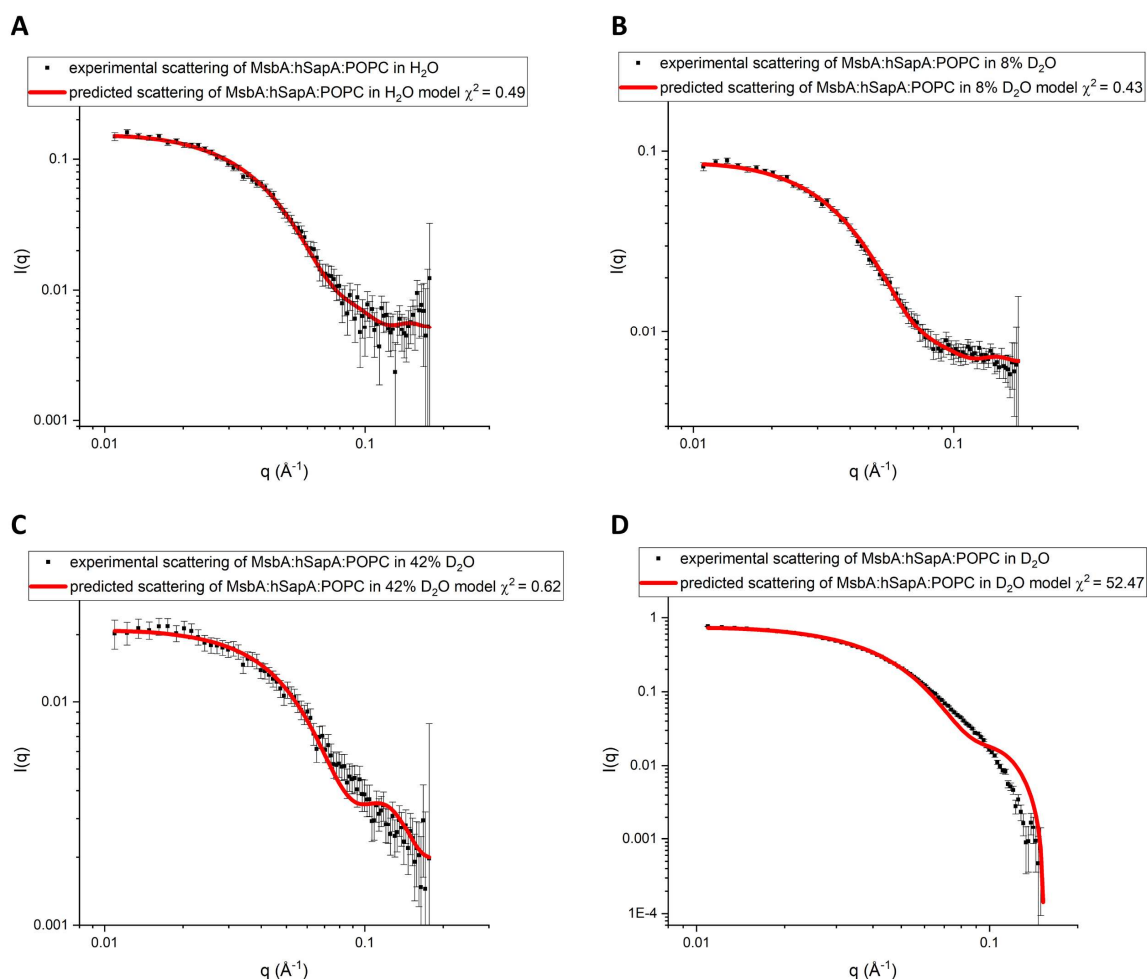


Figure 35: Comparison of the predicted scattering curve using PEPSI¹³⁴ from the model created in MPBuilder¹⁵⁹ to the experimental data of MsbA in hydrogenated Salipro in different backgrounds with varying H₂O/D₂O ratios. **A:** Comparison in H₂O. **B:** Comparison in 8% D₂O. **C:** Comparison in 42% D₂O. The experimental data in H₂O (A), 8% D₂O (B) and 42% D₂O (C) matches the predicted scattering curve from the model. **D:** Comparison in 100% D₂O. The experimental data differs from the predicted data from the model resulting in a high χ^2 of 52.47.

3.2.2.2 Contrast variation experiment of MsbA:dSapA:POPC

Hydrogenated MsbA was also incorporated into a Salipro containing match-out deuterated Saposin A (dSapA) and hydrogenated POPC. Measured in H₂O (Figure 36A), dSapA has the highest contrast to the solvent, so it scatters dominantly. The second most scattering contribution has MsbA while POPC has the lowest contribution due to their SLD differences to the SLD of the solvent. In measurements in 8% D₂O (B), the matching point of lipids is

reached. The dSapA contributes more dominantly to the neutron scattering than the MsbA. In 42% D₂O (C), all hydrogenated proteins are matched out so that MsbA become neutron invisible. The scattering contribution of dSapA and POPC is approximately equal, where the SLD of dSapA is higher than the solvent and the SLD of POPC lower. In combination, these two components could match-out each other due to the opposed SLD difference to the solvent. In 100% D₂O (D), the match-out deuterated SapA becomes neutron invisible, while POPC scatters more than MsbA.

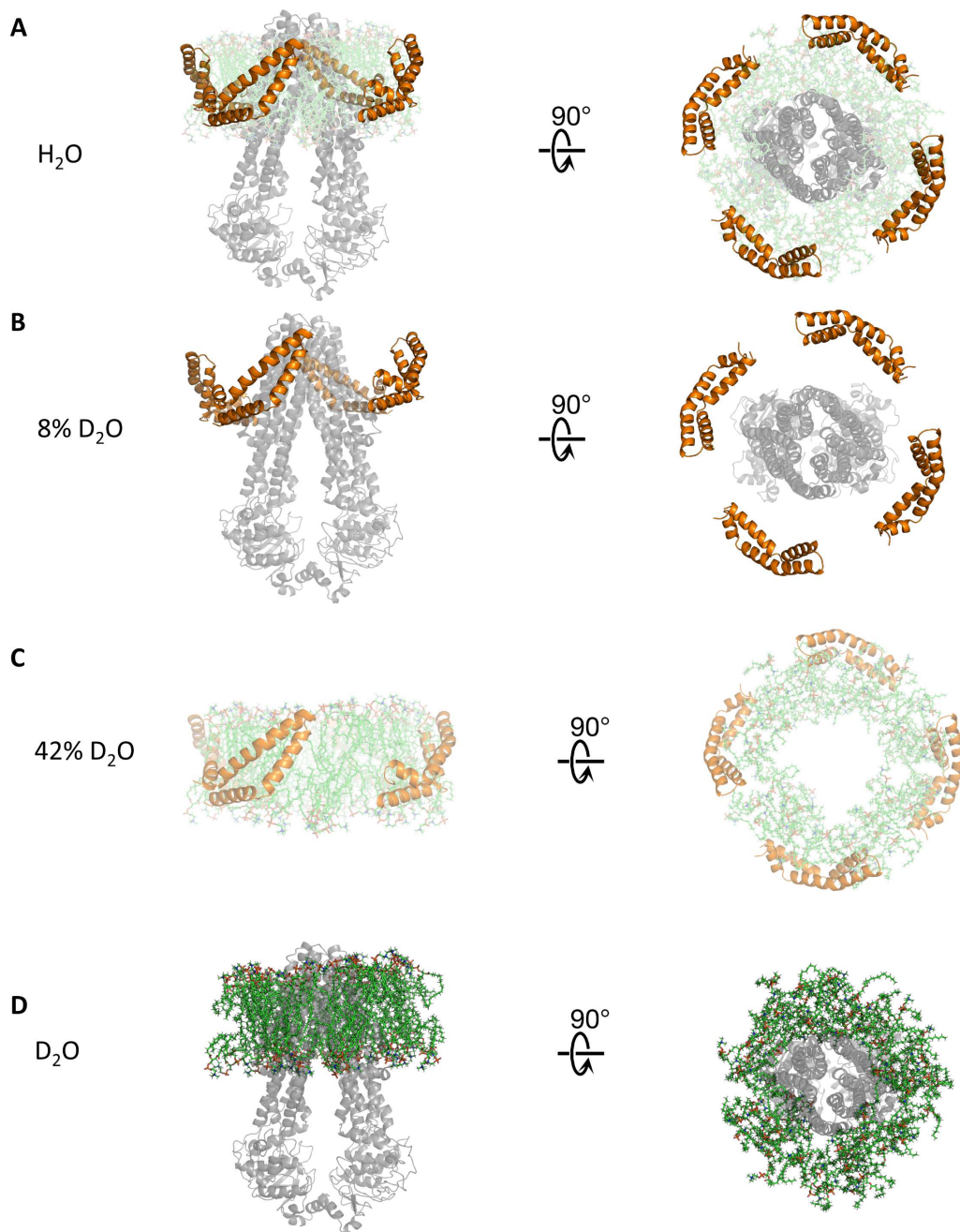


Figure 36: Model of MsbA (grey) in a Salipro of dSapA (orange) and POPC (green sticks) with different components matched out due to different H₂O/D₂O ratios. The transparency level indicates the neutron scattering contribution in combination with the solvent. **A:** In H₂O, dSapA contributes most to the neutron scattering due to the significant difference in the SLD of the deuterated proteins and the solvent. **B:** In 8% D₂O POPC is matched

out while dSapA scatters more than MsbA. **C:** In 42% D₂O, MsbA is matched out and only dSapA and POPC contribute to the neutron scattering. **D:** In 100% D₂O, dSapA is matched out and POPC scatters more than MsbA.

The experimental data of MsbA:dSapA:POPC was collected in H₂O, 8% D₂O, 42% D₂O and 100% D₂O. Figure 37A shows the scattering profile of the measurements in the different backgrounds. The scattering in H₂O (black) and 8% D₂O (blue) are very similar with the same features in the large q-range, while the measurement in 100% D₂O shows fewer features in the large q-range. In 42% D₂O (green), the scattering curve is not showing the typical trend of the scattering of protein samples. Instead, an almost flat curve is obtained with a decreasing small and large q-range. The neutron scattering characteristic of the MsbA:dSapA:POPC particle could explain the flat curve in 42% D₂O. At 42% D₂O, all hydrogenated proteins have the same SLD as the solvent and become neutron invisible so that MsbA is matched out. The remaining is the match-out deuterated Saposin A, which has an SLD above and the POPC with an SLD below the solvent (see Figure 31A). The combination of dSapA and POPC results in a global SLD close to the solvent, so the scattering is minimal. With this minimal scattering with almost no features, the measurement at 42% D₂O was not analysed further for the Guinier region, distance distribution plot and Kratky plot. The Guinier region of the measurements in H₂O, 8% D₂O and 100% D₂O showed a linear progression and was used to determine the R_g.

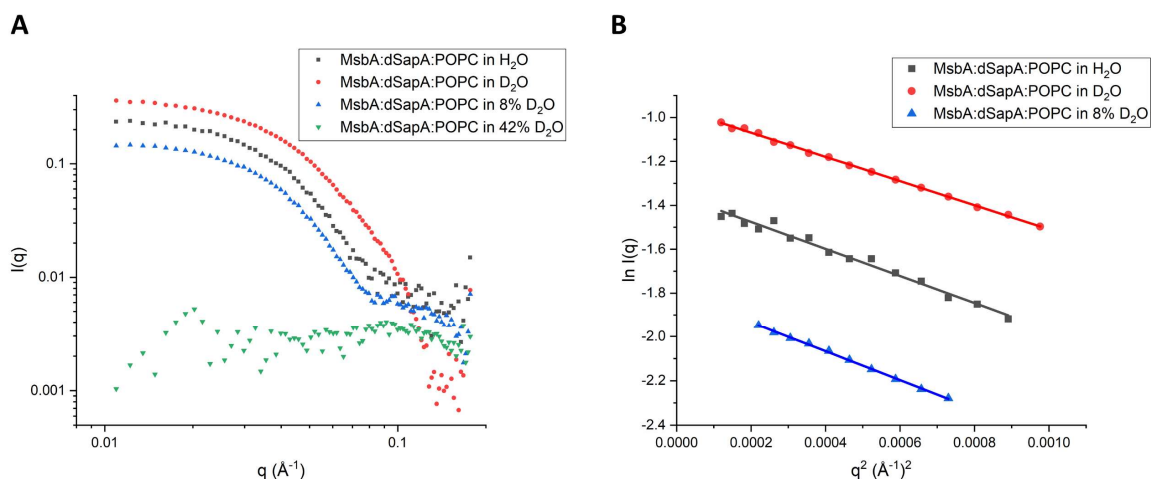


Figure 37: Small-angle neutron scattering of MsbA incorporated into Salipro with match-out deuterated SapA and hydrogenated POPC in different backgrounds with varying H₂O/D₂O ratios, H₂O (black), D₂O (red), 8% D₂O (blue) and 42% D₂O (green). **A:** Scattering profiles of MsbA in Salipro in different backgrounds. **B:** Guinier region of the SANS data. The Guinier region of the measurement in 42% D₂O is not shown due to the low contrast of the combination of dSapA and POPC to the solvent.

The distance distribution plots of the measurements are shown in Figure 38A. The distance of the highest probability in the particles at 100% D₂O is smaller compared to the measurements in H₂O and 8% D₂O. Also, the D_{max} in D₂O is smaller compared to H₂O and 8% D₂O. In D₂O, the match-out deuterated Saposin A is neutron invisible, leaving only MsbA and POPC

scattering. In H₂O and 8% D₂O, dSapA is constantly contributing to the scattering signal. Therefore, the distance with the highest probability and the D_{\max} is larger. The Kratky plots in Figure 38B illustrate the compactness of the particles. The measurement in 100% D₂O (red) has no hollow spaces inside the particle, so it has a high level of compactness. In H₂O, the SLD of POPC is minimally higher than the SLD of the solvent, resulting in a weak scattering component. This weak scatterer inside the particle leads to a less compact scattering structure and the peak is not as large as the peak in D₂O. At 8% D₂O, the lipids are completely matched-out and the hollow space in the particle leads to an even lower level of compactness.

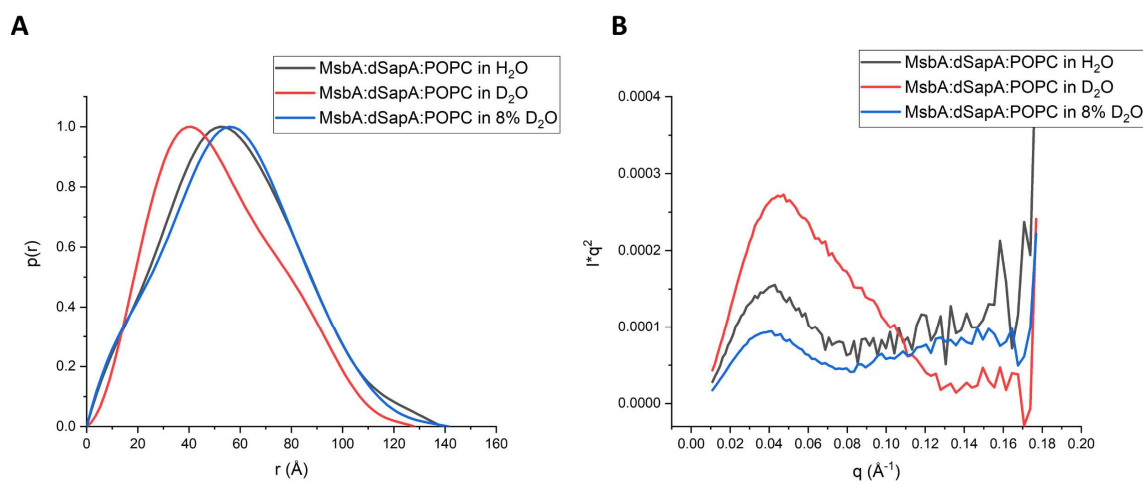


Figure 38: Analysis of SANS data of MsbA in matched out deuterated dSapA and hydrogenated POPC in different backgrounds with varying H₂O/D₂O ratios, H₂O (black), 100% D₂O (red), 8% D₂O (blue) and 42% D₂O (green). **A:** Distance distribution plots MsbA in different backgrounds showing similar D_{\max} value for the sample in H₂O and 8% D₂O. **B:** Kratky plot of the data of A. The peak size indicated different levels of compactness of the particles in different solvents. The measurement in 42% D₂O is not shown due to the low contrast of the combination of dSapA and POPC to the solvent.

Structural parameters of the SANS measurements for the measurements in H₂O, 100% D₂O and 8% D₂O are shown in Table 8. The R_g value derived from the measurement in 100% D₂O ($R_g = 40.6 \pm 0.21 \text{ \AA}$) is smaller compared to the R_g values in H₂O ($R_g = 44.5 \pm 0.26 \text{ \AA}$) and 8% D₂O ($R_g = 44.3 \pm 0.31 \text{ \AA}$) due to the match-out of the dSapA. The D_{\max} and the V_P values are for the same reason smaller in 100% D₂O ($D_{\max} = 128 \text{ \AA}$, $V_P = 271 \text{ nm}^3$) compared to the measurements in H₂O ($D_{\max} = 139 \text{ \AA}$, $V_P = 397 \text{ nm}^3$) and 8% D₂O ($D_{\max} = 141 \text{ \AA}$, $V_P = 384 \text{ nm}^3$).

Table 8: Structural SANS parameter of MsbA incorporated into match-out deuterated Saposin A and hydrogenated POPC in different backgrounds with varying H₂O/D₂O ratios.

MsbA:dSapA:POPC	R_g (Å)	D_{max} (Å)	V_p (nm³)	I(0) (cm⁻¹)
in H₂O	44.5 ± 0.26	139	397	0.26 ± 0.0032
in 100% D₂O	40.6 ± 0.21	128	271	0.38 ± 0.0012
in 8% D₂O	44.3 ± 0.31	141	384	0.16 ± 0.0007

The model of MsbA:dSapA:POPC was adapted by the MPBuilder¹⁵⁹ model of MsbA:hSapA:POPC. 70% of the non-exchangeable hydrogen atoms were replaced with deuterium via a python script. This model was used to calculate with PEPSI¹³⁴ the theoretical scattering curve in H₂O, 8% D₂O, 42% D₂O and D₂O to fit them to the experimental data. The calculated scattering curves in H₂O (Figure 39A) and 8% D₂O (B) fit the experimental data with a low χ^2 of 0.53 in H₂O and 0.36 in 8% D₂O. The measured scattering intensity at 42% D₂O is compared to the other measurements lower due to the opposite SLD differences to the solvent resulting in a scattering curve with only minimal features. The calculated fit of the deuterated model was an almost flat line with a χ^2 of 0.52 (C). The calculation of MsbA:dSapA:POPC in 100% D₂O does not fit the experimental data (χ^2 of 32.7). Like the fitting of MsbA in the hydrogenated Salipro, PEPSI has difficulty calculating the exact hydration layers between the hydrogenated lipid headgroups and the D₂O.

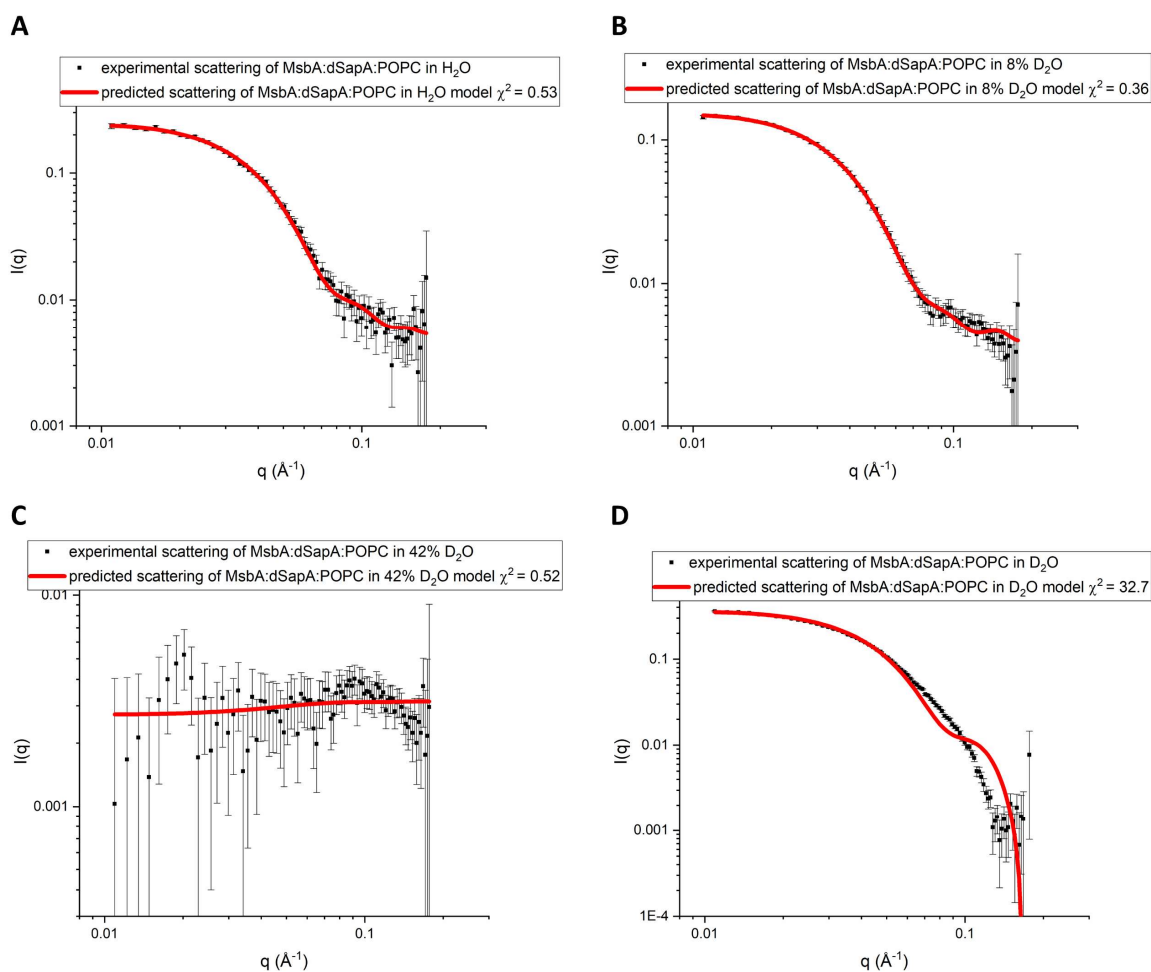


Figure 39: Comparison of the predicted scattering curve using PEPSI¹³⁴ from the model created in MPBuilder¹⁵⁹ to the experimental data of MsbA in match-out deuterated Saposin A and hydrogenated POPC in different backgrounds with varying H₂O/D₂O ratios. **A:** Comparison in H₂O. **B:** Comparison in 8% D₂O. The experimental data in H₂O (A) and 8% D₂O (B) matches the predicted scattering curve from the model. **C:** Comparison in 42% D₂O. The opposed SLD differences of dSapA and POPC to the solvent result in a low scattering intensity with only minor features. The fitting of the scattering results in an almost flat line. **D:** Comparison in 100% D₂O. The experimental data differ from the predicted data derived from the model resulting in a high χ^2 of 32.7.

With the contrast variation experiment of MsbA in a fully hydrogenated Salipro and a Salipro with match-out deuterated Saposin A and hydrogenated POPC in different backgrounds, we successfully matched out various components in a multicomponent complex. The experimental data was confirmed by PEPSI¹³⁴ calculations of models built in MPBuilder¹⁵⁹.

3.2.3 SANS experiment of ADP-Vi trapped MsbA in a matched out deuterated Salipro

After the successful match-out of different component of MsbA incorporated into, the next step was to match-out the entire Salipro in 100% D₂O by selective deuteration. For this, the match-out deuterated SapA described in section 3.2.1 was used.

The other deuterated component in the stealth Salipro are match-out deuterated Phosphatidylcholine (dPC) lipids. For a PC bilayer in 100% D₂O, the calculated deuteration level is 78% of the head group and 92% of the acyl chains to achieve neuron invisibility⁸⁰. These PC lipids must be produced in a specialised *E. coli* strain called AL95 because PC lipids are naturally not present in *E. coli*. This strain carries a plasmid that allows the expression of PC synthase encoded by the *Legionella pneumophila* pcsA gene¹⁶⁰. Growing this strain in 100% D-Enfors minimal media (with hydrogen containing salts) will produce labelled PC lipids which are matched out in 100% D₂O. The total lipids were extracted with a mixture of CHCl₃, MeOH and H₂O and the different lipid classes were isolated in a solid-phase extraction (SPE). An increasing amount of the polar MeOH to the non-polar CHCl₃ was used to elute different classes depending on the polarity of the lipid headgroups. The ratios (CHCl₃/MeOH) of 20:1, 15:1, 12:1, 9:1, 6:1, 4:1, 2:1, 1:1, (v/v) and 100% MeOH were used to cover a wide range going from a very non-polar to a very polar running solvent. The sample was dissolved in hexane and applied to the silica column. The elution fractions of the SPE were analysed by High-performance thin-layer chromatography (HPTLC) by applying the total lipid mix before the SPE, the elution fractions after the SPE and known standards to a TLC Silica coated plate. The plate was developed in CHCl₃:MeOH:Acetic acid 65:28:8 (v/v/v), stained with a primuline solution and visualised under UV light (Figure 40). A band corresponding to the PC and PE standard is visible in the total extract of lipids before the SPE. The upper band could be either PG or CL (standards not applied to the plate). The elution fraction of hexane shows no visible band because all lipids are still inside the column. In the 20:1 and 15:1 fraction, a band is visible, which could correspond to PG or CL. In the 12:1, 9:1, 6:1 and 4:1 fraction PE, and probably PG and CL were eluting. PC is starting to elute at a ratio of 2:1, together with PE and other lipids. At 100% MeOH, pure PC is eluting from the column.

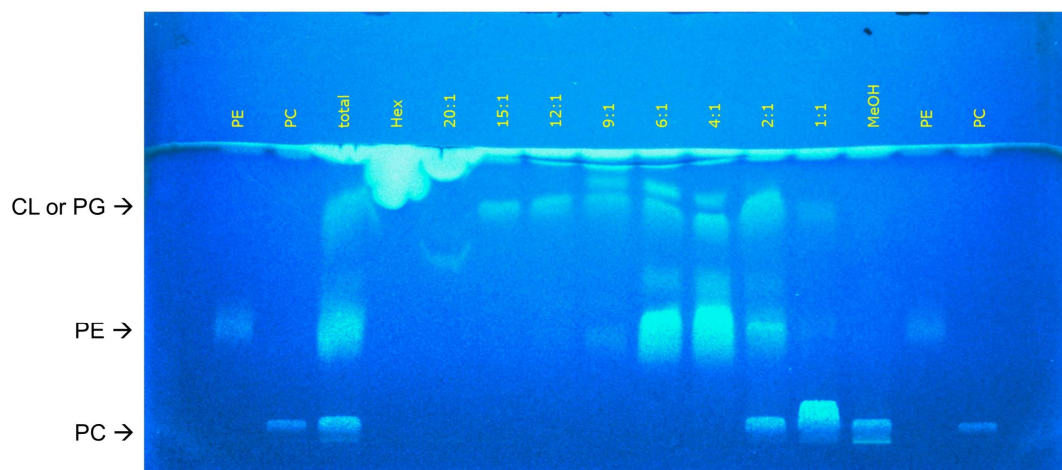


Figure 40: HPTLC analysis of the elution fractions of the SPE. The total lipids before the SPE and the elution fractions from the running solvents hexane, CHCl_3 :MeOH in the ratio 20:1, 15:1, 12:1, 9:1, 6:1, 4:1, 2:1, 1:1, v/v, and MeOH are shown alongside the PE, PC standards.

The fractions containing PC alongside other lipids were further purified with HPLC. The mobile phase was a gradient between solvent A ($\text{CHCl}_3/\text{CH}_3\text{OH}/\text{NH}_4\text{OH}$, 80:20.5:0.5, v/v) and solvent B ($\text{CHCl}_3/\text{CH}_3\text{OH}/\text{H}_2\text{O}/\text{NH}_4\text{OH}$, 60:35:5.5:0.5, v/v). The HPLC profile of the 2:1 fraction of the SPE is shown in Figure 41A. After the void volume of the column from ~13 – 15 min, the profile shows four different peaks (P1-P4) eluting after 34 min, 40 min, 43 min and 59 min. These peaks were collected separately and identified, comparing them to known lipid standards with HPTLC (Figure 41B). Peak 1 was identified as PG, peak 2 as CL, peak 3 as PE and peak 4 as PC.

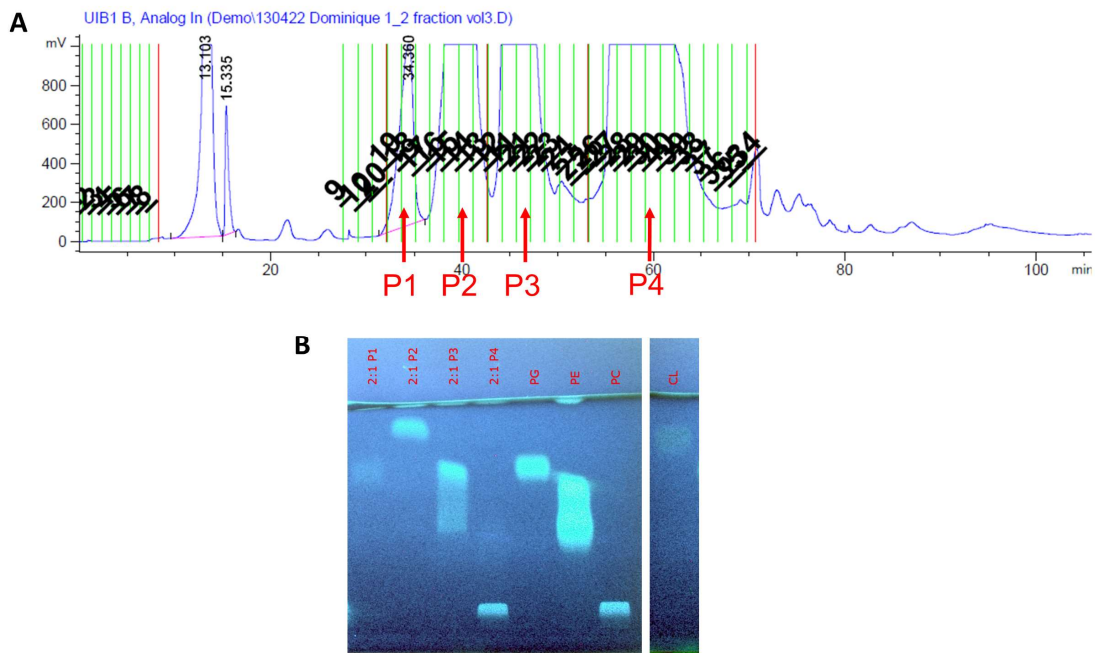


Figure 41: Analysis of the HPLC. **A:** HPLC profile of the 2:1 elution fraction of the SPE showing after the void peak four different peaks corresponding to different lipid classes. **B:** HPTLC analysis of peaks 1-4 from the HPLC. All lipid classes from each peak can be identified.

After the successful separation, the PC-containing fractions were pooled, and the solvent evaporated. After evaporation, the dry lipid film was resolved in a buffer containing 30 mM Tris pH 7.5, 150 mM NaCl and 100 mM cholate to obtain a 50 mM lipid stock solution.

To determine a more precise lipid concentration, a phosphate assay was performed. For this, several phosphate standards were prepared and measured together with the samples.

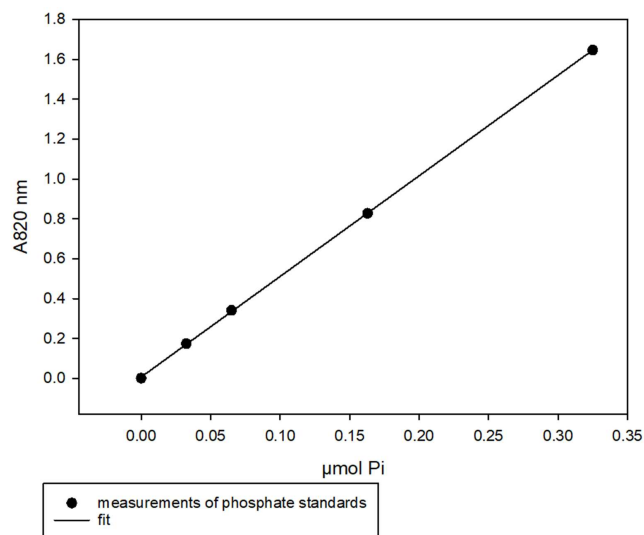


Figure 42: Phosphate assay of purified dPC lipids. The absorbance at 820 nm of the phosphate standards is shown as a function of phosphate concentration. A linear dependence is visible, allowing to create a linear fit through the data points. This fit is used to calculate the phosphate concentration of the dPC stock solution.

The absorbance at 820 nm was measured of the phosphate standards and the samples. A linear fit was created to describe the dependence of the amount of Pi in the standards to the absorbance at 820 nm. With this fit, the Pi concentration was calculated from the sample to determine the lipid concentration of the stock solution, resulting in a concentration of 30 mM of the dPC lipid stock solution.

The assembly conditions to form empty stealth Salipro was a ratio of 1:12 of deuterated SapA (dSapA) to deuterated PC (dPC). For MsbA reconstituted into stealth Salipro, the ratio was 1:4:20 of MsbA to dSapA to dPC/deuterated polar lipids. After detergent removal, the Salipros were formed and purified by SEC. The SEC profile (Figure 43) shows the assembly of MsbA into the two different stealth Salipros. There are two significant differences in the assembly with dpolar lipids compared to dPC. The first is the larger share of larger aggregates and other large particles in the samples containing the dpolar lipid mix. A possible explanation for the worse assembly could be the unknown composition of cardiolipin (CL), phosphatidylethanolamine (PE), phosphatidylglycerol (PG) and phosphatidylcholine (PC). Optimising the ratio between MsbA:dSapA:dpolar lipids could minimise the amount of aggregates in the assembly. The second difference is the earlier elution of MsbA in Salipro containing dPC, which indicates slightly larger particles of MsbA in deuterated Salipro containing dPC lipids. The successful incorporation of MsbA into stealth Salipro was confirmed with SDS-PAGE showing MsbA and dSapA in the same elution fraction.

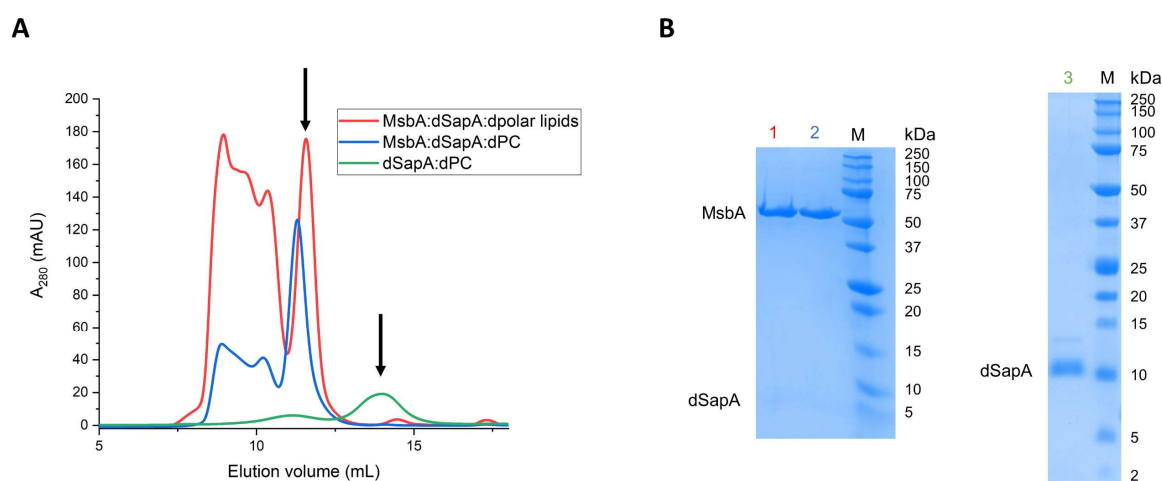


Figure 43: Reconstitution of MsbA into stealth Salipro with a deuterated polar mixture from *E. coli* (red) and deuterated PC (blue) and empty stealth Salipro (green). **A:** SEC profiles show the successful assembly of MsbA into stealth Salipro at 12 mL elution volume and the empty stealth Salipro at 14 mL. **B:** SDS-Page of SEC fractions at 12 mL showing the presence of MsbA and fractions at 14 mL of dSapA in the empty Salipro. 1 = MsbA in stealth Salipro with a deuterated polar mixture from *E. coli*, 2 = MsbA in stealth Salipro with deuterated PC, 3 = empty stealth Salipro, M = molecular weight marker. In both samples, void volumes are present.

The scattering signal of the empty stealth Salipro is more than one order of magnitude lower than MsbA incorporated stealth Salipro, indicating that the carrier proteins and lipids are not significantly contributing to the global scattering data and can be neglected in the data analysis. The almost flat line is only slightly above the experimental background, showing that the stealth Salipros are effectively matched out. The residual signal is likely from the statistical fluctuations in the deuteration level of SapA and lipids. The scattering profile for MsbA in stealth Salipro shows a typical profile for biological samples (Figure 44). The cryo-EM model of MsbA trapped in the occluded state (PDB ID: 7bcw, see section 3.1.1) was used to compute with PEPSI¹³⁴ the scattering data of MsbA and is compared to the experimental data. The predicted scattering profile matches the profiles in the entire q-range of both samples, resulting in a χ^2 of 4.26 to MsbA in the occluded state in Salipro containing a dpolar lipid mix and a χ^2 of 2.07 to MsbA in the occluded state in Salipro with dPC. The influence of the different lipids is minimal with slightly smaller dimensions of MsbA in stealth Salipro containing dPC with an R_g of $38.3 \pm 1.62 \text{ \AA}$ compared to $40.4 \pm 1.29 \text{ \AA}$ to Salipro with a polar lipid mix from the Guinier approximation. The minimal scattering contribution of the lipid carrier to the SANS data, suggesting the measured scattering intensity derives only from MsbA. The R_g values are also matching the predicted R_g of $37.0 \pm 0.04 \text{ \AA}$ of the cryo-EM model. Also, the other structural parameters including D_{\max} and V_P are very similar between the predicted cryo-EM model and the experimentally measured samples (see Table 9).

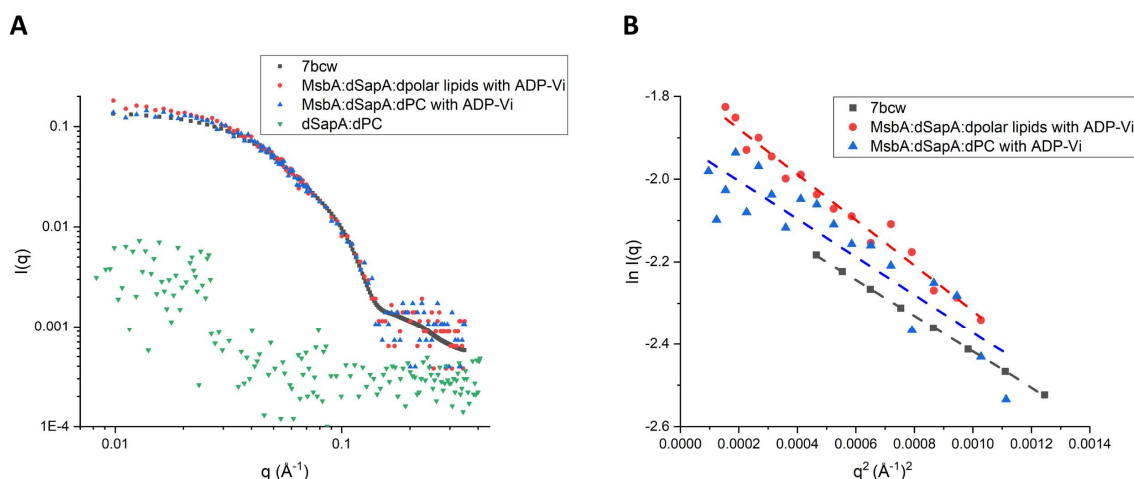


Figure 44: Small-angle neutron scattering of MsbA in the occluded state incorporated into stealth Salipro. **A:** Predicted SANS scattering curve of the cryo-EM model 7bcw of occluded MsbA shown in black. Scattering profiles of MsbA trapped in the occluded state with ADP and vanadate in deuterated Salipro containing a deuterated polar lipid mix from *E. coli* are shown in red and deuterated PC lipids in blue. Both experimental data fit with the predicted scattering curve from the MsbA model from cryo-EM, indicating that deuterated Salipros do not contribute to the scattering signal. Scattering data of empty deuterated Salipro is shown in green. The low scattering signal of the deuterated empty Salipro indicates the neglectable influence of the scattering compared to the MsbA samples. **B:** Guinier region of the SANS data of the cryo-EM model of MsbA (7bcw) shown in black

and occluded MsbA in stealth Salipro with a deuterated *E. coli* polar mixture in red and deuterated PC in blue. The linearity indicates the absence of inter-particle interferences.

The distance distribution plots from the predicted model and the experimentally measured samples differ slightly in the region between 45 – 120 Å. However, the most prominent peak at 32 Å is present in all curves (Figure 45). The Kratky plot shows a pronounced peak at 0.06 Å⁻¹, indicating a folded and non-flexible structure of MsbA trapped in the occluded state with ADP-Vi in Salipro.

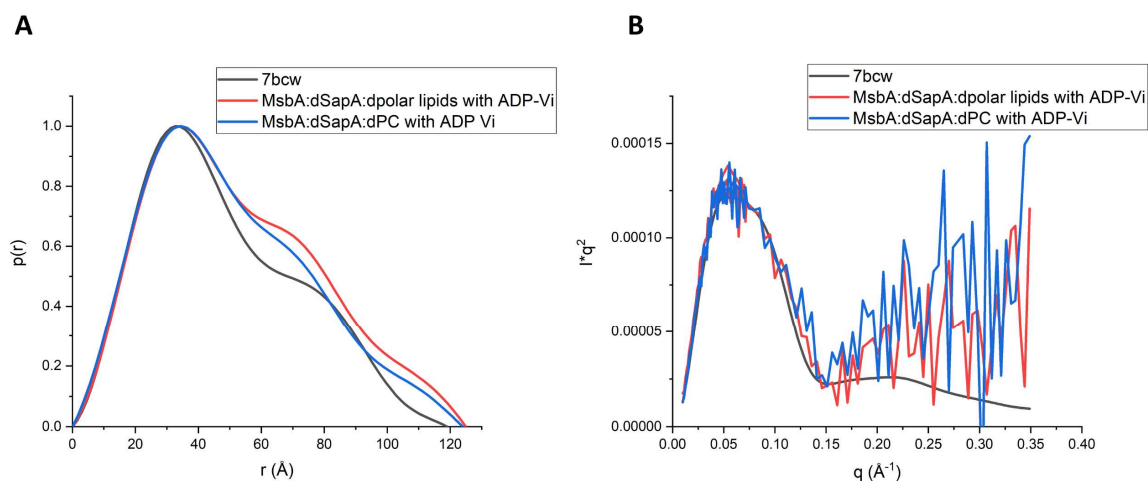


Figure 45: Analysis of SANS data of occluded MsbA in stealth Salipro. **A:** Distance distribution plots of the predicted SANS curve of MsbA (from 7bcw) shown in black and occluded MsbA in matched out deuterated Salipro with deuterated polar lipid mixture from *E. coli* in red and deuterated PC in blue, indicating that particles from the experimental data have a slightly higher D_{\max} than the predicted MsbA. **B:** Kratky plot of the data of A. The peak position of the experimental data is very similar to 7bcw, indicating a comparable size of samples.

Another way to confirm that the stealth Salipro are neutron invisible is to calculate the electron density of the solution scattering data and compare it to a known MsbA model. If the electron density has similar dimensions as the model, this would indicate that the Salipro is matched out.

Table 9: Structural SANS parameters of the predicted MsbA model 7bcw and MsbA in stealth Salipro with deuterated polar lipids from *E. coli* and deuterated PC.

	R_g (Å)	D_{\max} (Å)	V_P (nm ³)
7bcw	37.0 ± 0.04	119	156
MsbA:dSapA:dpolar lipids with ADP-Vi	40.4 ± 1.29	125	176
MsbA: dSapA:dPC with ADP-Vi	38.3 ± 1.62	124	170

The SANS data was used to calculate the electron density using DENSS¹³⁵. The obtained electron densities of MsbA in Salipro with a dpolar lipids mix and dPC are very similar, which is not surprising because the lipids and the belt proteins should be matched out in both cases. The predicted size of the electron density matches the MsbA model in the occluded state (PDB ID: 7bcw), indicating the match-out of the Salipro (Figure 46). The electron density in the TMDs and the NBDs is very high (colourised in red), showing the high compact areas of MsbA in the occluded state.

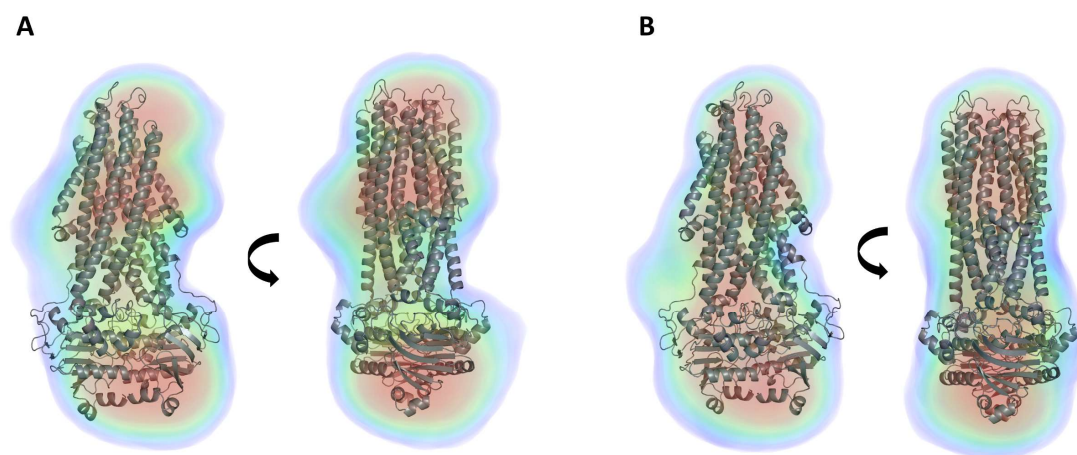


Figure 46: Electron density *ab initio* shape reconstruction by DENSS¹³⁵ from the experimental SANS data of MsbA incorporated into stealth Salipro containing a deuterated lipid polar mixture from *E. coli* (A) and deuterated PC lipids (B) superimposed on the cryo-EM structure of MsbA (7bcw). Electron density maps are shown in volumes coloured according to density.

Comparing the experimental SANS data to the cryo-EM model of the occluded MsbA and the SAXS data, a successful incorporation of MsbA into stealth Salipro can be confirmed with no scattering contribution of the lipid carrier in 100% D₂O. Furthermore, all structural parameters like R_g and D_{max} as well as the calculated electron densities are matching the MsbA model. Overall, this study demonstrates the suitability of deuterated stealth Salipro to SANS as a tool to analyse membrane proteins embedded in a native-like lipid environment.

3.2.4 SANS experiment of MsbA:dSapA:dPC leads to larger particles

If the ratio between membrane protein, carrier protein and lipids is off in the assembly, larger particles and aggregates are often formed. The following example illustrates the importance of determining the exact lipid concentration to set up the correct ratio for the assembly. The lipids for this experiment were extracted and purified with the protocol of Maric *et al.*⁸¹, yielding low amounts of dPC. However, the lipid concentration was not precisely determined in the phosphate assay to avoid losing more dPC lipids. Instead, the concentration was estimated by

the dry mass of the lipid film. This led to the problems discussed above in the resulting assembly. The SEC profile shows three peaks (Figure 47). The first peak at 8 mL is the void volume of the S200 10/300 column and corresponds to larger aggregates. In the SDS-PAGE analysis of corresponding elution fractions, only one band of MsbA is visible, showing that these aggregates are mostly MsbA proteins. In the second and third peaks, a MsbA band is visible and a band from dSapA. Based on the elution time, the particle population corresponding to peak 2 is bigger than the population of peak 3. Both samples were analysed in the apo and occluded trapped state in a SANS experiment.

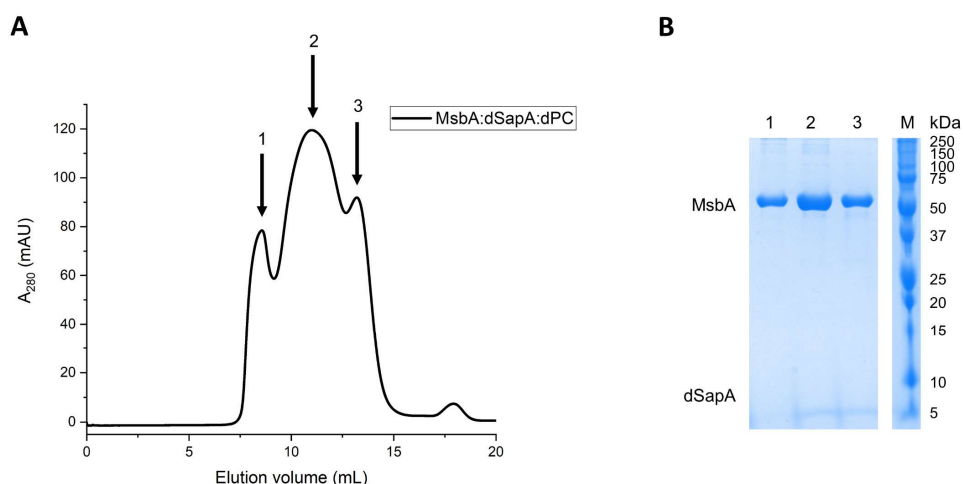


Figure 47: Reconstitution of MsbA into stealth Salipro with deuterated PC. **A:** SEC profile shows a void peak (peak 1) and two additional peaks. **B:** SDS-Page of SEC fractions of peak 1 - 3 showing the presents of MsbA. The band of dSapA is only visible in peaks 2 and 3.

The scattering profiles of peak 2 differ only in the small q -range showing different particle dimensions between the apo and the ADP-Vi trapped MsbA. A possible explanation is that MsbA:dSapA:dPC without ADP-Vi is less stable compared to the more compact trapped MsbA, leading to partly aggregated larger particles. In contrast, the profiles of peak 3 also show differences in the mid q -range. The size parameters from the scattering data confirm that the particle population of peak 2 is larger compared to the particles of peak 3. The R_g of the apo MsbA in match-out deuterated Salipro of peak 2 is $96.3 \text{ \AA} \pm 0.66$ while the R_g for the apo MsbA of peak 3 is only $61.2 \text{ \AA} \pm 1.10$. Also, the D_{\max} is differs significantly from 336 \AA of apo MsbA of peak 2 to 193 \AA of peak 3.

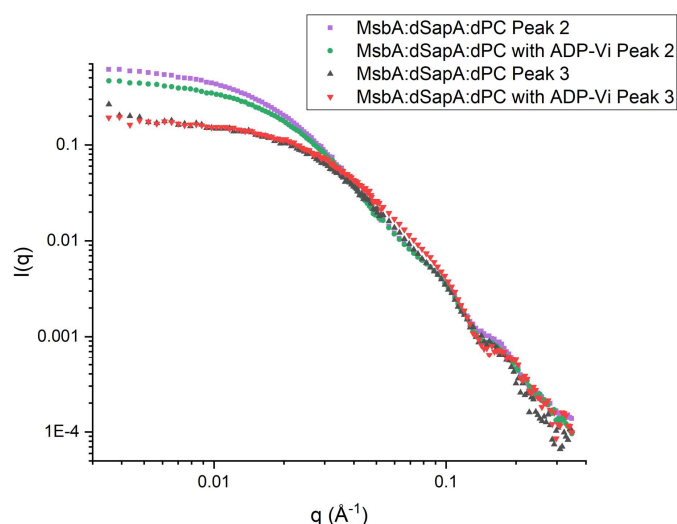


Figure 48: Small-angle neutron scattering of MsbA in the open and occluded state incorporated into stealth Salipro. Scattering profiles of peak 2 with (green) and without ADP-Vi (purple) plus peak 3 with (red) and without ADP-Vi (black). The differences in small and mid q -range show different populations of particles.

The expected R_g for MsbA in stealth Salipro is ~ 40 Å with an D_{\max} of ~ 125 Å (see section 3.2.3). Both populations from peaks 2 and 3 have significantly bigger dimensions. The next step is trying to explain the larger particles. One possibility is the incorporation of multiple MsbA proteins in one Salipro. To test this hypothesis, a dimeric model of the cryo-EM structure of MsbA trapped in the occluded state (PDB ID: 7bcw) was built (Figure 49). From this dimeric model, a theoretical scattering profile was calculated using PEPSI¹³⁴. These calculated scattering data can be compared to the experimental data of both populations, assuming the Salipro particles are entirely neutron invisible.

Table 10: Structural SANS parameters of peak 2 and 3 and the predicted MsbA-dimer model from 7bcw.

	R_g (Å)	D_{\max} (Å)	V_P (nm ³)
MsbA:dSapA:dPC Peak 2	96.3 ± 0.66	336	1688
MsbA:dSapA:dPC with ADP-Vi Peak 2	88.6 ± 0.78	293	1242
MsbA:dSapA:dPC Peak 3	61.2 ± 1.10	193	394
MsbA:dSapA:dPC with ADP-Vi Peak 3	55.7 ± 0.70	187	323
7bcw dimer	53.5 ± 0.05	184	296

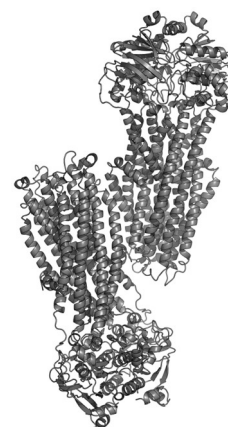


Figure 49: Dimeric model of 7bcw.

Based on the structural parameters, the particle population of peak 3 fits the predicted parameters of the dimeric model. The R_g of the dimeric model is 53.5 Å \pm 0.05 Å and in the

same range as the population of peak 3 with ADP-Vi ($R_g = 55.7 \text{ \AA} \pm 0.70 \text{ \AA}$). Also, the D_{\max} of 184 \AA of the model fits the experimental data ($D_{\max} = 187 \text{ \AA}$) and the V_P (model = 296 nm^3 , peak 3 with ADP-Vi = 323 nm^3). Only minimal differences in mid and minor differences in high q -range (Figure 50) are present between the predicted scattering profile of the dimeric model and the experimental data of peak 3 with ADP-Vi. Also, the scattering data in the Guinier region are almost identical.

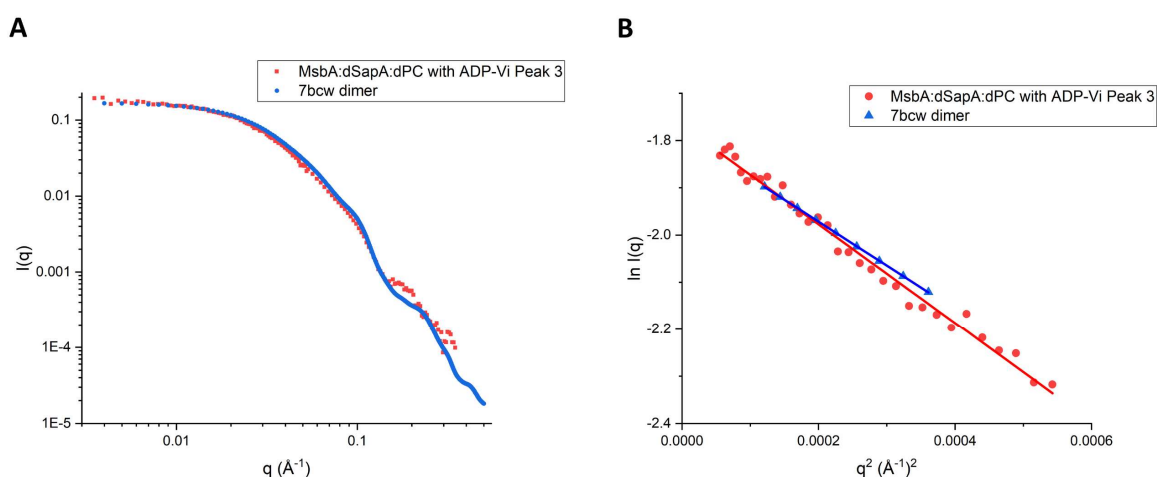


Figure 50: Small-angle neutron scattering of MsbA in the occluded state incorporated into stealth Salipro. **A:** Predicted SANS scattering curve of dimeric 7bcw of occluded MsbA shown in blue. Scattering profiles of MsbA trapped in the occluded state with ADP and vanadate in deuterated Salipro particles are shown in red and deuterated PC lipids in red. The experimental data fit with the predicted scattering curve from the dimeric MsbA model, indicating the possibility of assembling multimers into stealth Salipro. **B:** Guinier region of the SANS data of the MsbA-dimer (7bcw) is shown in blue and occluded MsbA in stealth Salipro in red.

The distance distribution plots, and the Kratky plots of the predicted model and the experimental data are very similar, indicating the high structural similarity of the population of peak 3 with ADP-Vi to the model (Figure 51).

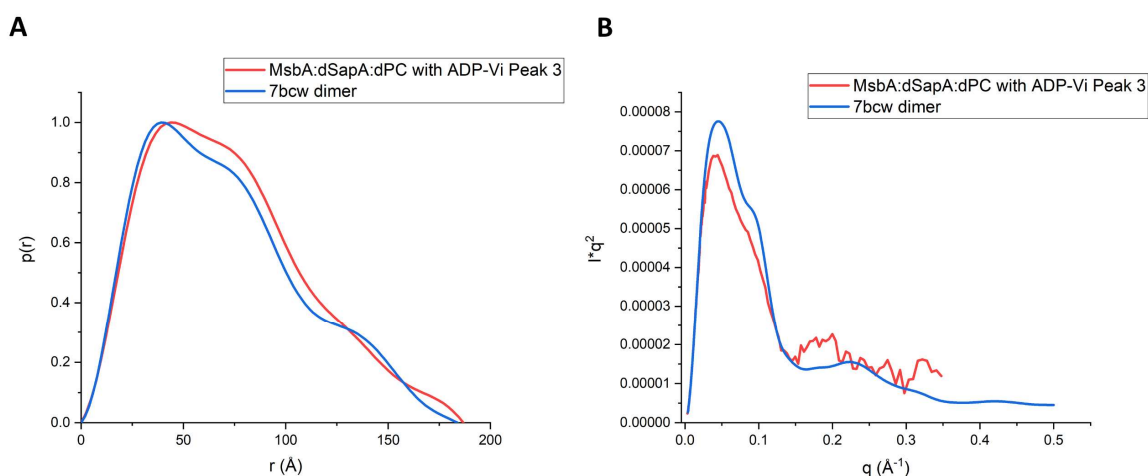


Figure 51: Analysis of SANS data of occluded MsbA in stealth Salipro. **A:** Distance distribution plots of the predicted SANS curve of the dimeric MsbA (from 7bcw) shown in blue and occluded MsbA in matched out deuterated Salipro red, indicating that particles from the experimental data have a slightly higher D_{\max} than the predicted MsbA-dimer. **B:** Kratky plot of the data

of A. The peak position of the experimental data is very similar to 7bcw, indicating a comparable size of samples. Also, the prominent peak at 0.05 \AA^{-1} in both samples indicates low flexibility in the proteins.

Another indicator that the particles of peak 3 could be MsbA dimers incorporated into stealth Salipro is the matching electron density of the experimental data to the model. The electron density was calculated using DENSS¹³⁵ and superimposed on the dimeric model. Especially the areas with a high electron density (coloured in red) match the shape of the two MsbA proteins.

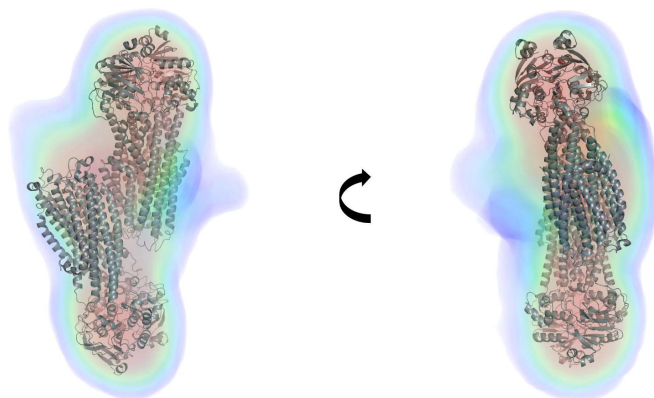


Figure 52: Electron density ab initio shape reconstruction by DENSS¹³⁵ from the experimental SANS data of peak 3 superimposed on the MsbA-dimer (7bcw). Electron density maps are shown in volumes coloured according to density.

The identification of the particles of peak 2 was challenging. The structural parameter and the scattering data are not fitting any MsbA multimer. More likely is that the particles are a fusion of multiple MsbA-filled stealth Salipro forming large particles.

The imprecise determination of the lipid concentration led to an off-ratio during the assembly. The results were two different populations of particles. The smaller particles could be identified as a MsbA dimer incorporated into stealth Salipro. This shows the flexibility of the Salipro system and could be used in future projects to analyse protein multimers by changing the ratio during the assembly, as well as the importance of the precise ratio in the assembly.

3.3 Chapter 3 – Time-resolved small-angle X-ray scattering (SAXS) analysis of MsbA in different lipid carrier systems

In a time-resolved experiment, multiple conformational states and their intermediates can be analysed over time. These motions are essential for numerous biological phenomena like enzymatic catalysis and the time scale can vary between femtoseconds up to minutes¹⁶¹. Therefore, probing and capturing different conformational states and intermediates to analyse their lifetime and structure is essential to understand protein function. Small-angle X-ray scattering (SAXS) is a valuable method to obtain direct structural information of proteins in solution. In this thesis, two different techniques were combined with SAXS to perform different time-resolved experiments. First, the stopped-flow technique was used to analyse the kinetics of wild-type (wt) MsbA incorporated in Salipro in a time scale of milliseconds up to seconds. In the second technique, the E506Q mutant of MsbA (MsbA-EQ) in MSP-based nanodiscs and Salipro was analysed by rapidly mixing with ATP-Mg²⁺ followed by measurements in batch mode. This technique covers structural changes from minutes to hours and is ideal for the slow kinetics of the MsbA-EQ mutant.

3.3.1 Stopped-flow time-resolved SAXS analysis of wt MsbA in Salipro

In a stopped-flow time-resolved SAXS experiment, solutions were mixed rapidly and injected into a capillary, where X-rays were scattered and detected afterwards to follow numerous ligand-driven kinetic processes. This technique can cover time scales from milliseconds to seconds. In this thesis, stopped-flow time-resolved SAXS was used to analyse the wt MsbA in Salipro in combination with ATP-Mg²⁺ to quantify and characterise structural changes and the kinetics in solution.

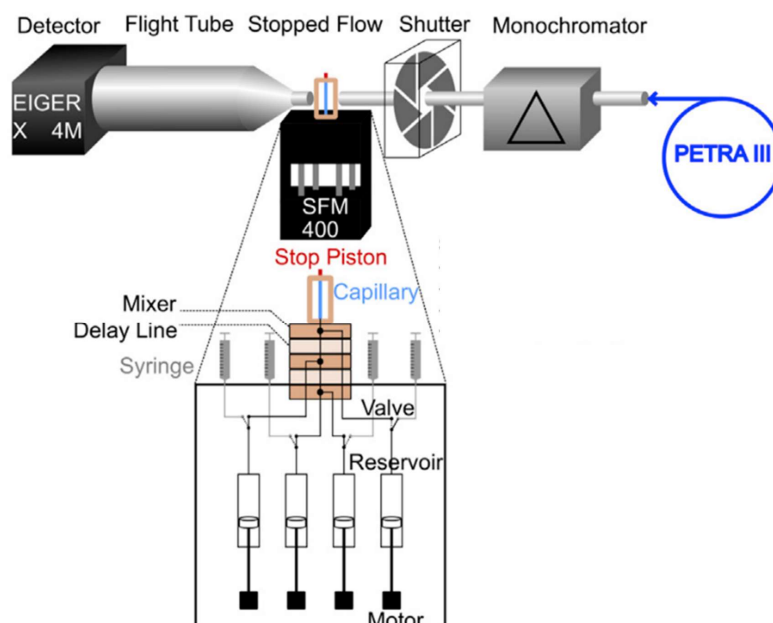


Figure 53: Set up for stopped-flow time-resolved SAXS measurements at EMBL’s P12 Beamline, PETRA III. A stopped-flow mixer (Bio-logic, Seyssinet-Pariset, France) is replacing the beamline’s regular sample changer. After mixing the solutions, the liquid flow is stopped by stopping the motors that push the liquids through the capillary. Taken from Josts *et al.*⁶⁸.

MsbA was purified and assembled into Salipro as described in section 2.4 and 2.8. 100 μM protein was mixed 1:1 with ATP-Mg²⁺ (100 μM) using the stop-flow device (Bio-logic, Seyssinet-Pariset, France), injecting 80 μL each, and was measured on the Bio-SAXS beamline P12⁵² on the storage ring PETRA III (EMBL/DESY, Hamburg, Germany). Figure 54 shows the scattering differences to time point zero (after 0 ms). Differences are visible between the very small q -range up to 0.2 nm^{-1} confirming measurable differences over time with SAXS.

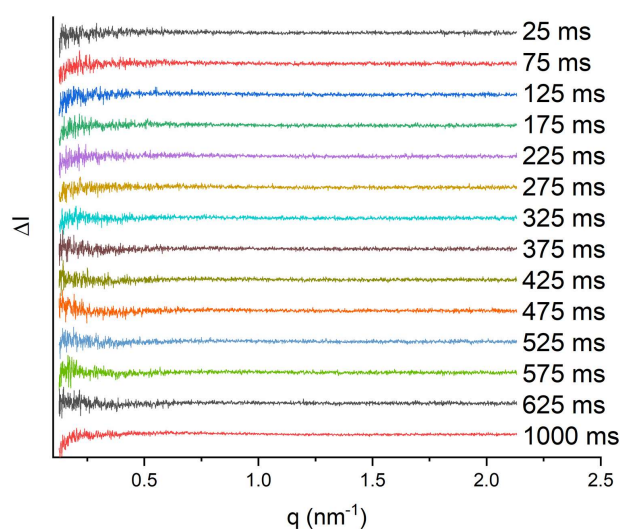


Figure 54: Stopped-flow time-resolved SAXS data. Scattering differences of MsbA incorporated in Salipro after mixing with ATP + Mg²⁺ (100 μM each). Differences to time point zero (0 min) occur at 0.2 nm^{-1} .

First, we analysed the starting conformation ($t = 0$ ms) of MsbA incorporated in Salipro. For this, the five different EM maps of apo MsbA in Salipro classes from the cryo-EM analysis (3.1.2) were used to calculate the theoretical scattering curve to compare them with the experimental data. The second most open class 1 (Figure 55B, yellow) fits the experimental data best with a $\chi^2 = 6.18$ (Figure 55A). All other classes have a higher χ^2 than the experimental data and are summarised in Table 11. However, the $\chi^2 = 6.18$ is still relatively high because of the potential mixture of different opening angles of MsbA in the apo state in solution. The scattering signal is a sum of all particles in solution, which impedes the exact determination of the opening angle of MsbA in a time-resolved SAXS experiment.

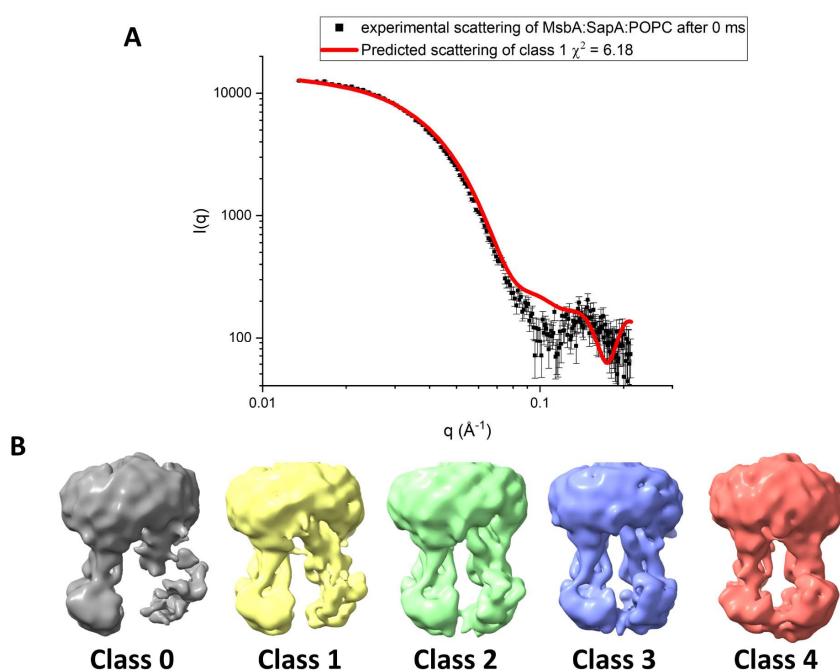


Figure 55: Analysis of starting conformation of MsbA in Salipro in a time-resolved experiment. **A:** Comparison of the predicted scattering using PEPSI¹³⁴ of the cryo-EM structure of class 1 to the experimental data after 0 ms. The predicted scattering curves match the experimental data relatively well, resulting in a χ^2 of 6.18. **B:** Different classes from the cryo-EM analysis of the apo MsbA in Salipro (see section 3.1.2).

Table 11: χ^2 values of the five different classes from the cryo-EM analysis of apo MsbA in Salipro compared to the experimental data after 0 ms (see section 3.1.2).

MsbA:SapA:POPC	χ^2 to experimental data after 0 ms
Cryo-EM class 0	10.13
Cryo-EM class 1	6.18
Cryo-EM class 2	7.12
Cryo-EM class 3	8.15
Cryo-EM class 4	11.37

The R_g changes in the experimental data can be used to follow conformational changes of the sample in a time-resolved SAXS experiment. In Figure 56A the R_g difference to 0 ms is shown over time. The R_g decreases in the first 100 ms to an ΔR_g of $-1.6 \pm 0.4 \text{ \AA}$. Afterwards, the R_g increases until after 300 ms the R_g of time point zero ($t = 0$) is reached. Until 550 ms, the R_g remains increasing to an ΔR_g of $1 \pm 0.4 \text{ \AA}$. After 1000 ms, the R_g is decreased to ΔR_g of $-1.3 \pm 0.2 \text{ \AA}$. With the help of MsbA models, we try to better understand the R_g evolution in the first 1000 ms. The model of the EM class 1 (see 3.1.2) was used to describe the structure of time point zero ($t = 0$) (see Figure 55A). The R_g of this model was used as a starting point (after 0 ms) to compare ΔR_g to other known MsbA conformations without the Salipro disc (Figure 55B). The occluded conformation of MsbA trapped with ADP-Vi from the cryo-EM analysis (PDB: 7bcw¹³³, see 3.1.1) has an ΔR_g of $-1.8 \pm 0.1 \text{ \AA}$ to the R_g of class 1. A very similar ΔR_g is observed after 100 ms in the experimental data. The outward open state of MsbA (PDB: 3b60¹⁶) has a slightly higher ΔR_g of $-1.7 \pm 0.1 \text{ \AA}$. Therefore, it is difficult to differentiate between the occluded and the outward open state in the SAXS data. The overshoot of R_g to class 1 (after 0 ms) could be explained by a slightly wider inward open state of MsbA. Recently, a wide inward open state of MsbA was described in *E. coli* cells and cell-derived membranes in the presence of nucleotides¹⁶². This state is present between the phosphate and ADP release and facilitates the binding of a new substrate in the transmembrane domains. In this publication, the authors claim that the wide inward open state is impossible to form in nanodiscs due to the funnelling effect of the discs. Whether this state can be reached in Salipro is not known. The R_g calculations of the earlier described wide inward open state of MsbA in detergent (PDB: 6bl6²⁰) yielded an ΔR_g of $10.2 \pm 0.2 \text{ \AA}$ that could not be reached in Salipro based on the experimental data. However, the calculations of the R_g of class 0 (class with the largest opening angle from the apo MsbA cryo-EM analysis, see 3.1.2) result in an ΔR_g of $0.7 \pm 0.1 \text{ \AA}$. This ΔR_g is reached after 400 ms in the experimental data. The last data point at 1000 ms could be the start of the next catalytic cycle and the transition to the occluded conformation of MsbA (ΔR_g of occluded model = $-1.8 \pm 0.1 \text{ \AA}$, ΔR_g of experimental data after 1000 ms = $-1.3 \pm 0.2 \text{ \AA}$). A catalytic cycle was created (Figure 55C) based on the chronological order of the calculated R_g from the MsbA models compared to the experimental data. The inward open state of MsbA, similar to class 1, transitions to the occluded state (PDB: 7bcw) after binding ATP in the nucleotide-binding domains (NBDs). It is still unknown if the fully occluded state is possible in physiological conditions in combination with lipid A, glycolipids or lipopolysaccharides bound to MsbA. A potential other conformation could be that the two NBDs are dimerised but in the core between the transmembrane domains is still space for the substrate. This described

state could not be isolated yet. The transition from the occluded state to the outward open state (PDB: 3b60) is challenging to determine in SAXS due to the very similar R_g . However, it is suspected that the outward open state follows the occluded state to transport the potential substrate. Afterwards, MsbA changes to a wider inward open state (class 0), followed by the ADP and Pi release and the transition back to the narrower inward open state (class 1). This order controverts Mi *et al.*¹⁷. They describe that the Pi release happens before transitioning back to the inward open state (between outward open and inward open state). However, our time-resolved SAXS data from the EQ-MsbA mutant (see section 3.3.2) indicates almost no Pi release in the Baginski assay (Figure 60) in combination with an overshoot in R_g (Figure 63, Figure 68). This overshoot could also be explained by a wider inward open state, meaning that MsbA is transitioning first to the wider inward open state (overshoot in R_g) and is releasing Pi afterwards. Additional experiments should be necessary to confirm the hypothesis.

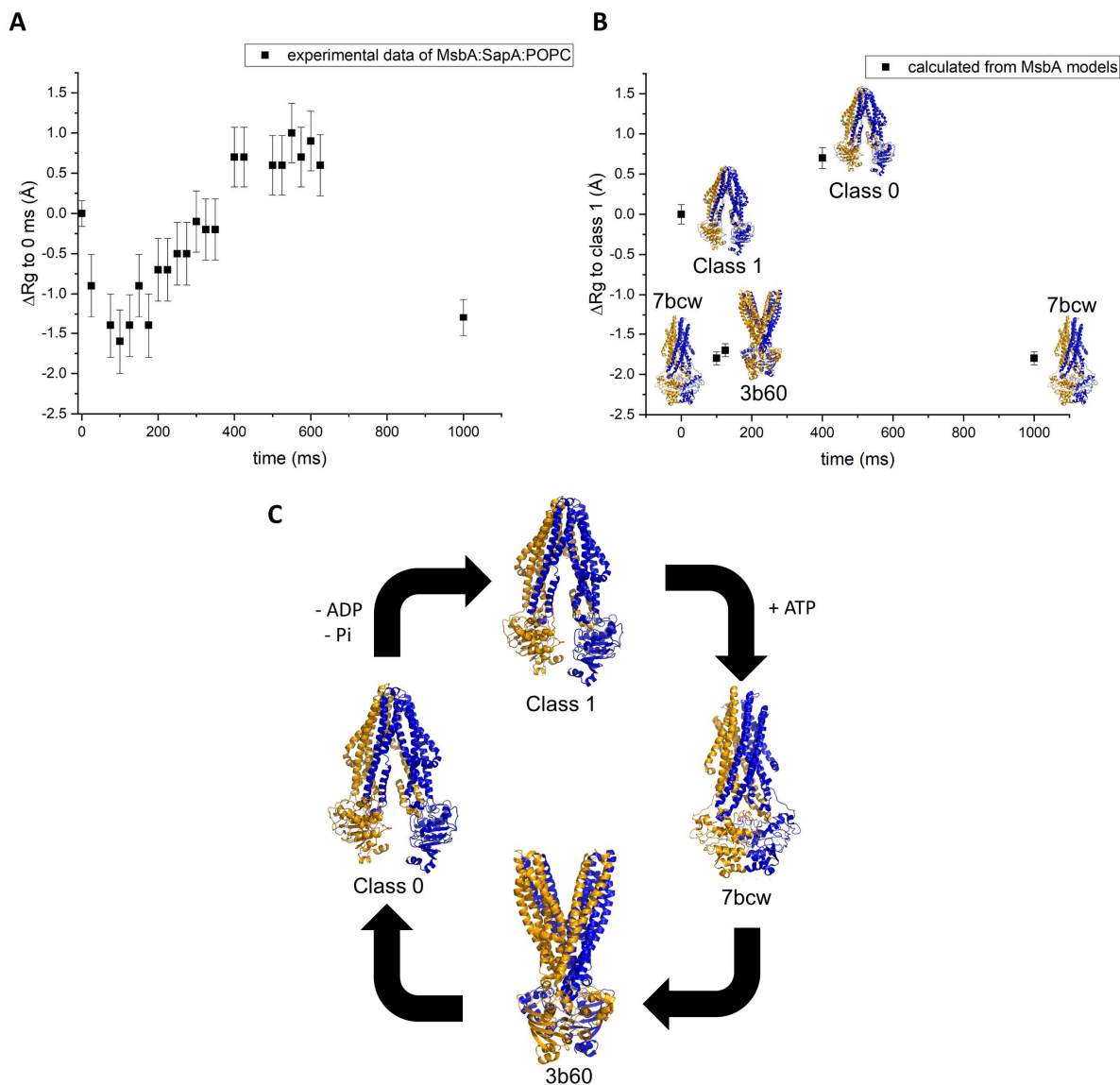


Figure 56: Evolution of R_g of MsbA in Salipro over the first 1000 ms. **A:** Experimental R_g differences to 0 ms. The R_g decreases in the first 100 ms to an ΔR_g of -1.6 ± 0.4 Å. Afterwards, the R_g increases until 550 ms to an ΔR_g of 1 ± 0.4 Å and decreases again to -1.3 ± 0.2 Å after 1000 ms. **B:** Calculated R_g differences from MsbA models to class 1 from the cryo-EM analysis (see 3.1.2). The calculated ΔR_g of our occluded cryo-EM structure PDB: 7bcw¹³³ (see 3.1.1) of -1.8 ± 0.1 Å fits the R_g value of experimental data after 100 ms. The outward open conformation of MsbA (PDB: 3b60¹⁶) has an ΔR_g of -1.7 ± 0.1 Å and could potentially be present after 125 ms. Positive ΔR_g values could be explained by the more open state of class 0 (see 3.1.2) compared to class 1. After 1000 ms, the ΔR_g is again -1.8 ± 0.1 Å. This could be the occluded state from the next catalytic cycle. **C:** Potential enzymatic cycle of the respective conformations.

In the singular value decomposition (SVD) analysis of MsbA in Salipro, the data is well described with two independent components (Figure 57). The first two components are above the non-zero singular values of the diagonal matrix. The third basis function of the SVD (Figure 57B, blue curve) includes only noise.

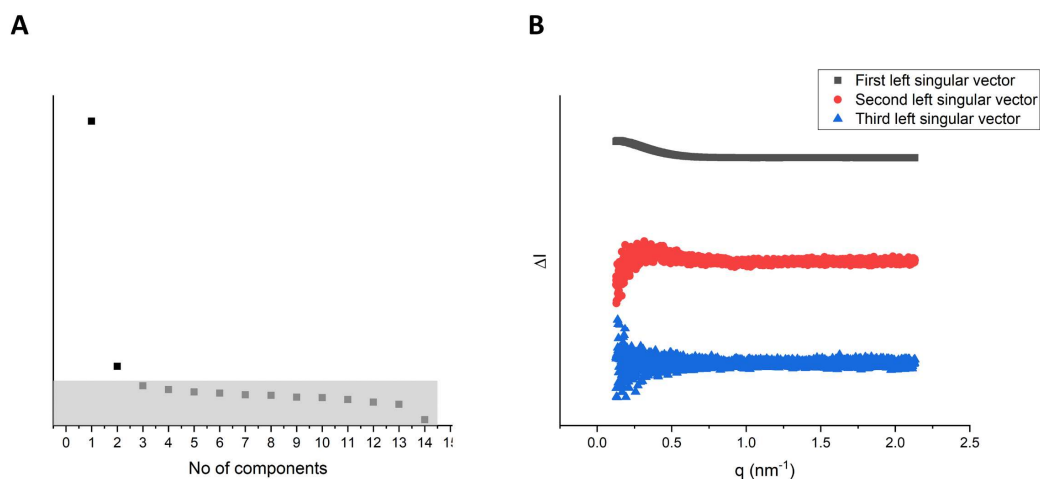


Figure 57: Singular-value decomposition (SVD) analysis of MsbA in Salipro. **A:** Number of independent components based on the non-zero (above the grey area) singular values of the diagonal matrix suggests that there are two major components. **B:** The first three basis functions from the SVD analysis of the difference curves indicate the presence of two independent components in the time-resolved SAXS data. The third basis component (blue) corresponds to noise.

Two individual components represent the experimental data. These components contribute to the scattering curve with different contributions over time. Component 1 (Figure 58, black) is not contributing at the start of the reaction. The contribution increases until after 450 ms, followed by a decrease almost back to zero contribution after 1000 ms. Component 2 (red) starts with a relatively high contribution of 0.7 and increases until 100 ms. Afterwards, the contribution decreases until after 400 ms it is almost zero. The component contribution of component 2 increases again to nearly 1 after 1000 ms. Component 1 could represent the wider inward open state of MsbA. The high contribution after 450 ms fits to the high R_g in Figure 56A, which could be explained by the wider inward open state. After 450 ms, the contribution decreases due to the transition from the wider inward open to the wide inward open, followed by the occluded state after 1000 ms. Component 2 could be a mixture of the inward open and occluded state of MsbA. Starting already at a high contribution is the inward open state of the protein. This contribution increases in the first 100 ms due to the ATP binding and the occlusion of the NBDs. After that, the contribution decreases with the transition to the outward open and the wider inward open state. The forming back to the inward open state and the start of the next catalytic cycle and the building of the occluded state after 1000 ms increases the contribution of component 2.

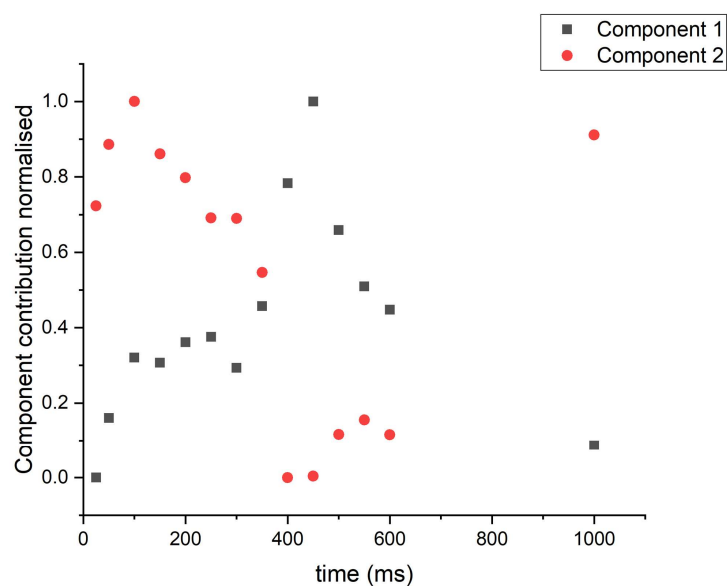


Figure 58: Individual normalised component contribution of the two independent components present in the SVD analysis of MsbA in Salipro measured in a time-resolved stopped-flow SAXS experiment. The contribution of component 1 (black) increases in the first 450 ms, followed by a decrease until almost zero contribution after 1000 ms. Component 2 (red) starts with a contribution of 0.7 and the contribution increases in the first 100 ms. Afterwards, the contribution decreases until after 400 ms component 2 is almost zero, followed by an increase until 1000 ms.

From the time-resolved stopped-flow SAXS experiment, we got detailed insights into the states of MsbA in Salipro during the reaction cycle. Especially the overshoot of R_g compared to the R_g of the starting conformation was not observed in a Salipro for MsbA before. This overshoot could be explained by a wider inward open state of MsbA after the outward open state. The existence of a wide inward open state in physiological conditions was recently confirmed¹⁶² but was never observed in lipid carrier discs. In Salipro, MsbA cannot reach the very wide inward open state according to Galazzo *et al.*¹⁶², but we monitored a small but significant increase in R_g . The very wide inward open conformation could not be reached due to the funnelling effect of the Salipro to MsbA.

3.3.2 Time-resolved batch mode SAXS analysis of MsbA-EQ in lipid carrier systems with triggering via mixing

The E506Q mutant of MsbA (MsbA-EQ) is used for studying the kinetics of MsbA. The point mutation is located downstream in the Walker B motif¹⁶³. This substitution of glutamic acid (E) to glutamine (Q) was studied in several transporter complexes such as MalK, HlyB-NBD PDR5 and MJ0796 and the transporter BmrA. These transporters are still able to bind ATP but cannot hydrolyse it^{163–166}. In contrast, studies on the intracellular peptide transporter Mdl1p showed that the ATP-induced dimer is able to hydrolyse ATP¹⁶⁷. The effect of the E506Q

mutation on MsbA was studied in liposomes by Schultz *et al.*¹⁶⁸. The ATP binding capability was measured in a fluorescent ATP binding assay. The ATP dissociation constant (K_d) is 0.51 μM for the fluorescence ATP analogue TNP-ATP, similar to the wt (0.32 μM for TNP-ATP¹⁶⁹). The study of the ability to hydrolyse and release the products of ATP hydrolysis indicates that the mutation significantly reduces the ability of ATP hydrolysis. However, it was shown that the mutation still allows MsbA to hydrolyse ATP. 5 μM protein needed 6 h to hydrolyse 10 μM ATP with excess of Mg^{2+} at room temperature while the wt required less than 30 min for the same amount of ATP¹⁶⁸. MsbA-EQ in different lipid carriers was used to perform time-resolved batch-mode SAXS experiments. Due to the significantly reduced kinetics, it was possible to study different states of the reaction cycle using manual mixing to trigger the reaction. The aim was to see the influence of the point mutation compared to the wt in a time-resolved experiment.

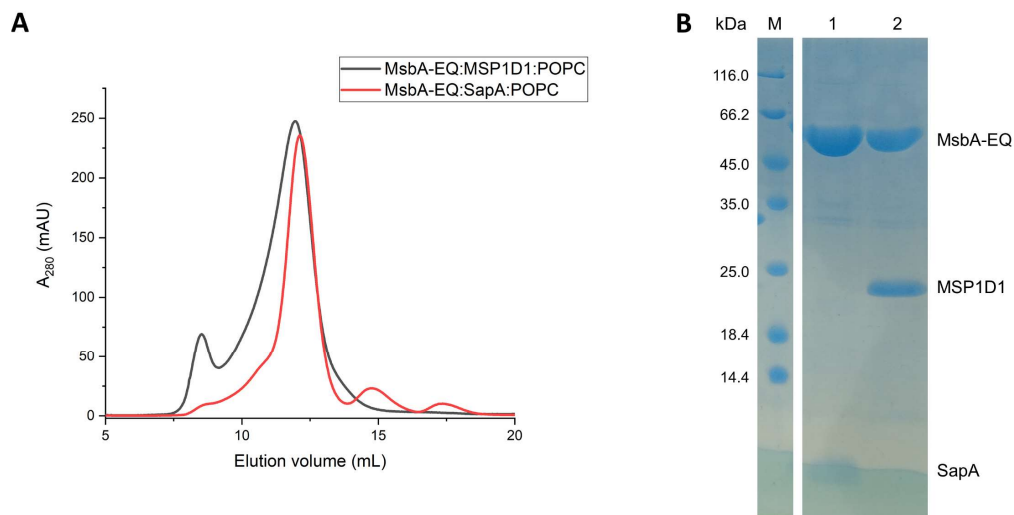


Figure 59: Reconstitution of MsbA-EQ into MSP-based nanodiscs and Salipro. **A:** SEC profiles show the successful assembly of MsbA-EQ in nanodiscs and Salipro at 12 mL elution volume. **B:** SDS-Page of SEC fractions at 12 mL showing the presents of MsbA-EQ and MSP1D1/SapA. M = molecular weight marker, 1 = MsbA-EQ in Salipro with POPC, 2 = MsbA-EQ in nanodiscs with POPC.

First, the MsbA-EQ mutant was incorporated into MSP-based nanodiscs and Salipro with POPC (see Figure 59) and the ATPase activity was compared in a Baginski assay to the wt MsbA in MSP nanodiscs and Salipro (see Figure 60). In nanodiscs, the maximal reaction speed (V_{\max}) with 109 nmol/ATP/min/mg enzyme as well as the Michaelis constant (K_m) with 5622 μM ATP is significantly reduced compared to the wt MsbA incorporated into nanodiscs ($V_{\max} = 669 \pm 38$ nmol/ATP/min/mg enzyme, $K_m = 475 \pm 75$ μM ATP). A similar reduction of the ATPase activity was also observed in the Salipro system. The MsbA-EQ mutant is showing a significantly reduced activity ($V_{\max} = 153$ nmol/ATP/min/mg enzyme, $K_m = 23262$ μM ATP) compared to the wt MsbA in Salipro ($V_{\max} = 601 \pm 45$ nmol/ATP/min/mg enzyme, $K_m = 493$

$\pm 79 \mu\text{M ATP}$). These results confirm the activity reduction of the E506Q point mutation in MsbA. The reduction of reaction speed allows the analysis of the kinetics of the mutant in a time-resolved SAXS experiment where ATP-Mg²⁺ is manually mixed with MsbA-EQ incorporated into nanodiscs and Salipro.

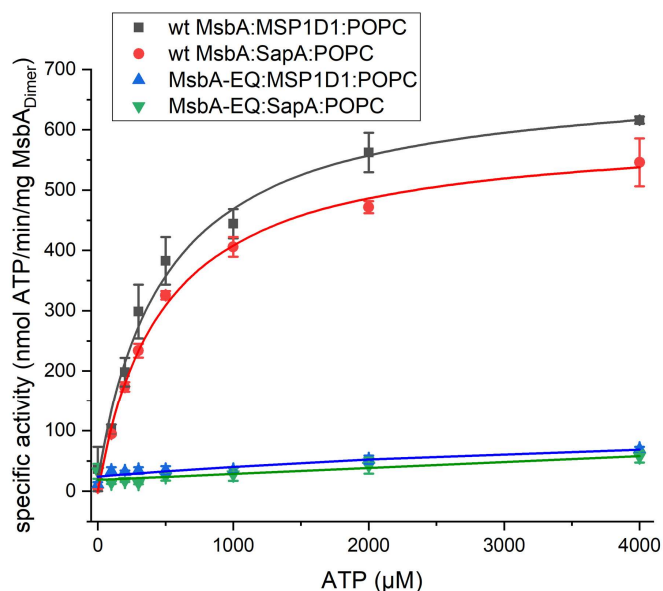


Figure 60: ATPase activity of wt MsbA and MsbA-EQ mutant incorporated into MSP-based nanodiscs and Salipro measured by the Baginski assay. The maximal reaction speed (V_{\max}) of wt MsbA in nanodiscs with POPC is $669 \pm 38 \text{ nmol ATP} \cdot \text{min}^{-1} \cdot \text{mg}^{-1}$ enzyme and the Michaelis (K_m) constant is $475 \pm 75 \mu\text{M ATP}$. At the same time, the MsbA-EQ mutant shows a significant decrease in activity in the same system ($V_{\max} = 109 \text{ nmol/ATP/min/mg enzyme}$, $K_m = 5622 \mu\text{M ATP}$). The same trend is also visible in Salipro (wt MsbA: $V_{\max} = 601 \pm 45 \text{ nmol/ATP/min/mg enzyme}$, $K_m = 493 \pm 79 \mu\text{M ATP}$, MsbA-EQ: $V_{\max} = 153 \text{ nmol/ATP/min/mg enzyme}$, $K_m = 23262 \mu\text{M ATP}$). The experiment was performed at RT in triplicates.

3.3.2.1 Time-resolved SAXS analysis of MsbA-EQ in MSP nanodiscs

In the time-resolved SAXS experiment, $16.5 \mu\text{M}$ of the MsbA-EQ mutant in nanodiscs was mixed with $123.75 \mu\text{M ATP-Mg}^{2+}$ and SAXS data were measured after 5 min, 10 min, 15 min, 20 min, 30 min, 60 min, 105 min, 150 min and 382 min. Additionally, the apo sample was measured before it was mixed with ATP-Mg²⁺. Differences in small-angle scattering are present in the mid q-range between 0.5 nm^{-1} and 1.5 nm^{-1} (see Figure 61), indicating detectable structural differences of the MsbA-EQ nanodisc complex.

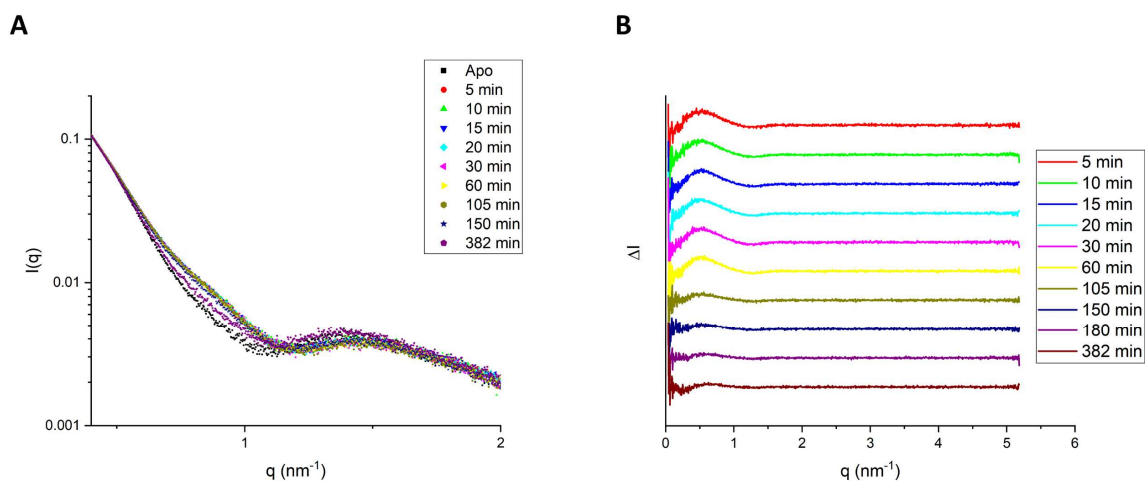


Figure 61: Scattering differences of MsbA-EQ incorporated in MSP-based nanodiscs after mixing with ATP + Mg²⁺ (123.75 μM each). **A:** Scattering data of the time-resolved experiment (zoomed in). **B:** Scattering differences compared to time point zero (0 min). Differences are visible at 0.6 nm⁻¹ and 1.3 nm⁻¹.

Table 12: Structural time-resolved SAXS parameter of MsbA-EQ in nanodiscs with POPC.

Time	R _g (Å)	D _{max} (Å)
Apo	53.7 ± 0.20	190
5 min	52.5 ± 0.16	190
10 min	52.1 ± 0.22	180
15 min	52.8 ± 0.17	185
20 min	52.6 ± 0.18	190
30 min	52.9 ± 0.19	193
60 min	53.2 ± 0.16	190
105 min	54.2 ± 0.17	200
150 min	54.8 ± 0.14	190
180 min	55.5 ± 0.15	191
382 min	57.8 ± 0.19	210

The distance distribution plots of MsbA-EQ in nanodiscs show only minor differences over the first 382 min after mixing with ATP-Mg²⁺ (Figure 62A). After 382 min, there is a slight increase in R_g in the particles. At the same time, the D_{max} is slightly higher at 382 min compared to the time points measured before (Table 12). This could be explained by the possible start of building larger aggregates. The Kratky plot illustrates the change of flexibility of MsbA-EQ in the nanodisc (Figure 62B). Between 5 min and 150 min, the plots have a higher progression compared to the apo plot at 0.9 nm⁻¹, suggesting increased flexibility of the particles. After 382 min, the plot is almost back to the apo level.

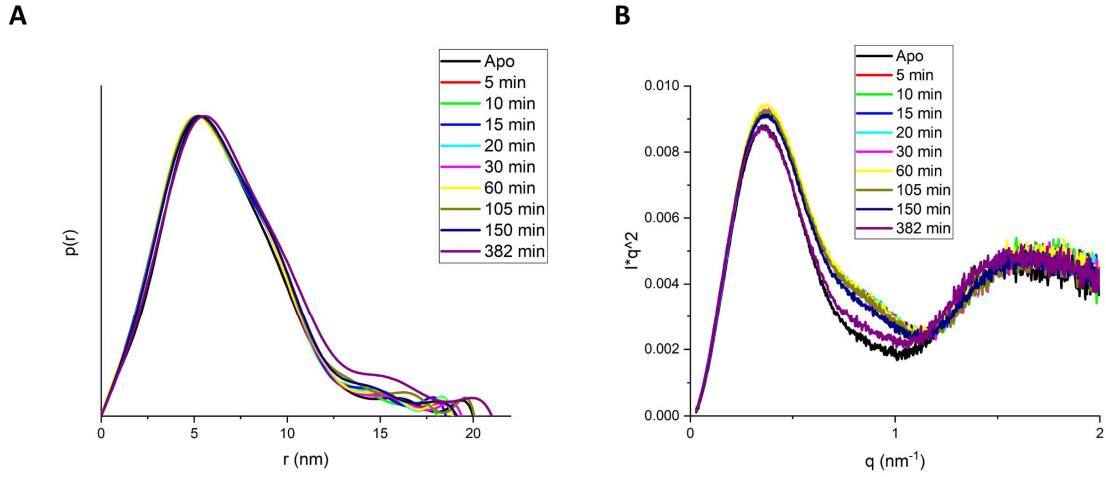


Figure 62: Analysis of time-resolved SAXS data of MsbA-EQ in nanodiscs. **A:** Distance distribution plots over time after mixing with ATP + Mg²⁺ (123.75 mM each). The distance distribution is relatively similar over the first 382 min. **B:** Kratky plot of the data shown in A. Differences of the apo (0 min) and 382 min at $\sim 0.9 \text{ nm}^{-1}$ suggests a less flexible structure of MsbA-EQ.

The evolution of the R_g^2 over the first 382 min of MsbA-EQ in nanodiscs is shown in Figure 63A. The starting R_g^2 of $2884 \pm 49 \text{ \AA}^2$ was measured before mixing MsbA-EQ incorporated in nanodiscs with ATP-Mg²⁺ (123.75 mM). After mixing, the R_g^2 decreases to $2714 \pm 53 \text{ \AA}^2$ after 10 min, which could be the transition from the inward open to the occluded state of MsbA-EQ. Afterwards, the R_g^2 increases almost linear to $3341 \pm 56 \text{ \AA}^2$ after 382 min. The increase of R_g^2 above the R_g^2 of the apo sample could be explained by a potential wider inward open conformation of MsbA-EQ compared to the starting conformation. The scattering intensity at zero angles ($I(0)$) after 382 min is with $0.46 \pm 0.0014 \text{ cm}^{-1}$ only slightly higher compared to the $I(0)$ of the previous measurements (Figure 63B). This slight increase of $I(0)$ is not enough to indicate sample aggregation. The $I(0)$ is a good indicator for identifying aggregates in the measured sample because it reflects the scattering of the smallest q , which corresponds to very large-sized particles. In addition, the $I(0)$ is proportional to the molecular weight of the protein. Where d is the density of the protein in $\text{g} \cdot \text{cm}^{-3}$, ΔSLD the difference of the scattering length density between the sample and the solvent in cm^{-2} and N_A the Avogadro number in mol^{-1} . Equation (5) is only valid if $I(0)$ is in absolute scale and units of cm^{-1} .

$$M_w / \text{g} \cdot \text{mol}^{-1} = \frac{I(0)d^2 N_A}{c \Delta SLD^2} \quad (5)$$

A wide open inward conformation of MsbA was found in crystal structures in combination with detergents¹⁶. The existence of this state in physiological conditions is still discussed. Recently it could be shown that a wide inward open conformation of MsbA is present in *E. coli* cells and cell-derived membranes¹⁶². Due to the increase of R_g^2 our data are indicating a potential existence of an inward open state, which is slightly larger than the apo inward open

state. The calculated R_g of the outward open state (PDB: 3b60¹⁶, $R_g = 36.8 \pm 0.1 \text{ \AA}$) shows a similar value to the occluded state of MsbA (PDB: 7bcw¹³³, $R_g = 36.7 \pm 0.1 \text{ \AA}$), which indicates that the outward open state of MsbA cannot explain the overshoot of the R_g^2 after 105 min. All calculations were performed without the nanodisc in PEPSI¹³⁴.

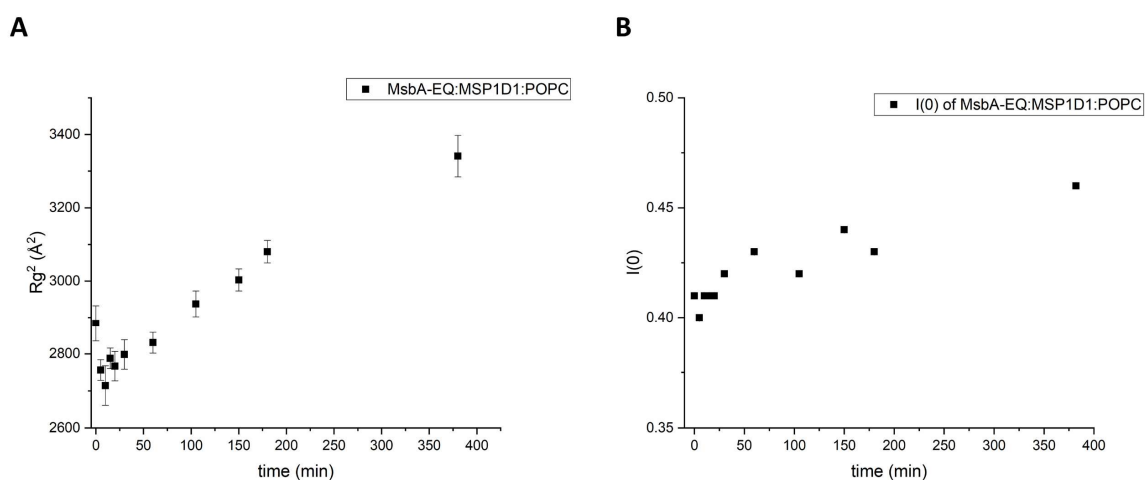


Figure 63: **A:** Evolution of R_g^2 of MsbA-EQ in nanodiscs over time. The R_g^2 decreases in the first 10 min to $2714 \pm 53 \text{ \AA}^2$ and increases in a linear fashion afterwards up to $3341 \pm 56 \text{ \AA}^2$. **B:** Evolution of the scattering intensity at zero angles ($I(0)$). The $I(0)$ over the whole measured 382 min is very similar, indicating that the increase of R_g^2 is not the result of larger aggregates.

The data is well described with three independent components in the singular value decomposition (SVD) analysis of MsbA-EQ in nanodiscs (Figure 64). The first three components are above the non-zero singular values of the diagonal matrix. The fourth basis function of the SVD (Figure 64B, green curve) includes only noise.

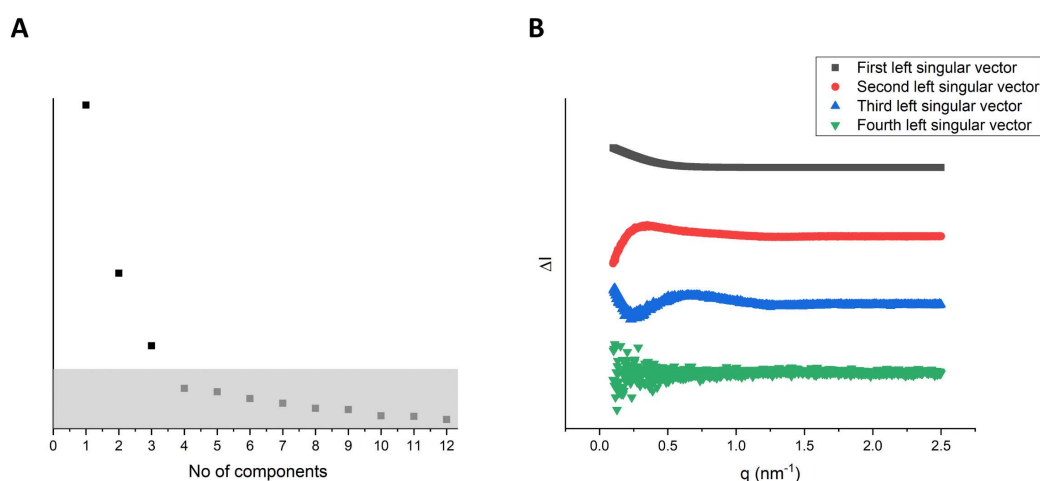


Figure 64: Singular-value decomposition (SVD) analysis of MsbA-EQ in nanodiscs. **A:** Number of independent components based on the non-zero (above the grey area) singular values of the diagonal matrix suggests three major components. **B:** The first four basis functions from the SVD analysis of the difference curves indicate the presence of three independent components in the SAXS data. The fourth basis component (green) corresponds to noise.

These three components contribute to different degrees to the scattering signal over time. The first component (Figure 65, black) is not present before the addition of ATP-Mg²⁺. After mixing, the component contribution increases until a plateau is reached after 60 min. Component 3 (blue) is similar to component 1, not present before adding ATP-Mg²⁺. However, the contribution increase is much faster compared to component 1. Already after 5 min, a plateau is reached, and the contribution stays at a high level until the rest of the time course. In contrast to components 1 and 3, the second component (red) starts with a high level and the contribution decreases until component 2 is not representing the scattering signal from 180 min onwards. Component 1 (black) could be attributed to the outward open state of MsbA-EQ. The faster contributing component 3 (blue) could be the occluded state and component 2 (red) the apo (narrow inward open) state of MsbA-EQ. The apo state of MsbA-EQ is prominent at time point zero (t = 0). By adding ATP-Mg²⁺, the two nucleotide-binding domains dimerize, leading to a transition from the apo state to the occluded state. Afterwards, MsbA is transitioned to the outward open state.

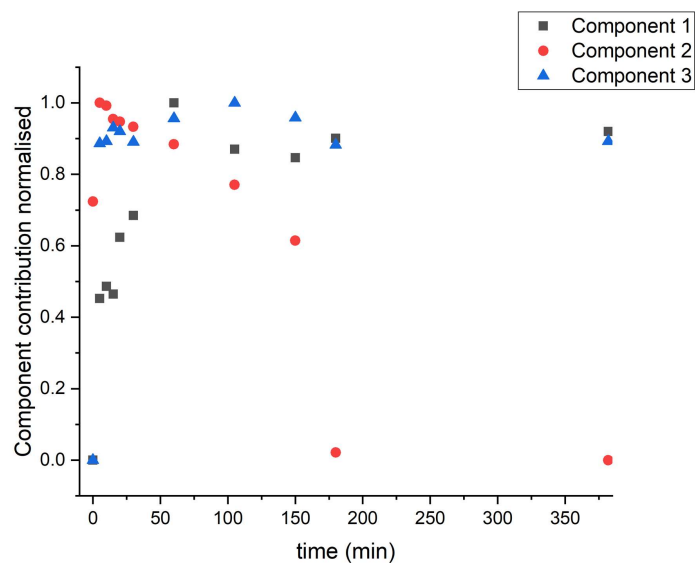


Figure 65: Individual normalised component contribution of the three independent components present in the SVD analysis of MsbA-EQ in nanodiscs. Singular matrix showing the relative amplitudes of the eigenvectors of component 1 (black), component 2 (red) and component 3 (blue) versus time. The contribution of component 1 increases in the first 75 min and stays at a high level until 382 min. The contribution of component 2 is decreasing over time. Component 3 contributed to 0% at time = 0, the contribution increases after 5 min to the maximum and stays at the high level.

It could be shown that the MsbA-EQ mutant in MSP-based nanodiscs can bind ATP molecules and transition to the occluded state very fast based on the fast decrease of R_g^2 . An overshoot of the R_g^2 compared to the starting conformation is also observed with the MsbA-EQ mutant incorporated into MSP-based nanodiscs. This overshoot could also be due to a wider inward open state of MsbA-EQ after the outward open state. The ΔR_g of MsbA-EQ in nanodiscs is

with 4.1 Å significantly higher compared to MsbA in Salipro measured in the stopped-flow experiment ($\Delta R_g = 1 \text{ \AA}$, see section 3.3.1) but still smaller than the wide inward open state of MsbA found in detergents (PDB: 6bl6²⁰, ΔR_g to class 1 of the EM analysis = 10.2 Å). An explanation could be the same funnelling effect of the nanodiscs on the membrane protein as with Salipro in the stopped-flow data. If the R_g^2 would increase more if we measured longer than 382 min is speculative because the exact kinetics of the whole reaction cycle is not known for MsbA-EQ mutant in nanodiscs.

3.3.2.2 Time-resolved SAXS analysis of MsbA-EQ in Salipro

Complimentary to the time-resolved SAXS experiment in batch mode with MsbA-EQ in nanodiscs, a similar experiment of MsbA-EQ in Salipro was performed. 16.5 μM of the MsbA-EQ mutant in Salipro was mixed with 123.75 μM ATP-Mg²⁺ and SAXS data were measured after 5 min, 10 min, 15 min, 20 min, 30 min, 60 min, 105 min, 150 min and 380 min. Before adding ATP-Mg²⁺ to the protein sample, the apo (t = 0) was measured. Figure 66 shows the scattering differences. Differences are visible between 0.6 nm⁻¹ and 1.3 nm⁻¹. These differences reflect conformational changes of MsbA-EQ in Salipro in combination with ATP-Mg²⁺. While the scattering differences compared to the apo state are larger in the early measurements, these differences decrease over time (Figure 66B).

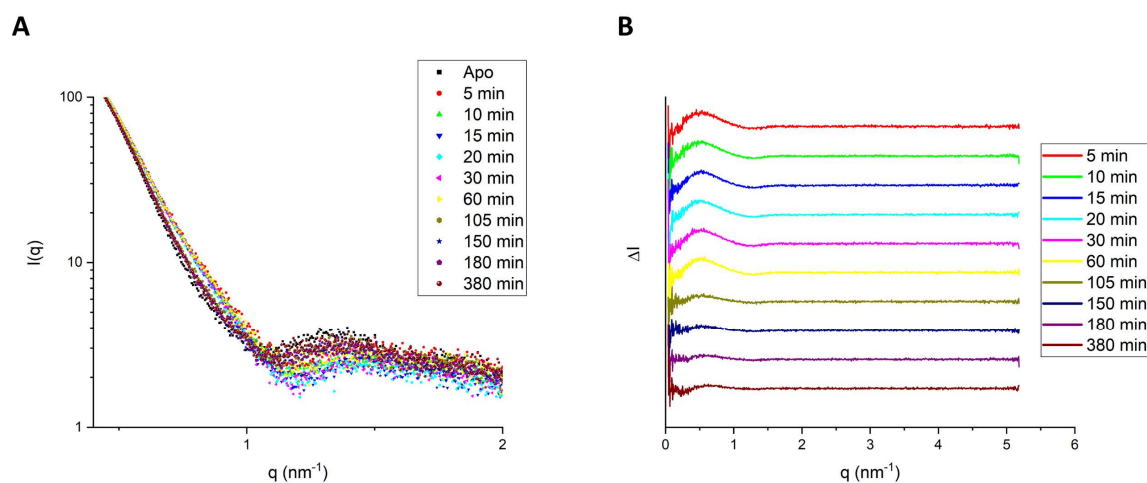
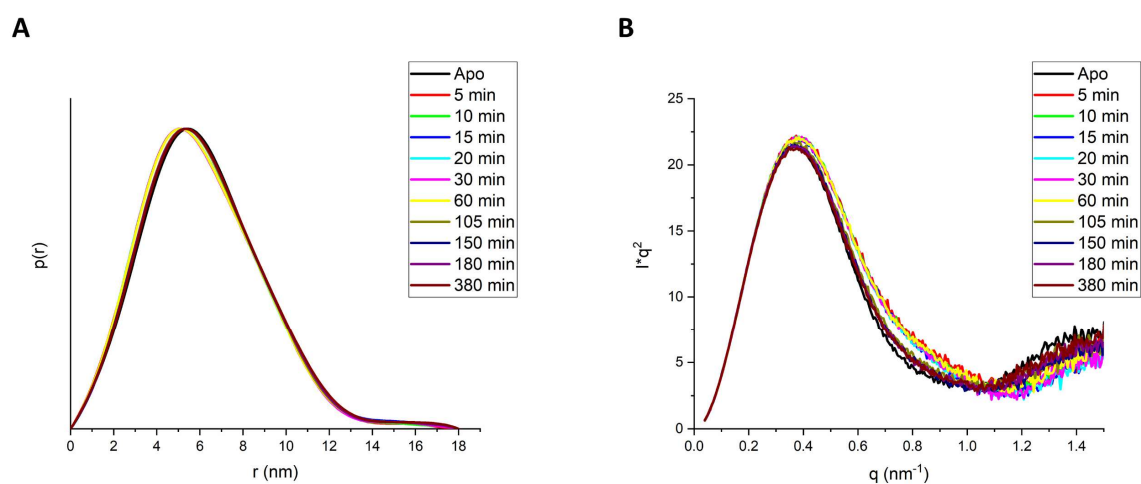


Figure 66: Scattering differences of MsbA-EQ incorporated in Salipro after mixing with ATP-Mg²⁺ (123.75 μM). **A:** Scattering data of the time-resolved experiment (zoomed in). **B:** Scattering differences compared to time point zero (0 min) with differences at 0.6 nm⁻¹ and 1.3 nm⁻¹.

Table 13: Structural time-resolved SAXS parameter of MsbA-EQ in Salipro with POPC.

Time	R_g (Å)	D_{max} (Å)
Apo	47.6 ± 0.10	180
5 min	46.7 ± 0.13	180
10 min	46.7 ± 0.09	180
15 min	47.0 ± 0.10	180
20 min	46.8 ± 0.09	180
30 min	46.8 ± 0.11	180
60 min	46.9 ± 0.10	180
105 min	47.5 ± 0.10	180
150 min	47.7 ± 0.09	180
180 min	47.6 ± 0.08	180
380 min	48.0 ± 0.08	180

The distance distribution plots over the whole duration of measurements (380 min) are almost identical, indicating the scattering differences reflect to internal structural rearrangements (Figure 67A). Also, the D_{max} is constant throughout the measurements with $D_{max} = 180$ Å (Table 13). In addition, the R_g is changing only subtle by decreasing after 5 min from 47.6 ± 0.10 Å to 46.7 ± 0.13 Å followed by an increase up to 48.0 ± 0.08 Å after 380 min. The Kratky plot reveals subtle changes after 5 min in the region between 0.6 nm^{-1} and 1.4 nm^{-1} compared to the apo sample (Figure 67B). The slightly less pronounced peak indicated greater flexibility of the particles. After 105 min, the Kratky plots reached almost the progression of the apo plot.

**Figure 67:** Analysis of time-resolved SAXS data of MsbA-EQ in Salipro. **A:** Distance distribution plots over time after mixing with ATP + Mg^{2+} ($123.75 \mu\text{M}$). The distance distribution is similar over the first 380 min. **B:** Kratky plot of the data shown in A. Differences of the apo (0 min) and 382 min samples compared to the other measurements suggests a less flexible structure.

The evolution of R_g^2 of MsbA-EQ in Salipro (Figure 68A) is very similar to the evolution of MsbA-EQ in nanodiscs (Figure 63A). The apo state (time = 0) has an R_g^2 of $2262 \pm 23 \text{ \AA}^2$ and decreases after 5 min to $2181 \pm 37 \text{ \AA}^2$. Afterwards, the R_g^2 increases and after 105 min, the R_g^2 of the apo state is reached. The R_g^2 increases further until the end of the measurements (380 min) to $2304 \pm 15 \text{ \AA}^2$. The fact that the $I(0)$ is increasing only minimal (below 5%) over time this is an indicator that no aggregates are forming during the experiment (Figure 68B). So, these R_g changes correspond to subtle changes in the MsbA-EQ Salipro complex. The decrease of R_g between the two first measurements after 0 min and 5 min could be the transition from the inward open to the occluded state due to the binding of ATP and dimerization of the two NBDs. A slightly wider inward open state could potentially explain the small overshoot of R_g . The existence of a wider inward open state of MsbA in lipid carrier discs was discussed in section 3.3.1 and 3.3.2.1. However, the overshoot in Salipro with an ΔR_g of 0.4 \AA is significantly lower compared to nanodiscs (ΔR_g of 4.1 \AA). Why the overshoot in nanodiscs is higher compared to Salipro cannot be clearly explained. Potentially the transition of the MsbA-EQ mutant from the outward open to the wider inward open state is significantly slower in Salipro compared to nanodiscs. An experiment with longer measurements would be necessary to confirm this hypothesis.

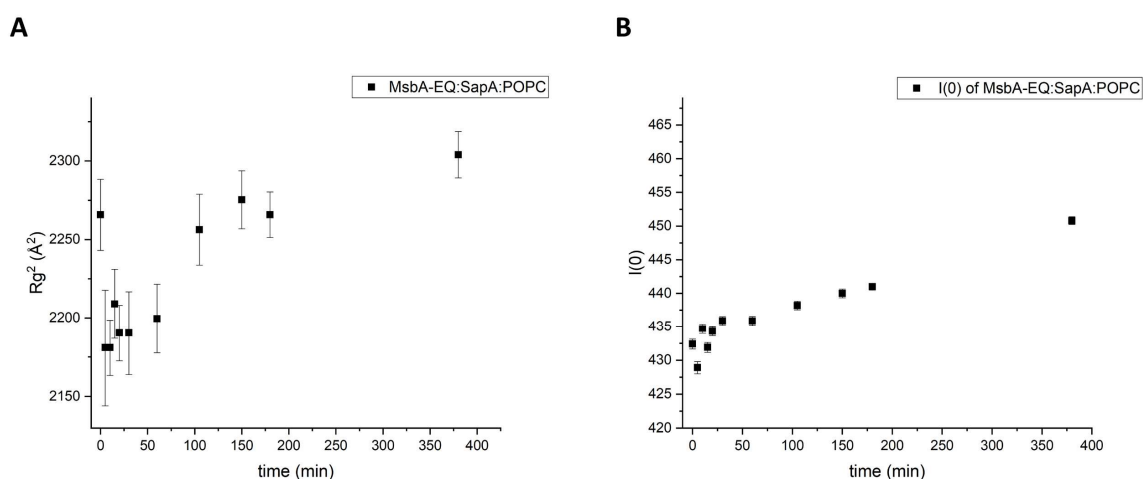


Figure 68: **A:** Evolution of R_g^2 of MsbA-EQ in Salipro over the first 380 min. The R_g^2 decreases in the first 10 min to $2181 \pm 37 \text{ \AA}^2$ and increases afterwards up to $2304 \pm 15 \text{ \AA}^2$. **B:** Evolution of the scattering intensity at zero angles ($I(0)$). The $I(0)$ is very similar during the entire time course. All data points are within 5%.

The SVD analysis of MsbA-EQ shows that the scattering data is well described by two individual components (Figure 69A), which are above the non-zero singular values of the diagonal matrix. The third basis function of SVD analysis corresponds to noise (Figure 69B). In contrast to MsbA-EQ in nanodiscs (Figure 64), the scattering signal is described in only two components. This could also indicate that the transition from the outward open to the wider

inward open state is slower in Salipro and the opening of the wider inward open state is not finished. The wider inward open state is potentially the additional component of MsbA-EQ in nanodiscs. Figure 69B shows the third basis function of the SVD analysis (blue) corresponding to noise. Still, the small features around 0.25 nm^{-1} could be potentially more pronounced with the further opening of the wider inward open state.

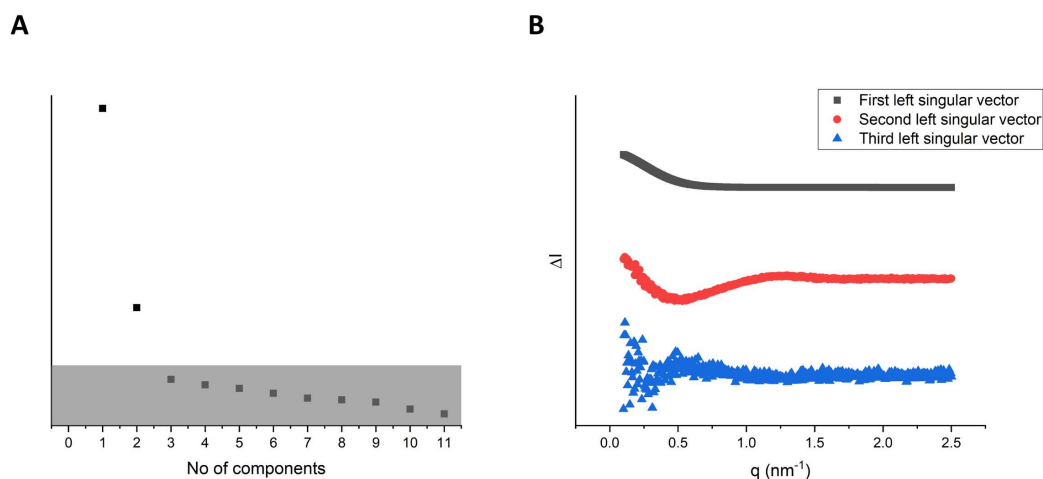


Figure 69: Singular-value decomposition (SVD) analysis of MsbA-EQ in Salipro. **A:** Number of independent components based on the non-zero (above the grey area) singular values of the diagonal matrix suggests that there are two major components. **B:** The first three basis functions from the SVD analysis of the difference curves indicate the presence of two independent components in the TR-SAXS data. The third basis component (blue) corresponds to noise.

The evolution of the two components from the SVD analysis of MsbA-EQ in Salipro is shown in Figure 70. Component 1 is not contributing to the scattering signal at $t = 0$, while component 2 is dominant before the addition of ATP-Mg²⁺. The contribution of component 1 increases until after 380 min the maximum contribution is reached. The contribution of component 2 decreases to 0 in the first 5 min and increases in the following measurements. Component 1 could relate to a mixture of occluded and outward open. Component 2 could correspond to the inward open state of MsbA-EQ. Starting as the dominant conformation, followed by a fast drop due to the rapid transition to the occluded state. After the occluded and outward open state, MsbA-EQ is transitioning back to the inward open state leading to an increase of component 2 from 5 min onwards.

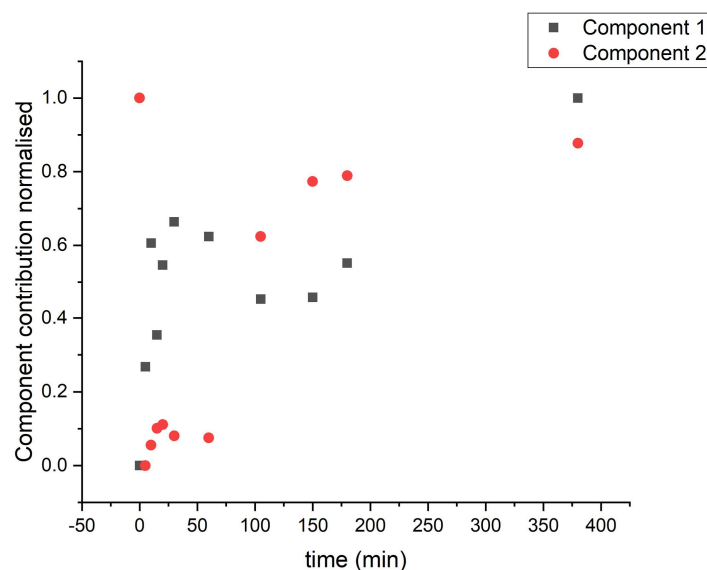


Figure 70: Individual normalised component contribution of the two independent components present in the SVD analysis of MsbA-EQ in Salipro. Singular matrix showing the relative amplitudes of the eigenvectors of component 1 (black) and component 2 (red) versus time. The contribution of component 1 starts at a low level and increases over time. The contribution of component 2 begins at a high level and decreases to 0 after 5 min, followed by an increase during the remaining measurements.

The time-resolved experiment with MsbA-EQ in nanodiscs and Salipro provide insights into the influence of the E506Q mutation in MsbA. The ATP binding is probably not affected. The R_g^2 decreases in both systems in the first 5 min to a minimum. A time-resolved experiment with for example a stop-flow device should be performed to make measurements in smaller time intervals directly after mixing MsbA-EQ with ATP-Mg²⁺. Potentially the hydrolysis speed of ATP of MsbA-EQ is significantly reduced, resulting in low activity in the Baginski assay. Another explanation could be that only the ADP and Pi release is slowed down, resulting in a low activity in the Baginski assay and the overshoot of R_g after 380 min. MsbA-EQ is almost trapped in the wider inward open state due to deficient release of ADP and Pi. The overshoot of R_g compared to the R_g of the starting conformation could also be explained by a wider inward open state similar to the stopped-flow data of wt MsbA in Salipro. This overshoot is significantly higher in nanodiscs compared to Salipro.

A potential outlook to further analyse the kinetics of the whole reaction cycle would be longer measurements after mixing with ATP-Mg²⁺ to achieve more profound insights into how long the R_g^2 will increase (opening of the wide inward open state) in nanodiscs and Salipro and if the R_g is decreasing at some point to reach the R_g of the starting conformation.

Another potential outlook to further improve the native-like lipid environment of MsbA in the Salipro is to reconstitute MsbA with their associating lipids directly in Salipro using the DirectMX¹⁷⁰ assembly approach. With this methodology, it is possible to perform a one-step

reconstitution of membrane proteins from crude cell membranes. During the assembly, the target protein will be incorporated with its lipid environment into Salipro. Without the delipination step during the membrane protein purification, MsbA could remain in the natural lipid composition. In this method, the crude membrane will be destabilised with a mild detergent (for example digitonin) to increase the membrane fluidity at 4 °C. As a result, the rendering lipids and IMPs become more accessible for the following reconstitution step. An excess of the carrier protein SapA is added to allow the reconstitution of all IMPs and their associated lipids into Salipro. After affinity chromatography, the target protein is obtained and can be used for structural studies. This method was successfully applied to human membranes and could potentially be adapted to bacterial membranes. One potential difficulty is the vast amounts of SapA proteins needed to extract all IMPs from the crude membrane. Usually, SapA is the bottleneck in during the assembly. Therefore, a more efficient SapA expression and purification may need to be developed first.

4 References

1. Y. Cao. *Advances in Membrane Proteins*. (Springer Singapore, 2018). doi:10.1007/978-981-13-0532-0_3
2. Liu, J. Comparing function and structure between entire proteomes. *Protein Sci.* **10**, 1970–1979 (2001).
3. Krogh, A., Larsson, È., Heijne, G. Von & Sonnhammer, E. L. L. Predicting Transmembrane Protein Topology with a Hidden Markov Model: Application to Complete Genomes. *J. Mol. Biol.* **305**, 567–580 (2001).
4. Overington, J. P., Al-lazikani, B. & Hopkins, A. L. How many drug targets are there? *Nat. Rev. Drug Discov.* **5**, 993–996 (2006).
5. Wardhan, R. & Mudgal, P. *Textbook of Membrane Biology*. (Springer Singapore, 2017).
6. Wallin, E. & Heijne, G. Von. Genome-wide analysis of integral membrane proteins from eubacterial, archaean, and eukaryotic organisms. *Protein Sci.* **7**, 1029–1038 (2008).
7. Moraes, I., Evans, G., Sanchez-Weatherby, J., Newstead, S. & Stewart, P. D. The Next Generation in Membrane Protein Structure Determination. in *Springer International Publishing* (2017). doi:10.1007/978-3-319-35072-1_13
8. Linke, D. *Detergents. An Overview. Methods in Enzymology* **463**, (Elsevier Inc., 2009).
9. Seddon, A. M., Curnow, P. & Booth, P. J. Membrane proteins , lipids and detergents : not just a soap opera. *Biochim. Biophys. Acta* **1666**, 105–117 (2004).
10. Champeil, P. *et al.* A robust method to screen detergents for membrane protein stabilization, revisited. *Anal. Biochem.* **511**, 31–35 (2016).
11. Locher, K. P. Mechanistic diversity in ATP-binding cassette (ABC) transporters. *Nat. Struct. Mol. Biol.* **23**, 487–493 (2016).
12. Wilkens, S. Structure and mechanism of ABC transporters. *F1000Prime Rep.* **7**, 1–9 (2015).
13. Doerrler, W. T., Gibbons, H. S. & Raetz, C. R. H. MsbA-dependent Translocation of Lipids across the Inner Membrane of Escherichia coli *. *J. Biol. Chem.* **279**, 45102–45109 (2004).
14. Zhou, Z., White, K. A., Polissi, A., Georgopoulos, C. & Raetz, C. R. H. Function of

- Escherichia coli MsbA, an Essential ABC Family Transporter, in Lipid A and Phospholipid Biosynthesis *. *J. Biol. Chem.* **273**, 12466–12475 (1998).
15. Raetz, C. R. H., Reynolds, C. M., Trent, M. S. & Bishop, R. E. Lipid A Modification Systems in Gram-Negative Bacteria. *Annu. Rev. Biochem.* **76**, 295–329 (2007).
 16. Ward, A., Reyes, C. L., Yu, J., Roth, C. B. & Chang, G. Flexibility in the ABC transporter MsbA : Alternating access with a twist. *Proc Natl Acad Sci USA* **104**, 19005–19010 (2007).
 17. Mi, W. *et al.* Structural basis of MsbA-mediated lipopolysaccharide transport. *Nature* **549**, 233–237 (2017).
 18. Terakado, K., Nakano, H., Kimura, Y., Nakatsu, T. & Kato, H. Deleting two C-terminal α -helices is effective to crystallize the bacterial ABC transporter Escherichia coli MsbA complexed with AMP-PNP. *Acta Crystallogr D Biol Crystallogr* **66**, 319–323 (2010).
 19. Ho, H. *et al.* Structural basis for dual-mode inhibition of the ABC transporter MsbA. *Nature* **557**, 196–201 (2018).
 20. Padayatti, P. S. *et al.* Structural Insights into the Lipid A Transport Pathway in MsbA. *Structure* **27**, 1114-1123.e3 (2019).
 21. Kehlenbeck, D., Josts, I., Nitsche, J. & Busch, S. Comparison of lipidic carrier systems for integral membrane proteins – MsbA as case study. *Biol. Chem.* **400**, 1509–1518 (2019).
 22. Bayburt, T. H., Leitz, A. J., Xie, G., Oprian, D. D. & Sligar, S. G. Transducin activation by nanoscale lipid bilayers containing one and two rhodopsins. *J. Biol. Chem.* **282**, 14875–14881 (2007).
 23. Shih, A. Y., Denisov, I. G., Phillips, J. C., Sugar, S. G. & Schulten, K. Molecular dynamics simulations of discoidal bilayers assembled from truncated human lipoproteins. *Biophys. J.* **88**, 548–556 (2005).
 24. Ritchie, T. K. *et al.* Chapter 11 Reconstitution of Membrane Proteins in Phospholipid Bilayer Nanodiscs. *Methods Enzymol.* **464**, 211–231 (2009).
 25. Bayburt, T. H. & Sligar, S. G. Self-assembly of single integral membrane proteins into soluble nanoscale phospholipid bilayers. *Protein Sci.* **12**, 2476–2481 (2009).

26. Denisov, I. G., Grinkova, Y. V., Lazarides, A. A. & Sligar, S. G. Directed Self-Assembly of Monodisperse Phospholipid Bilayer Nanodiscs with Controlled Size. *J. Am. Chem. Soc.* **126**, 3477–3487 (2004).
27. Bruhn, H. A short guided tour through functional and structural features of saposin-like proteins. *Biochem. J.* **389**, 249–257 (2005).
28. Olmeda, B., García-Álvarez, B. & Pérez-Gil, J. Structure-function correlations of pulmonary surfactant protein SP-B and the saposin-like family of proteins. *Eur. Biophys. J.* **42**, 209–222 (2013).
29. Frauenfeld, J. *et al.* A saposin-lipoprotein nanoparticle system for membrane proteins. *Nat. Methods* **13**, 345–351 (2016).
30. Flayhan, A. *et al.* Saposin Lipid Nanoparticles: A Highly Versatile and Modular Tool for Membrane Protein Research. *Structure* **26**, 345-355.e5 (2018).
31. Carpenter, E. P., Beis, K., Cameron, A. D. & Iwata, S. Overcoming the challenges of membrane protein crystallography. *Curr. Opin. Struct. Biol.* **18**, 581–586
32. Newstead, S. *et al.* Insights into outer membrane protein crystallization. *Mol. Membr. Biol.* **7688**, 631–638 (2008).
33. Ferrandon, B. & Newstead, S. Rationalizing a α -helical membrane protein crystallization. *Protein Sci.* **1**, 466–472 (2008).
34. Newby, Z. E. R. *et al.* PROTOCOL A general protocol for the crystallization of membrane proteins for X-ray structural investigation. *Nat. Protoc.* **4**, 619–637 (2009).
35. Bill, R. M. *et al.* perspective Overcoming barriers to membrane protein structure determination. *Nat. Biotechnol.* **29**, 335–340 (2011).
36. Biology, C., Kang, H. J., Lee, C. & Drew, D. The International Journal of Biochemistry Breaking the barriers in membrane protein crystallography. *Int. J. Biochem. Cell Biol.* **45**, 636–644 (2013).
37. Kobilka, B. & Schertler, G. F. X. New G-protein-coupled receptor crystal structures : insights and limitations. *Trends Pharmacol. Sci.* **29**, 79–83 (2008).
38. Roth, B. L. Studies of a ubiquitous receptor family. *Nature* **492**, 57 (2012).
39. Pedersen, B. P., Buch-pedersen, M. J., Morth, J. P., Palmgren, M. G. & Nissen, P.

- Crystal structure of the plasma membrane proton pump. *Nature* **450**, 1111–1115 (2007).
40. Morth, J. P. *et al.* Crystal structure of the sodium – potassium pump. *Nature* **450**, 1043–1050 (2007).
 41. Morth, J. P. *et al.* REVIEWS A structural overview of the plasma membrane Na⁺, K⁺-ATPase and H⁺-ATPase ion pumps. *Nat. Publ. Gr.* **12**, (2011).
 42. Bhattacharya, A. Structures of desire. *Nature* **459**, 24–27 (2009).
 43. Baker, M. Making membrane proteins for structures : a trillion tiny tweaks. *Nat. Publ. Gr.* **7**, 429–434 (2010).
 44. Sanders, C. R. & Frank, S. Solution NMR of membrane proteins : practice. *Magn. Reson. Chem.* **44**, S24–S40 (2006).
 45. Hong, M., Zhang, Y. & Hu, F. Membrane Protein Structure and Dynamics from NMR Spectroscopy. *Annu. Rev. Phys. Chem.* **63**, 1–24 (2012).
 46. Opella, S. J. Structure Determination of Membrane Proteins by Nuclear Magnetic Resonance Spectroscopy. *Annu. Rev. Anal. Chem.* **6**, 305–328 (2013).
 47. Jacques, D. A. & Trewthella, J. Small-angle scattering for structural biology — Expanding the frontier while avoiding the pitfalls. *Protein Sci.* **19**, 642–657 (2010).
 48. Petoukhov, M. V & Svergun, D. I. Applications of small-angle X-ray scattering to biomacromolecular solutions. *Int. J. Biochem. Cell Biol.* **45**, 429–437 (2013).
 49. Blanchet, C. E. & Svergun, D. I. Small-Angle X-Ray Scattering on Biological Macromolecules and Nanocomposites in Solution. *Annu. Rev. Phys. Chem.* **64**, 37–54 (2013).
 50. Rambo, R. P. & Tainer, J. A. Super-Resolution in Solution X-Ray Scattering and Its Applications to Structural Systems Biology. *Annu. Rev. Biophys.* **42**, 415–441 (2013).
 51. Hura, G. L. *et al.* Robust , high-throughput solution structural analyses by small angle X-ray scattering (SAXS). *Nat. Methods* **6**, 606–612 (2009).
 52. Blanchet, C. E. *et al.* Versatile sample environments and automation for biological solution X-ray scattering experiments at the P12 beamline (PETRA III, DESY). *J. Appl. Crystallogr.* **48**, 431–443 (2015).
 53. Toft, K. N. *et al.* High-Throughput Small Angle X-ray Scattering from Proteins in

- Solution Using a Microfluidic Front-End. *Anal. Chem.* **80**, 3648–3654 (2008).
54. Schroer, M. A. *et al.* Smaller capillaries improve the small-angle X-ray scattering signal and sample consumption for biomacromolecular solutions research papers. *J. Synchrotron Radiat.* **25**, 1113–1122 (2018).
 55. Zimmer, J., Doyle, D. A. & Gu, J. Structural Characterization and pH-Induced Conformational Transition of Full-Length KcsA. *Biophys. J.* **90**, 1752–1766 (2006).
 56. Johs, A. *et al.* Modular Structure of Solubilized Human Apolipoprotein B-100. *J. Biol. Chem.* **281**, 19732–19739 (2006).
 57. Cardoso, M. B., Smolensky, D., Heller, W. T. & Neill, H. O. Insight into the Structure of Light-Harvesting Complex II and Its Stabilization in Detergent Solution. *J. Phys. Chem.* **113**, 16377–16383 (2009).
 58. Tang, K., Urban, V. S., Wen, J., Xin, Y. & Blankenship, R. E. SANS Investigation of the Photosynthetic Machinery of *Chloroflexus aurantiacus*. *Biophys. J.* **99**, 2398–2407 (2010).
 59. Nogales, A., García, C., Pe, J., Callow, P. & Ezquerra, T. A. Three-dimensional Model of Human Platelet Integrin $\alpha\text{IIb}\beta\text{3}$ in Solution Obtained by Small Angle Neutron Scattering. *J. Biol. Chem.* **285**, 1023–1031 (2010).
 60. Compton, E. L. R., Karinou, E., Naismith, J. H., Gabel, F. & Javelle, A. Low Resolution Structure of a Bacterial SLC26 Transporter Reveals Dimeric Stoichiometry and Mobile Intracellular. *J. Biol. Chem.* **286**, 27058–27067 (2011).
 61. Wu, Z. *et al.* Double Superhelix Model of High Density Lipoprotein. *J. Biol. Chem.* **284**, 36605–36619 (2009).
 62. Clifton, L. A. *et al.* Low Resolution Structure and Dynamics of a Colicin-Receptor Complex Determined by Neutron Scattering. *J. Biol. Chem.* **287**, 337–346 (2012).
 63. Berthaud, A., Manzi, J. & Pe, J. Modeling Detergent Organization around Aquaporin-0 Using Small- Angle X-ray Scattering. *J. Am. Chem. Soc.* **134**, 10080–10088 (2012).
 64. Skar-Gislinge, N. *et al.* Small-angle scattering determination of the shape and localization of human cytochrome P450 embedded in a phospholipid nanodisc environment research papers. *Acta Cryst.* **D71**, 2412–2421 (2015).

65. Skar-Gislinge, N. & Arleth, L. Small-angle scattering from phospholipid nanodiscs : derivation and refinement of a molecular constrained analytical model form factor. *Phys. Chem. Chem. Phys* **13**, 3161–3170 (2011).
66. Kynde, S. A. R. *et al.* Small-angle scattering gives direct structural information about a membrane protein inside a lipid environment research papers. *Acta Cryst.* **D70**, 371–383 (2014).
67. Cleveland, T. E. *et al.* Small-angle X-ray and neutron scattering demonstrates that cell-free expression produces properly formed disc-shaped nanolipoprotein particles. *Protein Sci.* **27**, 780–789 (2017).
68. Josts, I. *et al.* Structural Kinetics of MsbA Investigated by Stopped-Flow Time-Resolved Small-Angle X-Ray Scattering. *Structure* **28**, 348-354.e3 (2020).
69. Franke, D., Kikhney, A. G., Svergun, D. I. & Back-, T. Nuclear Instruments and Methods in Physics Research A Automated acquisition and analysis of small angle X-ray scattering data. *Nucl. Inst. Methods Phys. Res. A* **689**, 52–59 (2012).
70. Jacrot, B. The study of biological structures by neutron scattering from solution scattering from solution. *Rep. Prog. Phys.* **39**, 911 (1976).
71. Guinier, A. & Fournet, G. SCATTERING OF X-RAYS. *Wiley* (1955).
72. Svergun, D. I. & Koch, M. H. J. Small-angle scattering studies of biological macromolecules in solution. *Reports Prog. Phys.* **66**, 1735–1782 (2003).
73. Guinier, A. The diffusion of x-rays under the extremely weak angles applied to the study of fine particles and colloidal suspension. *Cr Hebd Acad Sci* **206**, 1374–1376 (1938).
74. Engelman, D. M. & Moore, P. B. Determination of quaternary structure by small angle neutron scattering. *Annu. Rev. Biophys. Bioeng.* **4**, 219–241 (1975).
75. Sears, V. F. Neutron scattering lengths and cross sections. *Neutron News* **3**, 26–37 (1992).
76. Jacrot, B. & Zaccari, G. Determination of Molecular Weight by Neutron Scattering. *Biopolymers* **20**, 2413–2426 (1981).
77. Jeffries, C. M. *et al.* Preparing monodisperse macromolecular samples for successful biological small-Angle X-ray and neutron-scattering experiments. *Nat. Protoc.* **11**,

- 2122–2153 (2016).
78. Dunne, O. *et al.* Matchout deuterium labelling of proteins for small-angle neutron scattering studies using prokaryotic and eukaryotic expression systems and high cell-density cultures. *Eur. Biophys. J.* **46**, 425–432 (2017).
 79. Josts, I. *et al.* Conformational States of ABC Transporter MsbA in a Lipid Environment Investigated by Small-Angle Scattering Using Stealth Carrier Nanodiscs. *Structure* **26**, 1072–1079 (2018).
 80. Maric, S. *et al.* Stealth carriers for low-resolution structure determination of membrane proteins in solution. *Acta Crystallogr. Sect. D Biol. Crystallogr.* **70**, 317–328 (2014).
 81. Maric, S. *et al.* Biosynthetic preparation of selectively deuterated phosphatidylcholine in genetically modified *Escherichia coli*. *Appl. Microbiol. Biotechnol.* **99**, 241–254 (2014).
 82. Jones, N. Atomic Secrets. *Nature* **505**, 602–603 (2014).
 83. Frank, J. Averaging of low exposure electron micrographs of non-periodic objects. *Ultramicroscopy* **1**, 159–162 (1975).
 84. Dubochet, J. *et al.* Cryo-electron microscopy of vitrified specimens. *Rev. Biophys.* **21**, 129–228 (1988).
 85. Orlova, E. V. & Saibil, H. R. Structure determination of macromolecular assemblies by single-particle analysis of cryo-electron micrographs. *Current Opinion in Structural Biology* **14**, 584–590 (2004).
 86. Cheng, Y. Single-particle Cryo-EM at crystallographic resolution. *Cell* **161**, 450–457 (2015).
 87. Saibil, H. R. Macromolecular structure determination by cryo-electron microscopy. *Acta Crystallogr. Sect. D Biol. Crystallogr.* **56**, 1215–1222 (2000).
 88. Frank, J. *Three-Dimensional Electron Microscopy of Macromolecular Assemblies: Visualization of Biological Molecules in Their Native State*. Oxford University Press (Oxford University Press, 2006).
 89. Reimer, L. & Kohl, H. *Transmission Electron Microscopy Physics of Image Formation*. Springer series in optical sciences **51**, (2008).

90. Williams, D. B. & Carter, C. B. *Transmission electron microscopy: A textbook for materials science. Transmission Electron Microscopy: A Textbook for Materials Science* (Springer US, 2009).
91. McMullan, G., Faruqi, A. R., Clare, D. & Henderson, R. Ultramicroscopy Comparison of optimal performance at 300 keV of three direct electron detectors for use in low dose electron microscopy. *Ultramicroscopy* **147**, 156–163 (2014).
92. Bai, X., Fernandez, I. S., McMullan, G. & Scheres, S. H. W. Ribosome structures to near-atomic resolution from thirty thousand cryo-EM particles. *Elife* **2**, 2–13 (2013).
93. Campbell, M. G. *et al.* Movies of Ice-Embedded Particles Enhance Resolution in Electron Cryo-Microscopy. *Cell* **20**, 1823–1828 (2012).
94. Li, X. *et al.* Electron counting and beam-induced motion correction enable near-atomic-resolution single-particle cryo-EM. *Nat. Methods* **10**, 584–590 (2013).
95. Brilot, A. F. *et al.* Beam-induced motion of vitrified specimen on holey carbon film. *J. Struct. Biol.* **177**, 630–637 (2012).
96. Grant, T., Rohou, A. & Grigorieff, N. cisTEM, user-friendly software for single-particle image processing. *Elife* **7**, 1–24 (2018).
97. Scheres, S. H. W. RELION: Implementation of a Bayesian approach to cryo-EM structure determination. *J. Struct. Biol.* **180**, 519–530 (2012).
98. Punjani, A., Rubinstein, J. L., Fleet, D. J. & Brubaker, M. A. cryoSPARC: algorithms for rapid unsupervised cryo-EM structure determination. *Nat. Methods* **14**, 290–296 (2017).
99. Tegunov, D. & Cramer, P. Real-time cryo-EM data pre-processing with Warp. *bioRxiv* (2018).
100. Suloway, C. *et al.* Automated molecular microscopy: The new Legimon system. *J. Struct. Biol.* **151**, 41–60 (2005).
101. Mastronarde, D. N. Automated electron microscope tomography using robust prediction of specimen movements. *J. Struct. Biol.* **152**, 36–51 (2005).
102. Kühlbrandt, W. The Resolution Revolution. *Science (80-.)*. **343**, 1443–1444 (2014).
103. Yip, K. M., Fischer, N., Paknia, E., Chari, A. & Stark, H. Atomic-resolution protein

- structure determination by cryo-EM. *Nature* **587**, 157–161 (2020).
104. Liao, M., Cao, E., Julius, D. & Cheng, Y. Structure of the TRPV1 ion channel determined by electron cryo-microscopy. *Nature* **504**, 107–112 (2013).
 105. Wu, M., Gu, J., Guo, R., Huang, Y. & Yang, M. Structure of Mammalian Respiratory Supercomplex Article Structure of Mammalian Respiratory. *Cell* **167**, 1598–1609 (2016).
 106. Kim, J. *et al.* Subnanometre-resolution electron cryomicroscopy structure of a heterodimeric ABC exporter. *Nature* **517**, 396–400 (2015).
 107. Lyumkis, D. Challenges and opportunities in cryo-EM single-particle analysis. *J. Biol. Chem.* **294**, 5181–5197 (2019).
 108. Ohi, M., Li, Y., Cheng, Y. & Walz, T. Negative Staining and Image Classification – Powerful Tools in Modern Electron Microscopy. *Biol. Proced. Online* **6**, 23–34 (2004).
 109. Harris, J. R. & Carlo, S. De. *Negative Staining and Cryo-negative Staining : Applications in Biology and Medicine.* **1117**, (2013).
 110. Wagenknecht, T. *et al.* Three-dimensional reconstruction of the Ribosome from Escherichia coli. *Biophys. J.* **55**, 455–464 (1989).
 111. Dubochet, J. & McDowell, A. . W. Vitrification of pure water for electron microscopy. *J. Microsc.* **124**, 3–4 (1981).
 112. Dubochet, J., Lepault, J., Freeman, R., Berriman, J. & Homo, J. Electron microscopy of frozen water and aqueous solutions. *J. Microsc.* **128**, 219–237 (1982).
 113. Adrian, M., Dubochet, J., Lepault, J. & McDowell, A. W. Cryo-electron microscopy of viruses. *Nature* **308**, 32–36 (1984).
 114. Bellare, J. R., Davis, H. T., Scriven, L. E. & Talmon, Y. Controlled Environment Vitrification System : An Improved Sample Preparation Technique. *J. Electron Microsc. Tech.* **10**, 87–111 (1988).
 115. Tan, Y. Z. *et al.* Addressing preferred specimen orientation in through tilting. *Nat. Methods* **14**, 793–796 (2017).
 116. Henderson, R. The potential and limitations of neutrons , electrons and X-rays for atomic resolution microscopy of unstained biological molecules. *Q. Rev. Biophys.* **28**, 171–193

- (1995).
117. Egerton, R. F. Choice of operating voltage for a transmission electron microscope. *Ultramicroscopy* **145**, 85–93 (2014).
 118. Voss, N. R., Potter, C. S., Smith, R. & Carragher, B. *Software Tools for Molecular Microscopy : An Open-Text Wikibook. Methods Enzymol.* **482**, (Elsevier Inc., 2010).
 119. Zheng, S. Q., E. Palovcak, J. P. Armache, K. A. Verba, Y. C. and D. A. A. MotionCor2 : anisotropic correction of beam-induced motion for improved cryo-electron microscopy. *Nat. Methods* **14**, 331–332 (2017).
 120. Doerr, A. Single-particle cryo-electron microscopy. *Nat. Methods* **13**, 23 (2016).
 121. Henderson, R. Avoiding the pitfalls of single particle cryo-electron microscopy : Einstein from noise. *Proc. Natl. Acad. Sci. U.S.A.* **110**, 18037–18041 (2013).
 122. van Heel, M. Finding trimeric HIV-1 envelope glycoproteins in random noise. *Proc. Natl. Acad. Sci. U.S.A.* **110**, 4175–4177 (2013).
 123. Subramaniam, S. Structure of trimeric HIV-1 envelope glycoproteins. *Proc. Natl. Acad. Sci. U.S.A.* **110**, 4172–4174 (2013).
 124. Harauz, G. & van Heel, M. Exact filters for general geometry three-dimensional reconstruction. *Optik (Stuttg).* **78**, 146–156 (1986).
 125. Saxton, W. O. & Baumeister, N. W. The correlation averaging of a regularly arranged bacterial cell envelope protein. *J. Microsc.* **127**, 127–138 (1982).
 126. Rosenthal, P. B. & Henderson, R. Optimal Determination of Particle Orientation , Absolute Hand , and Contrast Loss in Single-particle Electron Cryomicroscopy. *J. Mol. Biol.* **333**, 721–745 (2003).
 127. Josts, I., Tidow, H. & Monteiro, D. Photocage-initiated time-resolved solution X-ray scattering investigation of protein dimerization. *IUCrJ* **5**, 667–672 (2018).
 128. Artero, J. B., Härtlein, M., McSweeney, S. & Timmins, P. A comparison of refined X-ray structures of hydrogenated and perdeuterated rat γ E-crystallin in H₂O and D₂O. *Acta Crystallogr. Sect. D Biol. Crystallogr.* **61**, 1541–1549 (2005).
 129. White, T., Bursten, S., Federighi, D., Lewis, R. A. & Nudelman, E. High-resolution separation and quantification of neutral lipid and phospholipid species in mammalian

- cells and sera by multi-one-dimensional thin-layer chromatography. *Anal. Biochem.* **258**, (1998).
130. Lindner, P. & Schweins, R. The D11 small-angle scattering instrument: A new benchmark for SANS. *Neutron News* **21**, 15–18 (2010).
 131. Svergun, D. I. Determination of the regularization parameter in indirect-transform methods using perceptual criteria. *J. Appl. Crystallogr.* **25**, 495–503 (1992).
 132. Konarev, P. V., Volkov, V. V., Sokolova, A. V., Koch, M. H. J. & Svergun, D. I. PRIMUS: A Windows PC-based system for small-angle scattering data analysis. *J. Appl. Crystallogr.* **36**, 1277–1282 (2003).
 133. Kehlenbeck, D. *et al.* Cryo-EM structure of MsbA in saposin-lipid nanoparticles (Salipro) provides insights into nucleotide coordination. *FEBS J.* 1–12 (2021). doi:10.1111/febs.16327
 134. Grudin, S., Garkavenko, M. & Kazennov, A. Pepsi-SAXS: An adaptive method for rapid and accurate computation of small-angle X-ray scattering profiles. *Acta Crystallogr. Sect. D Struct. Biol.* **73**, 449–464 (2017).
 135. Grant, T. D. Ab initio electron density determination directly from solution scattering data. *Nat. Methods* **15**, 191–193 (2018).
 136. Franke, D., Jeffries, C. M. & Svergun, D. I. Correlation Map, a goodness-of-fit test for one-dimensional X-ray scattering spectra. *Nat. Methods* **12**, 419–422 (2015).
 137. Kandiah, E. *et al.* CM01: a facility for cryo-electron microscopy at the European Synchrotron. *Acta Crystallogr D Struct Biol* **75**, 528–535 (2019).
 138. Maluenda, D., T. Majtner, P. Horvath, J. L. Vilas, A. Jimenez-Moreno, J. Mota, E. Ramirez-Aportela, R. Sanchez-Garcia, P. Conesa, L. Del Cano, Y. Rancel, Y. Fonseca, M. Martinez, G. Sharov, C. A. Garcia, D. Strelak, R. Melero, R. Marabini, J. M. C. and C. O. S. S. Flexible workflows for on-the-fly electron-microscopy single-particle image processing using Scipion. *Acta Crystallogr D Struct Biol* **75**, 882–894 (2019).
 139. Zhang, K. Gctf: Real-time CTF determination and correction. *J. Struct. Biol.* **193**, 1–12 (2016).
 140. Wagner, T. *et al.* SPHIRE-crYOLO is a fast and accurate fully automated particle picker for cryo-EM. *Commun Biol* **2**, 1–13 (2019).

141. Zivanov, J., T. Nakane, B. O. Forsberg, D. Kimanius, W. J. Hagen, E. L. and S. H. S. New tools for automated high-resolution cryo-EM structure determination in. *Elife* **7**, 1–22 (2018).
142. Rosa-trevín, J. M. De *et al.* Scipion: A software framework toward integration, reproducibility and validation in 3D electron microscopy. *Struct Biol* **195**, 93–99 (2016).
143. Pettersen, E. F. *et al.* UCSF ChimeraX: Structure visualization for researchers, educators, and developers. *Protein Sci* **8**, 70–82 (2021).
144. Emsley, P. & Lohkamp, B. research papers Features and development of Coot research papers. *Acta Crystallogr D Biol Crystallogr* **66**, 486–501 (2010).
145. Croll, T. I. ISOLDE: a physically realistic environment for model building into low-resolution electron-density maps research papers. *Acta Crystallogr D Struct Biol* **74**, 519–530 (2018).
146. Dorothee Liebschner, Pavel V. Afonine, Matthew L. Baker, Gábor Bunkóczi, Vincent B. Chen, Tristan I. Croll, Bradley Hintze, Li-Wei Hung, Swati Jain, Airlie J. McCoy, Nigel W. Moriarty, Robert D. Oeffner, Billy K. Poon, Michael G. Prisant, Oleg V. Sobolev, C. J. W. and P. D. A. Macromolecular structure determination using X-rays, neutrons and electrons: recent developments in Phenix. *Acta Crystallogr D Struct Biol* **75**, 861–877 (2019).
147. Afonine, P. V. *et al.* New tools for the analysis and validation of cryo-EM maps and atomic models. *Acta Crystallogr. Sect. D Struct. Biol.* **74**, 814–840 (2018).
148. Afonine, P. V. *et al.* Real-space refinement in PHENIX for cryo-EM and crystallography. *Acta Crystallogr. Sect. D Struct. Biol.* **74**, 531–544 (2018).
149. Baginski, E. S. & Epstein, E. Zak, B. Review of Phosphate Methodologies. *Ann Clin Lab Sci.* **5**, 399–416 (1975).
150. Chifflet, S. & Torriglia, A. A Method for the Determination of inorganic Phosphate in the Presence of Labile Organic Phosphate and High Concentrations of Protein: Application to Lens ATPases. *Anal Biochem* **168**, 1–4 (1988).
151. Nitsche, J. *et al.* Structural basis for activation of plasma-membrane Ca²⁺-ATPase by calmodulin. *Commun. Biol.* **1**, 1–10 (2018).
152. Spadaccini, R., Kaur, H., Becker-Baldus, J. & Glaubitz, C. The effect of drug binding

- on specific sites in transmembrane helices 4 and 6 of the ABC exporter MsbA studied by DNP-enhanced solid-state NMR. *Biochim. Biophys. Acta - Biomembr.* **1860**, 833–840 (2018).
153. Angiulli, G. *et al.* New approach for membrane protein reconstitution into peptidiscs and basis for their adaptability to different proteins. *Elife* **9**, 1–20 (2020).
 154. Chen, J. Molecular mechanism of the Escherichia coli maltose transporter. *Current Opinion in Structural Biology* **23**, 492–498 (2013).
 155. Punjani, A. & Fleet, D. J. 3D variability analysis: Resolving continuous flexibility and discrete heterogeneity from single particle cryo-EM. *J. Struct. Biol.* **213**, 107702 (2021).
 156. Kalienkova, V. *et al.* Stepwise activation mechanism of the scramblase nhtmem16 revealed by cryo- em. *Elife* **8**, 1–27 (2019).
 157. Kontziampasis, D. *et al.* A cryo-EM grid preparation device for time-resolved structural studies. *IUCrJ* **6**, 1024–1031 (2019).
 158. Haertlein, M. *et al.* *Biomolecular Deuteration for Neutron Structural Biology and Dynamics. Methods in Enzymology* **566**, (Elsevier Inc., 2016).
 159. Molodenskiy, D. S., Svergun, D. I. & Mertens, H. D. T. MPBuilder: A PyMOL Plugin for Building and Refinement of Solubilized Membrane Proteins Against Small Angle X-ray Scattering Data. *J. Mol. Biol.* **433**, 166888 (2021).
 160. Bogdanov, M. *et al.* Plasticity of lipid-protein interactions in the function and topogenesis of the membrane protein lactose permease from Escherichia coli. *PNAS* **107**, 15057–15062 (2010).
 161. Levantino, M., Yorke, B. A., Monteiro, D. C. F., Cammarata, M. & Pearson, A. R. Using synchrotrons and XFELs for time-resolved X-ray crystallography and solution scattering experiments on biomolecules. *Current Opinion in Structural Biology* **35**, 41–48 (2015).
 162. Galazzo, L. *et al.* The ABC transporter MsbA adopts the wide inward-open conformation in E. coli cells. *Sci. Adv.* **8**, eabn6845 (2022).
 163. Orelle, C., Dalmás, O., Gros, P., Di Pietro, A. & Jault, J. M. The Conserved Glutamate Residue Adjacent to the Walker-B Motif is the Catalytic Base for ATP Hydrolysis in the ATP-binding Cassette Transporter BmrA. *J. Biol. Chem.* **278**, 47002–47008 (2003).

164. Zaitseva, J., Jenewein, S., Jumpertz, T., Holland, I. B. & Schmitt, L. H662 is the linchpin of ATP hydrolysis in the nucleotide-binding domain of the ABC transporter HlyB. *EMBO J.* **24**, 1901–1910 (2005).
165. Oldham, M. L., Khare, D., Quioco, F. A., Davidson, A. L. & Chen, J. Crystal structure of a catalytic intermediate of the maltose transporter. *Nature* **450**, 515–521 (2007).
166. Moody, J. E., Millen, L. & Binns, D. Cooperative, ATP-dependent association of the nucleotide binding cassettes during the catalytic cycle of ATP-binding cassette transporters. *J. Biol. Chem.* **277**, 21111–21114 (2002).
167. Janas, E. *et al.* The ATP hydrolysis cycle of the nucleotide-binding domain of the mitochondrial ATP-binding cassette transporter Mdl1p. *J. Biol. Chem.* **278**, 26862–26869 (2003).
168. Schultz, K. M., Merten, J. A. & Klug, C. S. Characterization of the E506Q and H537A Dysfunctional Mutants in the E. coli ABC Transporter MsbA. *Biochemistry* **50**, 3599–3608 (2011).
169. Schultz, K. M., Merten, J. A. & Klug, C. S. Effects of the L511P and D512G mutations on the escherichia coli ABC transporter MsbA. *Biochemistry* **50**, 2594–2602 (2011).
170. Lloris-Garcerá, P. *et al.* DirectMX – One-Step Reconstitution of Membrane Proteins From Crude Cell Membranes Into Salipro Nanoparticles. *Front. Bioeng. Biotechnol.* **8**, 1–9 (2020).

5 Safety and Disposal

In this study several hazardous and toxic chemicals were used. They are listed in Table 14.

Table 14: Hazardous and toxic chemicals used in this thesis.

Compound	CAS-No.	GHS hazard	Hazard statements	Precautionary statements
Acetic acid, 96 %	64-19-7	GHS02, GHS05	H226, H314	P280, P305+351+338, P310
Chloramphenicol	56-75-7	GHS06, GHS08	H318, H351, H361	P202, P280, P305+P351+P338, P308+P313
2-Mercapto ethanol	60-24-2	GHS06, GHS09	H302, H411, H315, H335, H311, H319	P280, P312, P302+350, P261, P273, P301+312, P305+351+338
DTT	578517	GHS07	H302, H315, H319, H335	P302+P352, P305+P351+P338
EDTA	60-00-4	GHS07	H319	P305+P351+P338
Ethanol	64-17-5	GHS02	H225	P210
HCl, 36 %	7647-01-0	GHS05, GHS07	H290, H314, H335	P280, P303+P361+P353, P305+P351+P338+P310
Imidazole	288-32-4	GHS05, GHS06, GHS08	H301, H314, H361	P260, P281, P303+P361+P353, P301+P330+P331, P305+P351+P338, P308+P313
Isopropanol	67-63-0	GHS02, GHS07	H225, H319,	P210, P233, P305+P351+P338

			H336	
Kanamycin-sulfate	25-389-04-0	GHS08	H360	P201, P308+P313
KOH	1310-58-3	GHS05, GHS07	H290, H302, H314	P260, P280, P301+P312+P330, P303+P361+P353, P304+P340+P310, P305+P351+P338
Methanol	67-56-1	GHS02, GHS06, GHS08	H225, H301, H311, H331, H370	P210, P280, P302+P352+P312, P304+P340+P312, P370+P378, P403+P235
NaOH	1310-73-2	GHS05	H290, H314	P260, P280, P303+P361+P353, P304+P340+P310, P305+P351+P338
SDS	151-21-3	GHS02, GHS06	H228, H302, H311, H315, H319, H335	P210, P261, P280, P312, P305+P351+P338
Triton X-100	9002-93-1	GHS05, GHS07, GHS09	H302, H318, H411	P270, P273, P280, P305+P351+P338, P310
Chloroform	67-66-3	GHS06, GHS08	H302, H331, H315, H319, H351, H361d, H336,	P201, P273, P301+P312+P330, P302+P352, P304+P340+P311, P308+P313

			H372, H412	
CaCl ₂	10043-52-4	GHS07	H319	P305+P351+P338
Sulfuric acid	7664-93-9	GHS05	H290, H314	P280, P301+P330+P331, P303+P361+P353, P305+P351+P338+P310
di-Ammonium hydrogen citrate	3012-65-5	GHS07	H315, H319	P264, P280, P302+P352, P305+P351+P338, P332+P313, P337+P313
FeCl ₃ ·6H ₂ O	10025-77-1	GHS05, GHS07	H302, H315, H318	P264, P270, P280, P301+P312, P302+P352, P305+P351+P338
ZnSO ₄ ·7H ₂ O	231-793-3	GHS05, GHS07, GHS09	H302, H318, H410	P264, P270, P273, P280, P301+P312, P305+P351+P338
CuSO ₄ ·5H ₂ O	7758-99-8	GHS05, GHS07, GHS09	H302, H318, H410	P264, P270, P273, P280, P301+P312, P305+P351+P338
MnSO ₄ ·4H ₂ O	15244-36-7	GHS08GHS09	H373, H411	P260, P273, P314, P391, P501
CoCl ₂ ·6H ₂ O	7791-13-1	GHS07, GHS08, GHS09	H302, H317, H334, H341, H350i, H360F, H410	P273, P280, P301+P312, P302+P352, P304+P340+P312, P308+P313

Hexane	110-54-3	GHS02, GHS07, GHS08, GHS09	H225, H304, H361f, H373, H315, H336, H411	P210, P240, P273, P301+P310, P331, P302+P352, P403+P235
Gentamicin	1405-41-0	GHS08	H17, H334	P261, P280, P342+P311
Butylated hydroxytoluene	128-37-0	GHS09	H410	P273, P391, P501
Acetone	67-64-1	GHS02, GHS07	H225, H302, H319, H336, H373	P210, P235, P260, P305+P351+P338
Ammonia solution	1336-21-6	GHS05 GHS06 GHS07 GHS09	H302, H314, H335, H410	P261, P271, P273, P280, P303+P361+P353, P305+P351+P338
H ₂ O ₂	7722-84-1	GHS03 GHS05 GHS07	H271, H302, H314, H332, H335, H412	P280, P305+P351+P338, P310

5.1 GHS hazards statements

H225	Highly flammable liquid and vapor
H226	Flammable liquid and vapor
H228	Flammable solid
H272	May intensify fire; oxidizer
H290	May be corrosive to metals

H301	Toxic if swallowed
H302	Harmful if swallowed
H303	May be harmful if swallowed
H311	Toxic in contact with skin
H312	Harmful in contact with skin
H313	May be harmful in contact with skin
H314	Causes severe skin burns and eye damage
H315	Causes skin irritation
H316	Causes mild skin irritation
H317	May cause an allergic skin reaction
H318	Causes serious eye damage
H319	Causes serious eye irritation
H330	Fatal if inhaled
H331	Toxic if inhaled
H332	Harmful if inhaled
H333	May be harmful if inhaled
H334	May cause allergy or asthma symptoms or breathing difficulties if inhaled
H335	May cause respiratory irritation
H336	May cause drowsiness or dizziness
H340	May cause genetic defects
H341	Suspected of causing genetic defects
H350	May cause cancer
H350i	May cause cancer by inhalation
H360	May damage fertility or the unborn child
H360D	May damage the unborn child
H360F	May damage fertility
H360Fd	May damage fertility. Suspected of damaging the unborn child
H360FD	May damage fertility. May damage the unborn child
H361	Suspected of damaging fertility or the unborn child
H361d	Suspected of damaging the unborn child.
H361f	Suspected of damaging fertility

H370	Cause damage to organs
H372	Causes damage to organs through prolonged or repeated exposure
H373	May cause damage to organs through prolonged or repeated exposure.
H400	Very toxic to aquatic life with long-lasting effects
H410	Very toxic to aquatic life with long lasting effects
H411	Toxic to aquatic life with long lasting effects
H412	Harmful to aquatic life with long lasting effects.
EUH032	Contact with acids liberates very toxic gas
EUH066	Repeated exposure may cause skin dryness or cracking

5.2 GHS precautional statements

P101	If medical advice is needed, have product container or label at hand
P201	Obtain special instructions before use
P210	Keep away from heat/sparks/open flames/hot surfaces – No smoking
P233	Keep container tightly closed
P260	Do not breathe dust/fume/gas/mist/vapours/spray
P261	Avoid breathing dust/fume/gas/mist/vapours/spray
P264	Wash thoroughly after handling
P270	Do not eat, drink or smoke when using this product
P273	Avoid release to the environment
P281	Use personal protective equipment as required
P280	Wear protective gloves/protective clothing/eye protection/face protection
P284	Wear respiratory protection
P309	IF exposed or you feel unwell
P310	Immediately call a POISON CENTER or doctor/physician
P311	Call a POISON CENTER or doctor/physician
P312	Call a POISON CENTER or doctor/physician if you feel unwell
P321	Specific treatment (see respective MSDS)
P330	Rinse mouth
P362	Take off contaminated clothing and wash before reuse

P391	Collect spillage
P405	Store locked up
P501	Dispose of contents/container in accordance with local/regional/national/ international regulations
P301+P310	IF SWALLOWED: Immediately call a POISON CENTER or doctor/physician
P301+P312	IF SWALLOWED: Call a POISON CENTER or doctor/physician if you feel unwell
P301+P330+P331	IF SWALLOWED: Rinse mouth. Do NOT induce vomiting
P302+P352	IF ON SKIN: Wash with soap and water
P303+P361+P353	IF ON SKIN (or hair): Remove/Take off immediately all contaminated clothing. Rinse skin with water/shower
P304+P341	IF INHALED: If breathing is difficult, remove victim to fresh air and keep at rest in a position comfortable for breathing
P305+P351+P338	IF IN EYES: Rinse cautiously with water for several minutes. Remove contact lenses if present and easy to do - continue rinsing
P308+P313	IF exposed or concerned: Get medical advice/attention
P309+P311	IF exposed or you feel unwell: Call a POISON CENTER or doctor/physician
P332+P313	If skin irritation occurs: Get medical advice/attention
P333+P313	If skin irritation or rash occurs: Get medical advice/attention
P337+P313	If eye irritation persists: Get medical advice/attention
P342+P311	Call a POISON CENTER or doctor/physician
P370+P378	In case of fire: Use for extinction: Alcohol resistant foam
P370+P378	In case of fire: Use for extinction: Fire-extinguishing powder
P370+P378	In case of fire: Use for extinction: Carbon dioxide
P403+P233	Store in a well-ventilated place. Keep container tightly closed
P403+P235	Store in a well-ventilated place. Keep cool

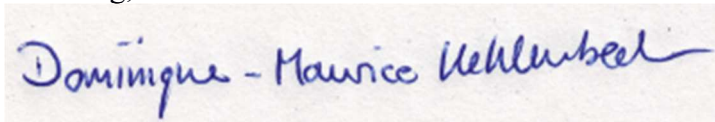
5.3 Disposal

All chemicals used during the experiments were handled and disposed according to their GHS safety and precautionary statements. Solvents and contaminated waste were stored in the indicated boxes and disposed according to the safety instructions. Genetically modified organisms and related waste were autoclaved according to the “Gentechnikgesetz” before disposal for 20 min at 121°C and 5 bar.

6 Eidesstattliche Versicherung

Hiermit versichere ich an Eides statt, die vorliegende Dissertation selbst verfasst und keine anderen als die angegebenen Hilfsmittel benutzt zu haben. Die eingereichte schriftliche Fassung entspricht der auf dem elektronischen Speichermedium. Ich versichere, dass die Dissertation nicht in einem früheren Promotionsverfahren eingereicht wurde.

Hamburg, den 11.01.2023



Dominique - Maurice Kehlus